Electron-volt neutron spectroscopy: beyond fundamental systems

Carla Andreani, Maciej Krzystyniak, Giovanni Romanelli, Roberto Senesi and Felix Fernandez-Alonso

Published version information

Citation: C Andreani et al. "Electron-volt neutron spectroscopy: beyond fundamental systems." Advances in Physics, vol. 66, no. 1 (2017): 1-73.

doi: 10.1080/00018732.2017.1317963

This is an Accepted Manuscript of an article published by Taylor & Francis in Advances in Physics on 28/04/2017, available online: http://dx.doi.org/10.1080/00018732.2017.1317963

To appear in *Advances in Physics*
Vol. 00, No. 00, Month 20XX, 1–84

REVIEW ARTICLE

Electron-volt neutron spectroscopy: beyond fundamental systems

Carla Andreani,[a,b] Maciej Krzystyniak,[c,d] Giovanni Romanelli,[c] Roberto Senesi,[a,b] and Felix Fernandez-Alonso[c,e*]

[a] *Università degli Studi di Roma 'Tor Vergata,' NAST Centre and Dipartimento di Fisica, Via della Ricerca Scientifica 1, 00133, Roma, Italy;* [b] *Consiglio Nazionale delle Ricerche, CNR-IPCF, Sezione di Messina, Italy;* [c] *ISIS Facility, Rutherford Appleton Laboratory, Chilton, Didcot, Oxfordshire OX11 0QX, United Kingdom;* [d] *School of Science and Technology, Nottingham Trent University, Clifton Campus, Nottingham NG11 8NS, United Kingdom;* [e] *Department of Physics and Astronomy, University College London, Gower Street, London WC1E 6BT, United Kingdom.*

(*last revised 31 March 2017*)

This work provides an up-to-date account of the use of electron-volt neutron spectroscopy in materials research. This is a growing area of neutron science, capitalising upon the unique insights provided by epithermal neutrons on the behaviour and properties of an increasing number of complex materials. As such, the present work builds upon the aims and scope of a previous contribution to this journal back in 2005, whose primary focus was on a detailed description of the theoretical foundations of the technique and their application to fundamental systems [see *Advances in Physics* **54** 377 (2005)]. A lot has happened since then, and this review intends to capture such progress in the field. With both expert and novice in mind, we start by presenting the general principles underpinning the technique and discuss recent conceptual and methodological developments. We emphasize the increasing use of the technique as a non-invasive spectroscopic probe with intrinsic mass selectivity, as well as the concurrent use of neutron diffraction and first-principles computational materials modelling to guide and interpret experiments. To illustrate the state-of-the-art, we discuss in detail a number of recent exemplars, chosen to highlight the use of electron-volt neutron spectroscopy across physics, chemistry, biology, and materials science. These include: hydrides and proton conductors for energy applications; protons, deuterons, and oxygen atoms in bulk water; aqueous protons confined in nanoporous silicas, carbon nanotubes, and graphene-related materials; hydrated water in proteins and DNA; and the uptake of molecular hydrogen by soft nanostructured media, promising materials for energy-storage applications. For the primary benefit of the novice, this last case study is presented in a pedagogical and question-driven fashion, in the hope that it will stimulate further work into uncharted territory by newcomers to the field. All along, we emphasize the increasing (and much-needed) synergy between experiments using electron-volt neutrons and contemporary condensed-matter theory and materials modelling to compute and ultimately understand neutron-scattering observables, as well as their relation to materials properties not amenable to scrutiny using other experimental probes.

PACS: 61.05.F-; 63.20.dk; 81.05.-t; 81.07.-b; 87.15.-v; 88.30.-k

Keywords: electron-volt neutron spectroscopy; deep-inelastic neutron scattering; neutron Compton scattering; mass-selective neutron spectroscopy; nuclear momentum distribution; nuclear quantum effects; neutron diffraction; proton conductors; water and aqueous media; hydrogen storage.

*Corresponding author. Email: felix.fernandez-alonso@stfc.ac.uk

Contents

1. Setting the scene

The use of electron-Volt (eV) neutrons to study condensed matter systems was reviewed about a decade ago with an emphasis on a detailed description of the underlying theoretical formalism and the study of the fundamental properties of bulk systems such as helium (He), molecular hydrogen (H_2), and their isotopic counterparts [1]. A lot has happened since then, and the present work intends to capture such progress in the field both in terms of technical as well as conceptual and scientific developments. The primary driver behind these efforts has been the increasing need to understand and subsequently exploit the properties of new and increasingly complex functional materials, an intrinsically interdisciplinary effort across physics, chemistry, biology, materials science, and engineering.

Neutron scattering using thermal and cold neutrons is a well-established non-invasive technique, extensively used to provide direct and unique information on the physical and chemical properties of materials at the atomic level [2, 3]. Current efforts at a global level to investigate materials for energy applications constitute a good case in point, given the pressing need to find clean and sustainable alternatives to the environmentally unfriendly combustion of fossil fuels. In this case, neutrons are exceptionally well suited to study *in situ* or under *operando* conditions how the transport and binding of energy- and charge-carrying atoms and molecules are related to structure and transport properties, including a detailed understanding of the micro and mesostructure of porous sorbents and adsorbents as well as the underlying mechanism of molecular and macromolecular uptake. In particular, the development of new technologies for energy and sustainable applications often requires a sound understanding of the behaviour of light atomic and molecular species such as H^+, Li^+, H_2, or hydrocarbons like methane, all of which are particularly well suited to investigation using neutron-scattering techniques. As a consequence of the above, neutron-based analysis is nowadays routinely carried out in the characterisation of hydrogen-storage, fuel-cell, catalytic, and battery materials. Similar

research into solar-cell, nuclear remediation, and carbon-dioxide capture/storage materials rely on other unique aspects of neutron scattering and, again, serve to illustrate how its use to probe structural and dynamical properties can provide much-needed insights into material stability or the uptake, binding, or mobility of key atomic, molecular, and supramolecular species of technological interest.

There are two types of neutron-scattering processes which can be used to investigate the properties of materials, namely, coherent and incoherent scattering. Coherent scattering enables the use of the neutron in much the same way as X-ray crystallography is used to determine atomic and molecular structure. In addition, neutrons can probe *collective* excitations in condensed matter (*e.g.,* phonons) via the use of Inelastic Neutron Scattering (INS) techniques. Incoherent scattering is of particular relevance to the study of hydrogen-containing systems due to the very large incoherent scattering cross section of the ^{1}H nucleus. Furthermore, incoherent INS can be used to study both the stochastic (diffusion) and vibrational dynamics of atoms in condensed matter. For example, diffusive motions (translational and rotational) in liquid water correspond to energy transfers below 1 meV, the so-called QuasiElastic Neutron Scattering (QENS) regime, whereas well-defined inter and intramolecular vibrational modes require energy transfers up to 400-500 meV, well within the reach of INS. Operationally speaking, vibrational motions in condensed matter are bounded by the fundamental energy of vibration of the H_2 molecule at *ca.* 500 meV. Beyond this energy transfer, the neutron-scattering response contains the cumulative contribution from overtones and combination bands associated with lower-lying fundamental transitions and, at sufficiently high incident energies (typically a few eV), all scattering can be ascribed to the dynamics associated with individual nuclei. This peculiar situation corresponds to the so-called *Neutron Compton Scattering* or NCS regime, and constitutes the focus of this review.

Relative to the widespread use of thermal and cold neutrons, the NCS regime has not been fully exploited for a number of reasons. On the technical front, it has required the development and subsequent deployment of pulsed spallation neutron sources based on accelerator technology during the last quarter of the past century, followed by significant and crucial advances in the requisite instrumentation. These technical achievements have opened up a new area for neutron science and condensed matter research, as exemplified by over thirty years of successful and uninterrupted operation of the ISIS Facility, Rutherford Appleton Laboratory, United Kingdom [4]. Accelerator-driven sources can deliver temporally tight neutron pulses that guarantee an outstanding spectral resolution over a wide dynamic range [5]. This condition requires keeping moderator sizes deliberately small, resulting in a significant fraction of undermoderated neutrons, and a so-called epithermal-neutron spectrum which is distinctly different from the celebrated Maxwell-Boltzmann distribution for energies above 100 meV. In this regime, the neutron flux per unit energy follows a characteristic '$1/E$-law' and the integrated epithermal flux becomes orders of magnitude higher than what is found in existing research reactors.

The above developments have paved the way for neutron-scattering experiments using epithermal neutrons of up to hundreds of eV using *Deep Inelastic Neutron Scattering* (DINS). We note that either DINS or NCS are both used in the literature to describe the same technique. For the sake of clarity, this review will hereafter use the former acronym exclusively. DINS was originally proposed to extract the *Nuclear Momentum Distribution* (NMD) and associated *mean kinetic energy* $\langle E_K \rangle$ in superfluid ^{4}He [6] and, more generally, to access the short-time single-particle dynamics in condensed-matter media [7, 8]. Since the mid 1980s, experimental methodologies and associated infrastructure for epithermal neutron scattering have been extensively developed and exploited at the ISIS Facility [1, 9]. DINS studies at ISIS started on the eVS spectrometer [10], a pioneering

instrument that has been superseded by VESUVIO in the past decade [11–32]. These early years saw the first DINS studies using energy transfers in excess of 1 eV and momentum transfers in excess of 20 Å^{-1}. The uniqueness of this scattering regime in terms of the physical observables amenable to investigation is covered in Section 2 of this work, and includes direct access to the quantum character of atomic motions in a mass-resolved manner, a feature which distinguishes DINS from other neutron techniques at lower energies. To illustrate these, we describe in some detail the application of DINS to light hydrides and proton conductors, as well as how state-of-the-art computational materials modelling has been used to guide and interpret DINS experiments. Section 2.3 describes in detail parallel developments of novel concepts and devices using epithermal neutrons for specific applications, and the recent implementation of *MAss-selective Neutron SpEctroscopy* (MANSE). MANSE constitutes a natural extension of DINS, placing increasing emphasis on the direct analysis of raw experimental data to gain simultaneous insights into the behaviour of several atomic species. As such, it has been a primary driver to extend the realm of applicability of the technique to complex materials. In some cases, we note that these new techniques and associated instrumentation have transcended their exclusive use for DINS. These include non-invasive and non-destructive investigations of archeological artefacts and cultural heritage [33], or the irradiation of electronic devices [34], to name a few. For a recent appraisal of these instrumentation developments and future perspectives, the reader may also consult Ref. [35] and references therein.

Section 3 shifts the focus of this work to the presentation of specific systems. With both the expert and the novice in mind, we build upon the examples given in previous sections and choose to restrict our presentation to a limited set of physical systems, in order to walk the reader through the application of DINS in specific situations. Our primary intent is to illustrate the *why*, the *what*, and the *how* underpinning the use of DINS in the study of functional materials, as opposed to providing a long (and rapidly growing) list of systems that have or could be tackled in the foreseeable future. To this end, Section 3.1 is devoted to water and aqueous media, an intense area of DINS research over the past decade or so. This presentation includes both bulk and nanostructured media. In the former case, DINS unequivocally shows that *Nuclear Quantum Effects* (NQEs) are responsible for the destructuring of the bulk liquid, *i.e.*, these NQEs are roughly equivalent to a 50 K temperature rise in models that treat nuclear motions in a classical fashion; similarly, quantum contributions to the excess chemical potential amount to roughly 10% of the total [36]. This discussion is complemented by a consideration of bulk water around the triple point and in the supercritical state, the latter case being a situation of certain technological relevance. In the case of melting, the emergence of competing quantum effects is presented in detail, as it represents a timely example of the combined use of DINS experiments and the most sophisticated approaches to computational materials modelling available at present. The last two parts in Section 3.1 describe the behaviour of water under nanoscale confinement and in biological systems, and serve to illustrate a recent change in direction in terms of the use of DINS to explore increasingly more complex media. The case study in Section 3.2 deals with the interaction of H_2 with nanoporous media. The pedagogical and question-driven style that we have adopted to present this case is meant to address the needs of a growing body of potential practitioners who are yet not familiar with the technique. The technological driver underpinning this case study is inextricably linked to the use of H_2 as a fuel store and energy vector, a goal that has stimulated a large and growing body of research over the past few decades aimed at finding economically viable ways of storing this molecule in sufficient quantities to replace greenhouse-gas-producing fossil fuels [37]. To date, however, no single material has been found to meet the stringent requirements for

practical applications, as identified by government agencies such as the US Department of Energy or the automotive industry [38]. The central role played by H_2 is not restricted to its storage via physical or chemical routes. Other situations of practical interest where H_2 is a key player include its generation in photocatalytic water-splitting reactions [39], as well as its widespread use in a wide range of industrial chemical processes [40]. On the experimental front, the study of H_2 is not a trivial task given the absence of dipole-allowed optical transitions in the ground state and the need of photon sources in the UV and VUV to access electronic excitations [41, 42]. In the above context, we illustrate how DINS has been used with success in the study of H_2 uptake by carbon-based intercalation compounds. These studies have shown how the technique can lead to fresh insights into the nature of the geometry and motions of the H_2 adsorbate in these technologically relevant materials.

In closing this preamble, we note that an increasing number of research with epithermal neutrons has and continues to provide a direct and unique link to state-of-the-art methodological developments aimed at an accurate theoretical description of NQEs in condensed matter [43–47]. This demonstrated synergy between state-of-the-art experiments and theory constitutes at present a strong driving force for the field and we believe that it will continue to be case in the years to come. Also, it provides a much-needed starting point to understand neutron observables in complex materials, particularly those aimed at addressing current and foreseeable societal challenges requiring a sound understanding of materials properties, as well as how these ultimately relate to function and performance.

2. Theory and practice

2.1. *Conceptual and theoretical preliminaries*

At energies well above typical excitation energies in a condensed matter system, the double differential neutron-scattering cross section for a single atomic species using unpolarized neutrons is related to the dynamic structure factor $S(\vec{\mathbf{Q}},\omega)$ via [2, 48, 49]

$$\frac{d^2\sigma(E_0,E_1,\phi)}{d\Omega dE_1} = \hbar^{-1}\sqrt{\frac{E_1}{E_0}}\frac{\sigma}{4\pi}S(\vec{\mathbf{Q}},\omega) \tag{1}$$

where E_1 and E_0 are the energies of the scattered and incident neutrons, respectively, $\hbar\vec{\mathbf{Q}}$ and $\hbar\omega$ are the momentum and energy transfers, ϕ is the scattering angle, and σ the total scattering cross section

$$\sigma = 4\pi\left[|b|^2 + (|b^2| - |b|^2)\right] = 4\pi|b^2| \tag{2}$$

where b is the neutron-scattering length for the target nuclide (H, D, ^{7}Li, etc). In line with our remarks when describing neutron-scattering processes earlier in the introduction, the identity in the middle of Eq. (2) has been written such that the first term represents the familiar 'coherent' contribution proportional to $|b|^2$ and a second 'incoherent' contribution arises from the nuclear-spin dependence of the neutron-scattering length for a particular nuclide [2]. It is important to note that Eq. (1) relates to the scattering of neutrons by a given nucleus and, therefore, does not contain magnetic contributions to

the scattering cross section, phenomena which are described in depth in Ref. [3] and will not be described any further in this work. With these considerations in mind, $S(\vec{\mathbf{Q}},\omega)$ can be expressed in terms of the two-particle correlation function $Y_{jj'}(\vec{\mathbf{Q}},t)$ [1, 49]:

$$S(\vec{\mathbf{Q}},\omega) = \frac{1}{2\pi N}\int_{-\infty}^{\infty} \exp(i\omega t) \sum_{jj'} Y_{jj'}(\vec{\mathbf{Q}},t)\, dt \tag{3}$$

where N is the number of particles in the target system. The correlation function $Y_{jj'}(\vec{\mathbf{Q}},t)$ is given by the following ensemble average

$$Y_{jj'}(\vec{\mathbf{Q}},t) = \left\langle \exp[-i\vec{\mathbf{Q}}\cdot\widehat{\mathbf{r}}_j]\exp[i\vec{\mathbf{Q}}\cdot\widehat{\mathbf{r}}_{j'}(t)]\right\rangle \tag{4}$$

In this expression, $\widehat{\mathbf{r}}_j(t)$ is the Heisenberg operator for the position of particle j at time t, and $\widehat{\mathbf{r}}_j = \widehat{\mathbf{r}}_j(0)$. The operator $\exp[-i\vec{\mathbf{Q}}\cdot\widehat{\mathbf{r}}_j]$ couples the plane wave of the neutron with the position of the nucleus in the target system.

2.1.1. The impulse approximation and the neutron Compton profile

As the name implies, DINS refers to a neutron-scattering regime in which the incident neutron energy is well above the binding energies of the scattering atoms. This condition amounts to considering large $\hbar\vec{\mathbf{Q}}$ and $\hbar\omega$ relative to other momentum and energy scales in the system under investigation. In this case, the neutron-scattering process is adequately described within the framework of the impulse approximation (IA), which becomes exact in the limit of infinite momentum transfer [9, 50, 51]. In this case, the distribution of scattered neutrons can be calculated by recourse to classical kinematics [1, 9, 52]. In the IA regime, the inelastic neutron-scattering cross section is related in a simple way to the NMD. Below, we outline the physical conditions under which the IA regime is attained.

In the approximation of negligible external forces acting on the compound neutron-nucleus system, the use of momentum and energy conservation laws provides a direct relationship between $\hbar\vec{\mathbf{Q}}$ and $\hbar\omega$ of the form:

$$\hbar\omega = \frac{(\vec{\mathbf{p_n}} - \vec{\mathbf{p_n}}')^2}{2M} + \frac{(\vec{\mathbf{p_n}} - \vec{\mathbf{p_n}}')\cdot\vec{\mathbf{p}}}{M} = \frac{\hbar^2 Q^2}{2M} + \frac{\vec{\mathbf{Q}}\cdot\vec{\mathbf{p}}}{M} \tag{5}$$

where $\hbar\vec{\mathbf{Q}} = \vec{\mathbf{p_n}} - \vec{\mathbf{p_n}}'$ with $\vec{\mathbf{p_n}}$ and $\vec{\mathbf{p_n}}'$ are the momenta of the incident and scattered neutron, respectively. M and $\vec{\mathbf{p}}$ are the mass and the momentum of the struck particle before the collision. These kinematic variables are shown pictorially in Fig. 1. The scattering of neutrons by a given atom is used to determine its momentum distribution. Unlike a classical particle, the *Heisenberg Uncertainty Principle* links the momentum and position of the atom which, in turn, is dictated by the underlying potential-energy landscape or confining potential. Much of the discussion that will follow about DINS boils down to finding ways of relating the measured momentum distribution to the other two quantities.

At the high Q values accessible in DINS experiments, the scattering is entirely incoherent, that is, it originates from the interaction of the neutron with individual nuclei. Thus, DINS provides a direct probe of the distribution of atomic momenta in the target

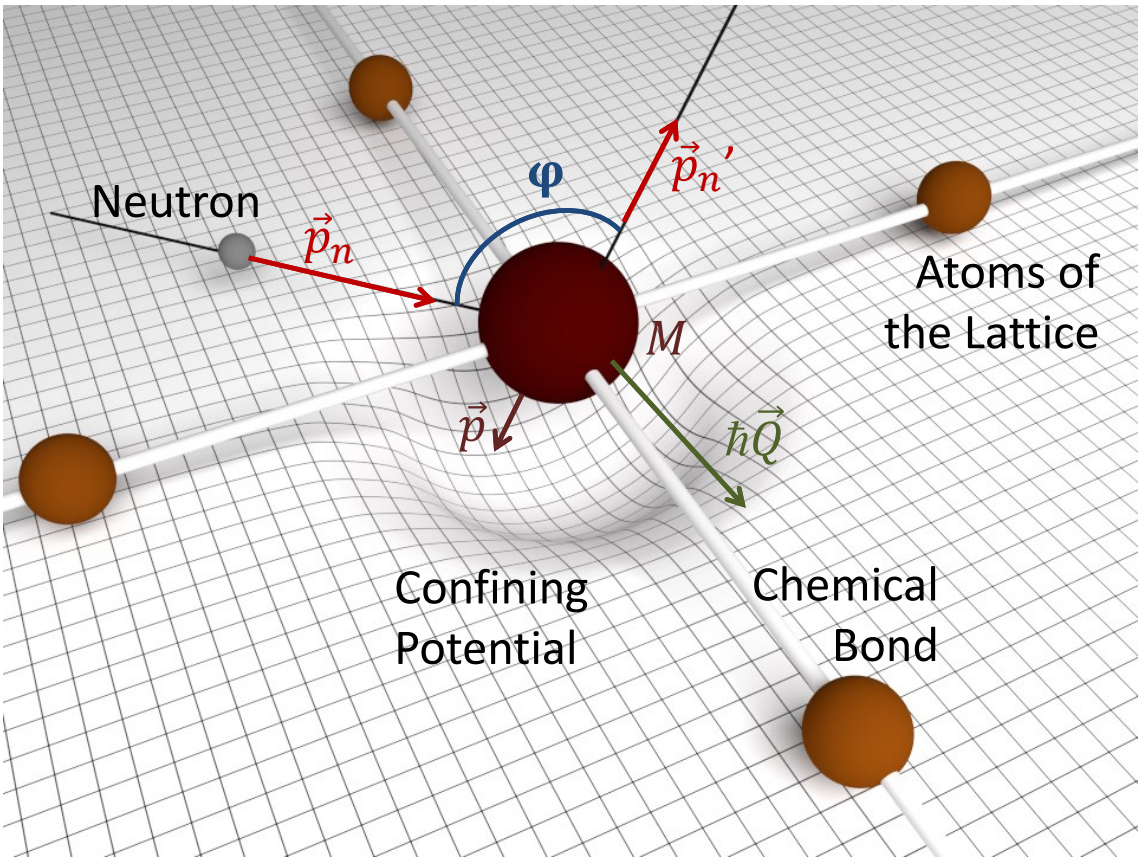

Figure 1. Kinematic variables used in the main text to describe the scattering of eV neutrons in a condensed-matter system. For illustrative purposes, the curved grid represents the confining potential around a given atom in a lattice.

system, *i.e.*, the energy distribution of the scattered neutron is directly related to the distribution of particle momenta projected onto the scattering vector $\vec{\mathbf{Q}}$. The formalism required to extract momentum distributions from experimental data is given in the next section.

For sufficiently small t, $\widehat{\mathbf{r}}_j(t)$ can be replaced by

$$\widehat{\mathbf{r}}_j(t) \simeq \widehat{\mathbf{r}}_j + \frac{t}{M_j}\widehat{\mathbf{p}}_j \tag{6}$$

where $\widehat{\mathbf{p}}_j$ is the momentum operator (vector) of particle j of mass M_j. Physically, this approximation implies that the particle travels freely over short enough times and, therefore, its interaction with other particles can be neglected over this brief time interval. The next step is to use the approximation introduced in Eq. (6) in Eq. (4) using standard commutation relations between momentum and position, to derive a working expression in the limit of high Q [1], where the exponential terms containing position operators of different nuclei in the above correlation function will oscillate rapidly from atom to atom and cancel out on average. The correlations between the positions of different nuclei will then be absent and the incoherent approximation holds such that only $j = j'$ terms associated with the properties of the same particle will be retained. One then obtains:

$$Y_{jj}(\vec{\mathbf{Q}},t) = \exp\left[\frac{i\hbar\, t\, Q^2}{2M_j}\right]\left\langle \exp\left[\frac{i\, t}{M_j}\vec{\mathbf{Q}}\cdot\widehat{\mathbf{p}}_j\right]\right\rangle \tag{7}$$

The IA approximation to the incoherent ($j = j'$) dynamic structure factor for an isotropic system is obtained by using Eq. (7) in Eq. (3)

$$S_{IA}(\vec{\mathbf{Q}},\omega) = \frac{1}{2\pi\, N}\sum_j \int_{-\infty}^{\infty} \exp\left[-i\omega t + \frac{i\hbar\, t\, Q^2}{2M_j}\right]\left\langle \exp\left[\frac{i\, t}{M_j}\vec{\mathbf{Q}}\cdot\widehat{\mathbf{p}}_j\right]\right\rangle dt \tag{8}$$

where S_{IA} denotes the dynamic structure factor under the IA. Performing the integration over t gives [1]:

$$S_{IA}(\vec{\mathbf{Q}},\omega) = \hbar \int n(\vec{\mathbf{p}})\; \delta\left[\hbar\omega - \hbar\omega_r - \frac{\vec{\mathbf{p}}\cdot\hbar\vec{\mathbf{Q}}}{M}\right] d\vec{\mathbf{p}} \tag{9}$$

The physical meaning of this equation is that scattering occurs between the neutron and a single particle, with conservation of kinetic energy and momentum given by Eq. (5). The quantity $\hbar\omega_r = \frac{\hbar^2 Q^2}{2M}$ is known as the *recoil energy*, *i.e.*, the energy that a stationary particle would have gained from a collision with a neutron owing to momentum and energy conservation. This condition corresponds to the center of the observed recoil peak at a given Q being associated with a recoiling particle of mass M. This recoil peak defines a parabolic trajectory in $(\vec{\mathbf{Q}},\omega)$ space. The NMD of the particle broadens this line by a similar mechanism as the Doppler broadening of spectral lines by atomic motions. Since the position in $(\vec{\mathbf{Q}},\omega)$ space depends on M, particles of different mass can be (at least in principle) distinguished in the observed spectrum. These features are illustrated in Fig. 2 for a series of different atomic masses. Given the quadratic dependence of recoil energy on momentum transfer, mass separation increases rapidly with Q. In the specific example given in this figure, Qs above 100 Å^{-1} are sufficient to resolve the DINS response of the heavier nuclides.

It is important to stress that although we are dealing with a single-particle scattering response, the NMD of a given atom is ultimately sensitive to the many-body nature of all surrounding atoms and their interactions. Thus, these seemingly simple '*billiard − ball*' experiments are of direct relevance to the description of the condensed-matter system as a whole. If we consider a single atom at rest, then the scattering will be represented by a Dirac delta-function of the form $\delta(\hbar\omega_r - \frac{\hbar^2 Q^2}{2M})$, *i.e.,* a peak in the dynamic structure factor at the recoil energy $\hbar\omega_r$. Not all the target atoms will be at rest, and a probability distribution function of particle momenta will weigh the peak of $S(\vec{\mathbf{Q}},\omega)$ to account for the details of this underlying distribution. The determination of the extent and the nature of this *spread* constitutes the primary objective of DINS measurements, as explored in more depth in Section 2.3.

Within the IA limit, the two dynamical variables, Q and ω, are coupled through the definition of the so-called West-scaling variable y [52]:

$$y = \vec{\mathbf{p}}\cdot\hbar\hat{\mathbf{Q}} = \frac{M}{\hbar^2 Q}\left(\hbar\omega - \hbar\omega_r\right) \tag{10}$$

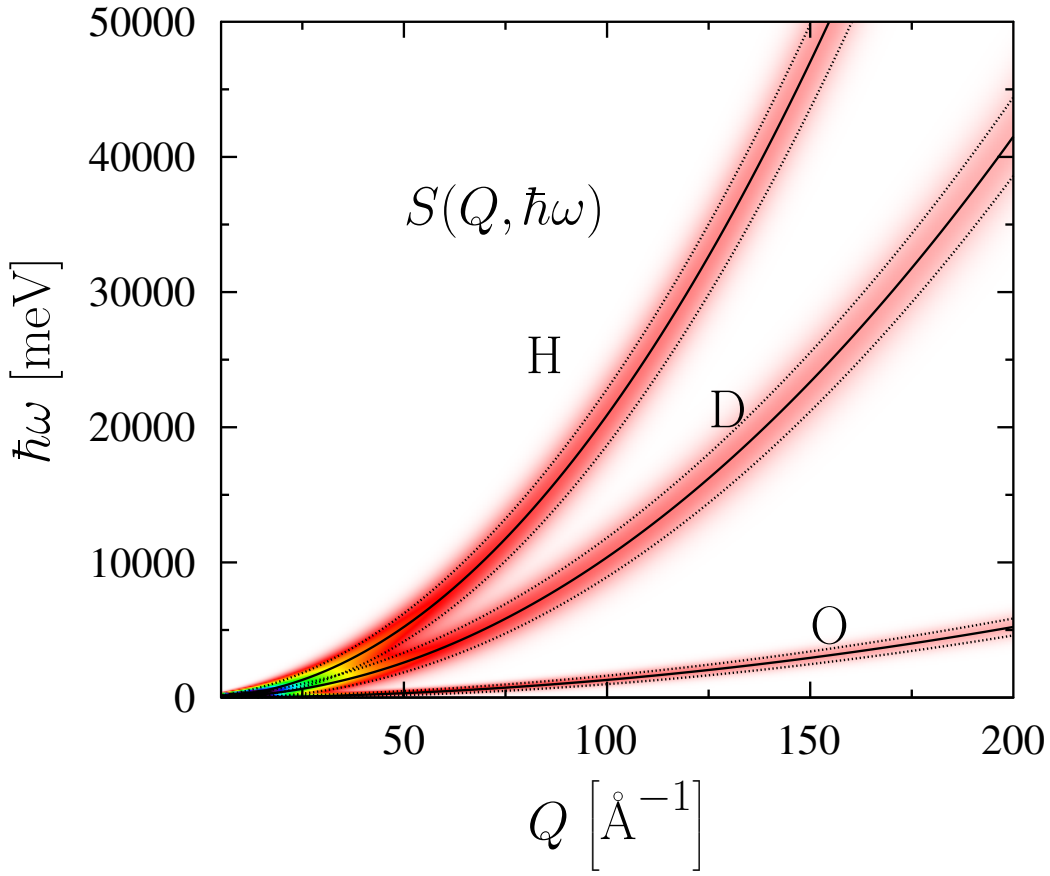

Figure 2. Atomic recoil trajectories as a function of momentum and energy transfer (abscissa and ordinate, respectively). The black solid lines denote parabolic recoil lines for several atomic species given by $\hbar\omega = \hbar^2Q^2/2M$. The dashed lines represent the curves $\hbar\omega = \hbar^2Q^2/2M \pm \hbar^2\sigma Q/M$ where σ is 5, 7 and 12 Å^{-1} for H, D, and O respectively. These dashed lines and the colour shading underneath are used to depict the width and associated extent of the scattering response around the atomic recoil lines. These broadenings are directly related to the overall width of the underlying NMDs, as described in the main text.

where y is the momentum $\vec{\mathbf{p}}$ of the nucleus in the initial state projected onto the scattering vector $\hbar\vec{\mathbf{Q}}$, and $\hat{\mathbf{Q}}$ is a unit vector in the direction of the momentum transfer. We note that it is common practice in the literature to use the same units of Å^{-1} for y and p. The double differential neutron-scattering cross section [Eq. (1)] and the scattering function [Eq. (9)] can then be rewritten, respectively, in the form:

$$\frac{d^2\sigma(E_0,E_1,\phi)}{d\Omega dE_1} = b^2\sqrt{\frac{E_1}{E_0}}\frac{M}{\hbar Q}J(y,\hat{\mathbf{Q}}) \tag{11}$$

and

$$S_{IA}(\vec{\mathbf{Q}},\omega) = \frac{M}{\hbar Q}J(y,\hat{\mathbf{Q}}) \tag{12}$$

The function $J(y, \hat{\mathbf{Q}})$ is known as the *Neutron Compton Profile* (NCP):

$$J(y, \hat{\mathbf{Q}}) = \hbar \int n(\vec{\mathbf{p}})\ \delta(\hbar y - \vec{\mathbf{p}}\cdot\hat{\mathbf{Q}})\ d\vec{\mathbf{p}} \tag{13}$$

a quantity that no longer depends on the magnitude of $\vec{\mathbf{Q}}$. In physical terms, $J(y, \hat{\mathbf{Q}})dy$ corresponds to the probability for an atom to have a momentum of magnitude between $\hbar y$ and $\hbar(y + dy)$ along $\hat{\mathbf{Q}}$. The NCP constitutes the primary observable in a DINS experiment.

To illustrate the physical meaning of the NCP, we can consider some special cases. In an isotropic system (*i.e.*, a liquid or a powder specimen), the direction of $\hat{\mathbf{Q}}$ is immaterial and Eq. (13) yields:

$$J(y) = 2\pi\hbar \int_{|\hbar y|}^{\infty} p\ n(p)\ dp \tag{14}$$

and from Eq. (14) we also have

$$n(p) = -\frac{1}{2\pi\hbar^3 y}\frac{d}{dy}J(y)\ |_{\hbar y = p} \tag{15}$$

The single-particle mean kinetic energy, $\langle E_K \rangle$, can be defined as the second moment of $J(y)$:

$$\langle E_K \rangle = \frac{3\hbar^2}{2M}\int_{-\infty}^{\infty} y^2 J(y) dy = \frac{3\hbar^2}{2M}\,\sigma^2 \tag{16}$$

where σ is the standard deviation of the NCP. The temperature dependence of $\langle E_K \rangle$ can also be estimated from a model of the underlying motions, as shown explicitly in Sections 2.2.2 and 2.2.3

Bearing in mind that DINS experiments are typically performed as one *approaches asymptotically* the IA, one can determine when this approximation is valid and what the corrections might be. The deviations from the IA which occur at finite Q are generally referred to as *Final State Effects* (FSEs), although it should be noted that the IA makes assumptions about the way in which the initial state is treated as well [53]. A detailed description and treatment of FSEs is given in Ref. [1], including the description of alternative methodologies to include them in a quantitative fashion. For the purposes of this work, our discussion below illustrates what the overall effects are in the experimental data, and refer the reader to the aforementioned review and references therein for further details.

Mathematically, one convenient way of capturing FSEs is by making the NCP an explicit function of Q. In this situation, $J(y, \hat{\mathbf{Q}})$ needs to be formally replaced by $J(y, \vec{\mathbf{Q}})$. Equation (12) then needs to be rewritten as:

$$J(y, \vec{\mathbf{Q}}) = \frac{\hbar Q}{M} S(\vec{\mathbf{Q}}, \omega) \tag{17}$$

Physically, any FSE correction at finite Q arises from the effects of the forces on the particle producing displacements from straight-line trajectories on a timescale τ. The latter is a characteristic time τ associated with the scattering process, *i.e.*, it is essentially the decay time of the correlation function $Y_{jj}(\vec{\mathbf{Q}},t)$ which at high Q becomes $\tau = \frac{M}{Q\Delta p}$, Δp being the width of the momentum distribution of the particle. Representing the effect of these deviations on $J(y,\vec{\mathbf{Q}})$ as a series in powers of $1/Q$, one finds for the isotropic case [54]:

$$J(y,Q) = J(y) - \frac{A_3}{Q}\frac{d^3}{dy^3}J(y) + \frac{A_4}{Q^2}\frac{d^4}{dy^4}J(y) + ... \tag{18}$$

where it can be shown that A_3 and A_4 are related to the inter-particle potential V schematically shown in Fig. 1 via

$$A_3 = \frac{M}{36\hbar^2}\left\langle \nabla^2 V \right\rangle; \quad A_4 = \frac{M^2}{72\hbar^4}\left\langle \left(\vec{\nabla}V\right)^2 \right\rangle \tag{19}$$

where $\langle ... \rangle$ stands for a quantum-statistical average. The extension to the case of anisotropic momentum distributions, as in a crystal, is given in Ref. [55].

Considering typical values of V in condensed matter, FSEs can be strongly suppressed by operating at high momentum transfers such as those available on the VESUVIO spectrometer at ISIS (*e.g.*, 20 Å^{-1} $< Q <$ 250 Å^{-1}) [11]. In practice, it is necessary to assess the quantity expressed by Eq. (18). To this end, one measures an experimental NCP at an individual (fixed) scattering angle l on the instrument, hereafter denoted as $F_l(y,Q)$, where we note that Q is a function of both l and energy transfer. As such, Q can be evaluated directly from a knowledge of these two variables (see also Section 2.3.2). As an experimental observable, $F_l(y,Q)$ can be further decomposed into two terms with and without an explicit Q-dependence, that is, [1]

$$F_l(y,Q) = [J(y) + \Delta J_l(y,Q)] \otimes R_l(y,Q) \tag{20}$$

where $J(y)$ is the longitudinal NCP in the IA limit, $\Delta J_l(y,Q)$ represents all Q-dependent FSEs introduced in Eq. (18), and $R_l(y,Q)$ is a fixed-angle instrumental resolution function (see Section 2.3.2). The convolution product $\otimes$ shown in this expression is an approximation, and its validity to analyse DINS data quantitatively has been checked in detail in Refs. [56, 57]. With these considerations in mind, $F_l(y,Q)$ line shapes are then analyzed to determine the momentum distribution and mean kinetic energy of the system under study. In closing this section, we note that the use of $J(y)$ and $F(y)$ (and their variants) to either denote theoretical or experimental NCPs is a useful one, although the literature has not been consistent in this choice. Likewise, $J(y)$ and $J(y,\hat{\mathbf{Q}})$ implicitly assume that the IA holds, whereas $J(y,\vec{\mathbf{Q}})$ does not assume the validity of this approximation. In what follows, we shall adhere to these conventions, and alert the reader otherwise when referring to published results.

2.1.2. Momentum distributions and mean kinetic energies

The isotropic NCP under the IA, $J(y)$, and its associated NMD, $n(p)$, are obtained by a full analysis of DINS experimental data via a simultaneous fit of individual $F_l(y,Q)$ line shapes with suitable model functions for $J(y,Q)$. Two parametric methods of analysis have been extensively used to date, namely: (a) model-independent functions using a Gauss-Hermite (or Gram-Charlier-type) expansion [1, 50]; and (b) a three-dimensional anisotropic Gaussian line shape corresponding to a quasi-harmonic picture of the effective potential energy surface [58, 59].

In case (a) above, one performs the inversion of $J(y,\hat{\mathbf{Q}})$ [see Eq. (13)], formally the Radon transform of $n(\vec{\mathbf{p}})$, so as to obtain the NMD. This inversion is easily accomplished for the cases where $J(y,\hat{\mathbf{Q}})$ is independent of orientation, as in a powder measurement or a fluid [see Eq. (15)]. A mathematically elegant procedure of accomplishing this task was originally introduced by Reiter and Silver [50] starting from the case of a perfectly aligned crystal, and leading to a Gram-Charlier expansion for $J(y)$ of the form:

$$J(y) = \frac{\exp[\frac{-y^2}{2\sigma^2}]}{(2\pi\sigma^2)^{\frac{1}{2}}} \sum_n \frac{a_n}{2^{2n}n!} H_{2n}(\frac{y}{\sigma\sqrt{2}}), \tag{21}$$

with a radial NMD

$$n(p) = \frac{\exp[\frac{-p^2}{2\sigma^2}]}{(2\pi\sigma^2)^{\frac{3}{2}}} \sum_n (-1)^n a_n L_n^{\frac{1}{2}}(\frac{p^2}{2\sigma^2}). \tag{22}$$

If the first term in the series (H_2) is omitted in the fitting procedure (that is, a_1 is set to zero), σ determines the kinetic energy, independently of any other terms in the series.

In the second parametric approach, one uses a model function for $J(y,\hat{\mathbf{Q}})$, *i.e.*, a spherically averaged multivariate Gaussian [36, 58–62]. The basic assumption in this case is that the NMD of each individual particle is well approximated by a multivariate Gaussian distribution with three distinct frequencies $\omega_{x,y,z}$ associated with local and orientation-dependent principal axes of the molecule. This approach corresponds to an anisotropic quasi-harmonic model in which the main effects of anharmonicity are subsumed in the effective frequencies ω_i. A more general model which allows for the inclusion of anharmonic terms is given in Ref. [55]. Since DINS experiments give access to the total NMD, *i.e.*, the superposition of the distributions of all particles in the sample, for polycrystalline samples it is reasonable and at the same time insightful to assume that the underlying $n(p)$ arises from the spherical average of an anisotropic multivariate Gaussian distribution which may be written as

$$n(p) = \Big\langle \frac{1}{\sqrt{8\pi^3}\sigma_z\sigma_x\sigma_y} \exp\left(-\frac{p_z^2}{2\sigma_z^2} - \frac{p_x^2}{2\sigma_x^2} - \frac{p_y^2}{2\sigma_y^2}\right) \Big\rangle_\Omega \tag{23}$$

with $\langle ... \rangle_\Omega$ denoting an angular average. This expression involves three parameters – the variances σ_α^2 with $\alpha = x,y,z$. These parameters are related to three effective principal frequencies ω_α via $\sigma_\alpha^2 = \frac{M\omega_\alpha}{2\hbar} \coth \frac{\hbar\omega_\alpha}{2k_BT}$, or to the three components of the quantum kinetic energy via $E_\alpha = \hbar^2\sigma_\alpha^2/2M$. We note that Eq. (22) does not make use of these

frequencies ω_i in an explicit manner, yet it is still possible to find relationships that link either approach [63].

As an example to illustrate the above formalism, we can briefly consider the particular case of the water molecule, which is also covered in more detail in Section 3.1. The high-momentum tail of the NMD is dominated by the highest-frequency mode of vibration, the stretch mode, with the proton moving preferentially along the O–H bond. The measured momentum distribution is an isotropic average of the individual proton distributions. The set of frequencies $(\omega_1, \omega_2, \omega_3)$ can be expressed in terms of weighted averages of stretching, librational, and a mix of bending and librational frequencies [59, 60, 64]. In this context, we stress that although Eq. (21) is of the most general form, it does not allow to discriminate between the effects of anharmonicity along a given direction or to highlight the presence of an underlying anisotropy [50, 55]. In contrast, the second approach introduced above [Eq. (23)] provides a suitable framework to assess the main effects of anharmonicity via a determination of the characteristic frequencies ω_i.

Non-parametric methods to analyse angle-averaged $F_l(y,Q)$s [*cf.* Eq. (20)] and hereafter denoted $\bar{F}(y)$ have also been tested. These approaches use the associated function $\bar{F}(y)y^2$ to derive $\langle E_K \rangle$ in two different ways: (a) from direct numerical integration of the second central moment of $\bar{F}(y)y^2$ [65, 66]; or (b) directly from the mean force $f(x)$, a physical quantity proposed in recent theoretical studies [44, 59]. The latter is a more sensitive quantity which, for a macroscopically isotropic system, is a function of the radial displacement x. The mean force may be written as $f(x) = [-\log n(x)]' - \frac{Mk_BTx}{\hbar^2}$. In this relation, $n(x)$ is the spherical end-to-end distribution, *i.e.*, the Fourier transform of $n(p)$ [Eq. (23)], while the second term is the free-particle contribution which is independent of the environment. The function $f(x)$ can be directly related to the experimental $\bar{J}(y)$ after correcting the measured NCP $\bar{F}(y)$ for FSEs $\Delta J(y,Q)$. The corresponding expression is [44]

$$f(x) = -\frac{Mk_BT}{\hbar^2}x + \frac{\int_0^\infty dy\; y \sin(xy/\hbar)\bar{J}(y)}{\hbar \int_0^\infty dy\; \cos(xy/\hbar)\bar{J}(y)}. \tag{24}$$

The mean kinetic energy $\langle E_K \rangle$ can be decomposed into a free-particle contribution proportional to the temperature and a non-classical excess kinetic-energy term $\langle E_{nc} \rangle$ proportional to the gradient of the mean force evaluated at zero displacement

$$\langle E_K \rangle = \frac{3}{2}k_BT + \langle E_{nc} \rangle \tag{25}$$

A detailed discussion of the link between mean forces and kinetic energies can be found in Ref. [44].

2.2. *Momentum distributions of light and heavy nuclei*

2.2.1. Classical vs. quantum behaviour

The NMD $n(\vec{\mathbf{p}})$ and its associated mean kinetic energy $\langle E_K \rangle$ are intimately related to NQEs, particularly for light nuclides. In the quantum regime, $n(\vec{\mathbf{p}})$ is determined by the degree of localisation of the particle through the uncertainty principle, with temperature typically playing a minor role. In many cases of interest, light atoms like protons (or

deuterons) are localized in an approximately harmonic potential and NQEs are related to their intrinsic zero-point energy (ZPE). Because of the non-commuting character of position and momentum operators in quantum mechanics, the NMD provides a sensitive local probe of the potential energy surface in the vicinity or surroundings of the target nucleus. The details of the shape of the $n(\vec{\mathbf{p}})$ therefore give access to the details of the confining potential for the target particle. In the most favorable situations such as single-crystal specimens, experimental NMD data can be used to obtain an effective, single-particle Born-Oppenheimer potential [67]. In all cases, it provides strong constraints on any model of the potential surface. For illustrative purposes, we recall below some of the most salient features of NMDs associated with classical and quantum particles.

For a classical particle, $n(\vec{\mathbf{p}})$ and $\langle E_K \rangle$ are well-defined physical quantities given by [68]:

$$n(\vec{\mathbf{p}}) = [2\pi M k_B T]^{-3/2} \exp\left[-\frac{p^2}{2Mk_BT}\right] \tag{26}$$

and

$$\langle E_K \rangle = \frac{3}{2} k_B T \tag{27}$$

We note that the same Gaussian functional form for $n(\vec{\mathbf{p}})$ is obtained in the ideal case of a perfectly harmonic and isotropic crystal [69], as well as for a cubic Bravais lattice:

$$n(\vec{\mathbf{p}}) = \left[\frac{4}{3}\pi M \langle E_K \rangle\right]^{-3/2} \exp\left[-\frac{3p^2}{4M\langle E_K \rangle}\right] \tag{28}$$

In this case, $\langle E_K \rangle$ retains a non-trivial temperature dependence linked to the *Vibrational (or phonon) Density Of States* $g(\omega)$ (hereafter VDOS), *i.e.,* to the distribution of the phonon frequencies in the crystal:

$$\langle E_K \rangle = \frac{3\hbar}{4} \int_0^{\omega_D} \omega \; g(\omega) \coth\left(\frac{\hbar\omega}{2k_BT}\right) d\omega \tag{29}$$

with

$$g(\omega) = \frac{1}{3N} \sum_{\vec{\mathbf{q}}} \sum_j \delta\left(\omega - \omega_j(\vec{\mathbf{q}})\right), \tag{30}$$

where the sum over reciprocal lattice vectors $\vec{\mathbf{q}}$ is performed over the entire Brillouin zone and ω_D is the cut-off phonon frequency (*i.e.,* the Debye frequency). In the high-temperature limit ($T \to \infty$), this expression converges to Eq. (27), that is, the NMDs of an ideal gas and a high-temperature harmonic solid coincide [68]. In the limit $T \to 0$, the mean kinetic energy reduces to its (purely quantum) ZPE, $\langle E_K \rangle_0$:

$$\langle E_K \rangle_0 = \frac{3\hbar}{4} \int_0^{\omega_D} \omega \; g(\omega) d\omega \tag{31}$$

which in the two special cases of a *Debye solid* and an *Einstein solid* yield, respectively, $g(\omega) = \frac{3\omega^2}{\omega_D^3}\Theta(\omega_D - \omega) \Rightarrow \langle E_K \rangle_0 = \frac{9}{16}\hbar\omega_D$ and $g(\omega) = \delta(\omega - \omega_E) \Rightarrow \langle E_K \rangle_0 = \frac{3}{4}\hbar\omega_E$. The general case of a crystalline solid is treated in more detail in the next section.

Light nuclei in condensed-matter systems are most significatly affected by NQEs, even at ambient conditions. Examples include particle delocalisation and interference in ^{3}He, ^{4}He and ^{3}He-^{4}He mixtures at low temperatures, isotopic effects in liquid water, the ferroelectric behaviour of potassium dihydrogen phosphate, the formation of high-pressure ice phases, localisation and/or delocalisation effects induced in water confined at the nanoscale or on macromolecular surfaces, *etc.* In general, for a light nuclide such as a proton surrounded by heavier atoms at low temperature, it is reasonable to assume that it occupies its ground state and that many-body effects involving the motion of the heavier (and much slower) atoms may be neglected [70]. In this case, the intrinsic ZPE of the proton immediately leads to a higher $\langle E_K \rangle$ than the classical prediction $\frac{3}{2}k_BT$ (a number of exceptions to this behaviour are treated in Ref. [71]). On a microscopic scale, a striking example of NQEs is the spherically averaged NMD of protons participating in *Hydrogen Bonding* (HB). This NMD is markedly different from a classical Maxwell-Boltzmann distribution, even at temperatures higher than ambient, and it is characterised by an additional nuclear kinetic energy intrinsically linked to the degree of binding of the atom to the surrounding medium. Differences between classical and quantum NMDs can also be significant for heavier nuclides, as illustrated in Fig. 3 for the case of D and O atoms in heavy water. For the level of agreement shown in this figure, it is necessary to make recourse to state-of-the-art *Path Integral Molecular Dynamics* (PIMD) methods using first-principles *Density Functional Theory* (DFT). The use of these theoretical and computational tools in the context of DINS are discussed in more detail in Sections 2.2.2 and 2.2.3.

A simple example serves to illustrate how NQEs underpinning nuclear motions go well beyond any semiclassical approach, at least to order $\hbar^2$. To this end, we can estimate semiclassical quantum corrections by treating $\hbar$ as a perturbation [72–74]. Explicit corrections in powers of $\hbar^2$ provide an NMD that still conforms to a Gaussian functional form:

$$n(\vec{\mathbf{p}}) = \frac{1}{\sqrt{(2M\pi k_B T^*)^3}} e^{-\frac{p^2}{(2M\pi k_B T^*)}} \tag{32}$$

but with an effective temperature T^* greater than T and given by

$$T^* = T + \frac{\hbar^2}{36Mk_B^2T} \left\langle \nabla^2 V \right\rangle, \tag{33}$$

In Eq. (33), M is the mass of the particle and $\left\langle \nabla^2 V \right\rangle$ is the average of the Laplacian of the potential energy. If one applies the above approach to protons in polycrystalline ice *Ih* close to melting ($T = 271$ K) using a quasi-harmonic potential for V with a single effective frequency $\bar{\omega}$ (an average value for stretch, bend, and librational modes), a value

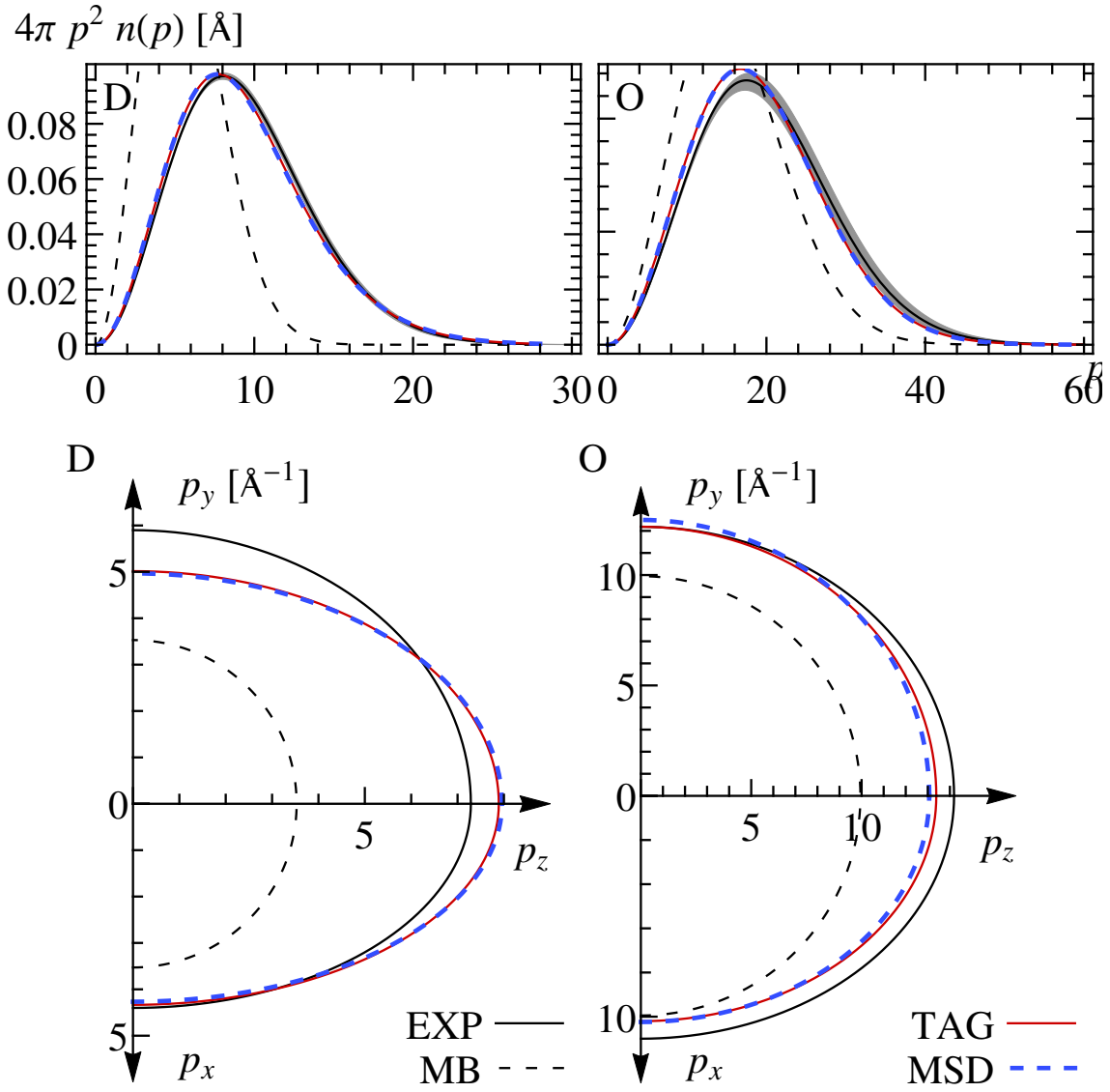

Figure 3. NMDs for D (left) and O (right) in heavy water at 300 K: DINS measurements (EXP); classical Maxwell-Boltzmann distribution (MB); and two different computational PIMD predictions (TAG,MSD). The top panels show the radial NMDs, where $n(p)$ has been multiplied by the Jacobian $4\pi p^2$ to represent a net probability for the atom to have a given momentum p. The shaded area around the experimental data (EXP) represents confidence bands. The directional character of the NMDs is explored in the lower two panels, showing NMD isosurfaces on the xz and yz planes. Cartesian coordinates refer to the direction of the principal components of the quantum kinetic energy tensor. For a liquid, these have been estimated using two procedures (TAG and MSD), as described in detail in Ref. [36]. Contour lines have been chosen such that values at the intercepts correspond to σ_α. Reproduced with permission from Ref. [36].

of $T^* \approx 850$ K is obtained. This effective temperature corresponds to $\langle E_K \rangle \approx 110$ meV, well below the value of $\langle E_K \rangle \approx 154$ meV obtained via DINS measurements [59]. Although this prediction is clearly in the right direction relative to the classical prediction, it also highlights that this simple model cannot describe the inherent anisotropy of the kinetic-energy tensor in ice [75]. In addition, the mean kinetic energy of oxygen in this ice phase predicted by this semiclassical approach amounts to $\langle E_K \rangle \approx 43$ meV, sensibly lower than the value of 56 meV predicted from accurate PIMD simulations [60]. These

examples amply demonstrate how a quantitative description of NQEs associated with proton NMDs in ubiquitous materials like ice and liquid water requires a framework well beyond any classical or semiclassical approach. In weakly quantum systems, corrections of order $\hbar^2$ can be incorporated into the $n(\vec{\mathbf{p}})$ so that a Gaussian line shape is still retained with an effective temperature T^* higher than T. In systems composed of pure He isotopes and their mixtures, the corresponding $n(\vec{\mathbf{p}})$ is nonetheless seen to deviate signicantly from Maxwell-Boltzmann predictions, depending on the specific nature and relative magnitude of the underlying NQEs.

The relations for $\langle E_K \rangle$ and $g(\omega)$ presented above can be also generalized to a wider class of systems, to describe the motion of any atom either in solids or in liquids, including strongly anharmonic solid phases and dense fluids. A discussion of these cases is deferred to Section 2.2.3, after introducing the simpler case of crystalline solids within the harmonic approximation in the next section.

2.2.2. Application to crystalline materials

Building upon the conceptual and theoretical framework presented above, the calculation of NMDs is most conveniently accounted for by considering the *atom-Projected (or Partial) Vibrational Density of States* (PVDOS). Provided that a phonon picture of atomic motions is valid, a crystalline material characterised by long-range order is a suitable starting point to develop the requisite formalism leading to the *ab initio* prediction of DINS observables using first-principles electronic structure methods and, in particular, DFT calculations. In phonon calculations using DFT Perturbation Theory (DFPT), for example, the dynamical matrix is solved directly for a given reciprocal lattice vector $\vec{\mathbf{q}}$ [77]. Due to the variational nature of the DFT formalism, the DFPT problem can be solved by minimizing the second-order perturbation to the total energy yielding first-order variations to the electronic density, wavefunctions, and potential. For the benefit of the unfamiliar reader, this section provides a summary of this increasingly important area of activity in DINS work and refer the reader to Refs. [2, 78] for further details. Those comfortable with the formalism associated with the theory of vibrations in solids and how it applies to DINS may skim over this section.

A phonon description of lattice vibrations implies a number of approximations worthwhile recalling in some detail. First of all, it is assumed that the mean equilibrium position of atom i, $\vec{\mathbf{r}}_i$, is uniquely defined. Secondly, it is assumed that the amplitude of atomic displacements is small compared to interatomic distances, naturally leading to the harmonic approximation for atomic displacements. With these approximations in mind, a description of the vibrational properties of the crystal only requires knowledge of one fundamental quantity, namely, the force-constant matrix [79]

$$D_{\mu\nu}(\vec{\mathbf{r}} - \vec{\mathbf{r}}') = \frac{\partial^2 E}{\partial u_\mu(\vec{\mathbf{r}}) \partial u_\nu(\vec{\mathbf{r}}')}|_{\vec{\mathbf{u}}=0} \tag{34}$$

where $\vec{\mathbf{u}}$ refers to the displacement of a given atom from its equilibrium position and E is the total energy within the harmonic approximation. The force-constant matrix can also be represented in reciprocal space leading to the so-called dynamical matrix

$$D_{\mu\nu}(\vec{\mathbf{q}}) = \frac{1}{N_R} \sum_{\vec{\mathbf{r}},\vec{\mathbf{r}}'} \frac{1}{\sqrt{M_\mu M_\nu}} D_{\mu\nu}(\vec{\mathbf{r}} - \vec{\mathbf{r}}') \exp(-i\vec{\mathbf{q}} \cdot (\vec{\mathbf{r}} - \vec{\mathbf{r}}')). \tag{35}$$

where N_R is the number of lattice sites. With these definitions, equations of motion can be written in the language of dynamical matrices as an eigenvalue problem. Each atomic displacement is described as a plane wave of the form

$$\vec{\mathbf{u}}(\vec{\mathbf{r}},t) = \vec{\mathbf{e}}(\vec{\mathbf{q}})\exp(-i(\vec{\mathbf{q}}\cdot\vec{\mathbf{r}} - \omega(\vec{\mathbf{q}})t)) \tag{36}$$

where the polarisation vector of each mode, $\vec{\mathbf{e}}(\vec{\mathbf{q}})$, is an eigenvector of a $3N$-dimensional eigenvalue problem describing all possible vibrational modes. The eigenvalue equation reads

$$\omega(\vec{\mathbf{q}})^2\vec{\mathbf{e}}(\vec{\mathbf{q}}) = D(\vec{\mathbf{q}})\vec{\mathbf{e}}(\vec{\mathbf{q}}). \tag{37}$$

Phonon dispersion relations are obtained by mapping the wave-vector ($\vec{\mathbf{q}}$) dependence of the frequency eigenvalues $\omega(\vec{\mathbf{q}})$. To achieve the above, we shall assume that the NMD of the n^{th} nucleus in a crystal along the $\hat{\mathbf{q}}$ direction assumes a purely multivariate Gaussian functional form. As introduced earlier, this so-called 'Gaussian approximation' has already been demonstrated to work very well for molecular systems like crystalline HCl [57]. In essence, the Gaussian approximation reflects the essentially harmonic nature of the potential energy surface in the vicinity of the equilibrium position. In this case, the second moment of the NMD for a given nucleus n and along a given direction $\hat{\mathbf{q}}$, $\sigma_n^2(\hat{\mathbf{q}})$, can be written as

$$\sigma_n(\hat{\mathbf{q}})^2 = \frac{M_n}{N_q\hbar^2}\sum_{\vec{\mathbf{q}}\in 1BZ}\sum_{\lambda=1}^{N_\lambda}\times$$
$$(\vec{\mathbf{e_n}}(\lambda,\vec{\mathbf{q}})\cdot\hat{\mathbf{q}})^2(\frac{\omega(\lambda,\vec{\mathbf{q}})}{2})\coth\left(\frac{\omega(\lambda,\vec{\mathbf{q}})}{2k_BT}\right), \tag{38}$$

where $\omega(\lambda,\vec{\mathbf{q}})$ are phonon frequencies and $\vec{\mathbf{e_n}}(\lambda,\vec{\mathbf{q}})$ are polarisation vectors for a given nucleus n. The summation in Eq. (38) runs over all $\vec{\mathbf{q}}$ vectors contained in the first Brillouin zone (1BZ), where N_q is the number of these wave vectors, as well as over the total number of phonon branches N_λ.

From Eq. (38), the spherically averaged value of the second moment of the NMD for nucleus n, σ_n^2, can be obtained using two different routes. In the first route, the spherical average is calculated analytically from Eq. (38) using the following expression [80]

$$\sigma_n^2 = \frac{1}{3}(\sigma_n(\hat{\mathbf{x}})^2 + \sigma_n(\hat{\mathbf{y}})^2 + \sigma_n(\hat{\mathbf{z}})^2) \tag{39}$$

In the second route, the PVDOS of nucleus n, $g_n(\omega)$, is used to compute σ_n^2 explicitly using the relation

$$\sigma_n^2 = \frac{M_n}{\hbar^2}\int g_n(\omega)\frac{\omega}{2}\coth\left(\frac{\omega}{2k_BT}\right)d\omega, \tag{40}$$

The PVDOS, $g_n(\omega)$, is defined as the contribution from a given atom to the total

VDOS. $g_n(\omega)$ is defined by the following sum over all $\vec{\mathbf{q}}$ vectors in the 1BZ and over all phonon bands [81, 82]

$$g_n(\omega) = \frac{1}{3N_q} \sum_{\vec{\mathbf{q}} \in 1BZ} \sum_{\lambda=1}^{N_\lambda} \vec{\mathbf{e_n}}(\lambda, \vec{\mathbf{q}})^2 \delta(\omega - \omega(\lambda, \vec{\mathbf{q}})) \tag{41}$$

where $\vec{\mathbf{e_n}}(\lambda, \vec{\mathbf{q}})$ are the polarisation vectors defined above associated with a mode λ of energy $\omega(\lambda, \vec{\mathbf{q}})$ and N_q is the number of points in the 1BZ.

The PVDOS, $g_n(\omega)$, for a harmonic solid can also be used to estimate the magnitude of FSEs introduced in Section 2.1.1. The spherical average of the Laplacian of the local effective potential felt by nucleus n can be obtained from [83]

$$\langle \nabla^2 V_n \rangle = \frac{3M}{\hbar^2} \int \omega^2 g_n(\omega) d\omega. \tag{42}$$

For an isotropic three-dimensional harmonic oscillator (3D-HO), this quantity is given by [83, 84]

$$\frac{M\langle \nabla^2 V \rangle}{36\hbar^2 Q} = \frac{\sigma^4}{3Q}, \tag{43}$$

where we recall that Q refers to the modulus of the scattering wave vector introduced in earlier sections. Assuming a Gaussian line shape for $J(x)$ with $x = \frac{y}{\sqrt{2\sigma^2}}$, taking its third derivative with respect to y and using the definition of the third-order Hermite polynomial leads to

$$\frac{M\langle \nabla^2 V \rangle}{36\hbar^2 Q} \frac{d^3}{dy^3} J(x) = -\frac{\sigma}{Q} \frac{\sqrt{2}}{12} H_3(x) J(x). \tag{44}$$

FSE contributions beyond the IA can then be written as

$$\Delta J(x, Q) = -\frac{k}{Q} H_3(x) J(x), \tag{45}$$

that is, we have established an explicit connection between the parameter k describing FSEs and the standard deviation of the NMD for a harmonically bound nucleus, namely,

$$k = \sigma \frac{\sqrt{2}}{12}. \tag{46}$$

Equation (46) is useful in the analysis of measured NMDs using the Gram-Charlier expansion. In this case, the parameter k can be relaxed during the fitting procedure and then compared with a prediction based on a purely harmonic system. Also, a comparison of the spherical average of the Laplacian of the effective Born-Oppenheimer potential as obtained from our *ab initio* calculations [*cf.* Eq. (42)] with the value calculated in the

limit of an isotropic 3D-HO allows us to assess the validity of the harmonic approximation in specific situations.

Using the expression for the PVDOS given by Eq. (41) and plugging it back into Eq. (42) for the spherical average of the Laplacian of the effective potential for nucleus n yields an expression for the Laplacian in terms of polarisation vectors $\vec{\mathbf{e}}_{\mathbf{n}}(\lambda, \vec{\mathbf{q}})$

$$\langle \nabla^2 V_n \rangle = \frac{M_n}{N_q \hbar^2} \sum_{\vec{\mathbf{q}} \in 1BZ} \sum_{\lambda=1}^{N_\lambda} \langle \vec{\mathbf{e}}_{\mathbf{n}}(\lambda, \vec{\mathbf{q}})^2 \rangle \omega(\lambda, \vec{\mathbf{q}})^2 \tag{47}$$

Moreover, recalling that

$$\langle \nabla^2 V_n \rangle = \frac{1}{3} \left(\frac{\partial^2 V_n}{\partial x^2} + \frac{\partial^2 V_n}{\partial y^2} + \frac{\partial^2 V_n}{\partial z^2} \right) \tag{48}$$

and

$$\langle (\vec{\mathbf{e}}_{\mathbf{n}}(\lambda)^2 \rangle = \frac{1}{3} (\vec{\mathbf{e}}_{\mathbf{n}}(\lambda, \hat{x})^2 + \vec{\mathbf{e}}_{\mathbf{n}}(\lambda, \hat{y})^2 + \vec{\mathbf{e}}_{\mathbf{n}}(\lambda, \hat{z})^2) \tag{49}$$

leads us to

$$\frac{\partial^2 V_n}{\partial u^2} = \frac{M_n}{N_q \hbar^2} \sum_{\vec{\mathbf{q}} \in 1BZ} \sum_{\lambda=1}^{N_\lambda} \vec{\mathbf{e}}_{\mathbf{n}}(\lambda, \hat{\mathbf{u}})^2 \omega(\lambda, \vec{\mathbf{q}})^2 \tag{50}$$

where $\hat{\mathbf{u}} = \{\hat{\mathbf{x}}, \hat{\mathbf{y}}, \hat{\mathbf{z}}\}$. Equation (50) provides a useful recipe for the *ab initio* modeling of the anisotropy of the effective Born-Oppenheimer potential from phonon dispersion relations in both molecules and condensed-matter systems.

We illustrate the formalism presented above by examining NMDs in crystalline LiH and its deuterated counterpart LiD, two isoelectronic and isostructural insulators characterized by distinctly different vibrational manifolds. LiH exhibits one of the largest-known isotope effects upon hydrogen/deuterium (H/D) substitution in terms of lattice parameters, elastic constants, and Debye temperatures [85]. In this spirit, solid LiH and LiD therefore can offer a direct comparison between first-principles predictions and experimental DINS data. This comparison is facilitated by the high symmetry of its face-centered-cubic crystal structure, shown in Fig. 4.

Ab initio calculations for solid LiH and LiD were performed using Plane-Wave DFT (PW-DFT) and the generalized-gradient-approximation functional of Perdew, Burke, and Ernzerhof [86]. From these electronic-structure calculations, NMD observables are obtained via the computation of phonon dispersion relations and PVDOSs for face-centered-cubic LiH and LiD crystals. A summary of the results of these calculations is given in Figs. 5 and 6.

From the simulated phonon dispersion data within the 1BZ, phonon frequencies $\omega(\lambda, \vec{\mathbf{q}})$ and polarisation vectors $\vec{\mathbf{e}}_{\mathbf{n}}(\lambda, \vec{\mathbf{q}})$ were numerically calculated for all phonon branches. NMD widths σ_n for each atom type along each Cartesian direction (cf. Fig. 4) were calculated using Eq. (38). Finally, the isotropic average was performed for each nucleus within the unit cell using Eq. (39). As a check of these calculations, the isotropic average

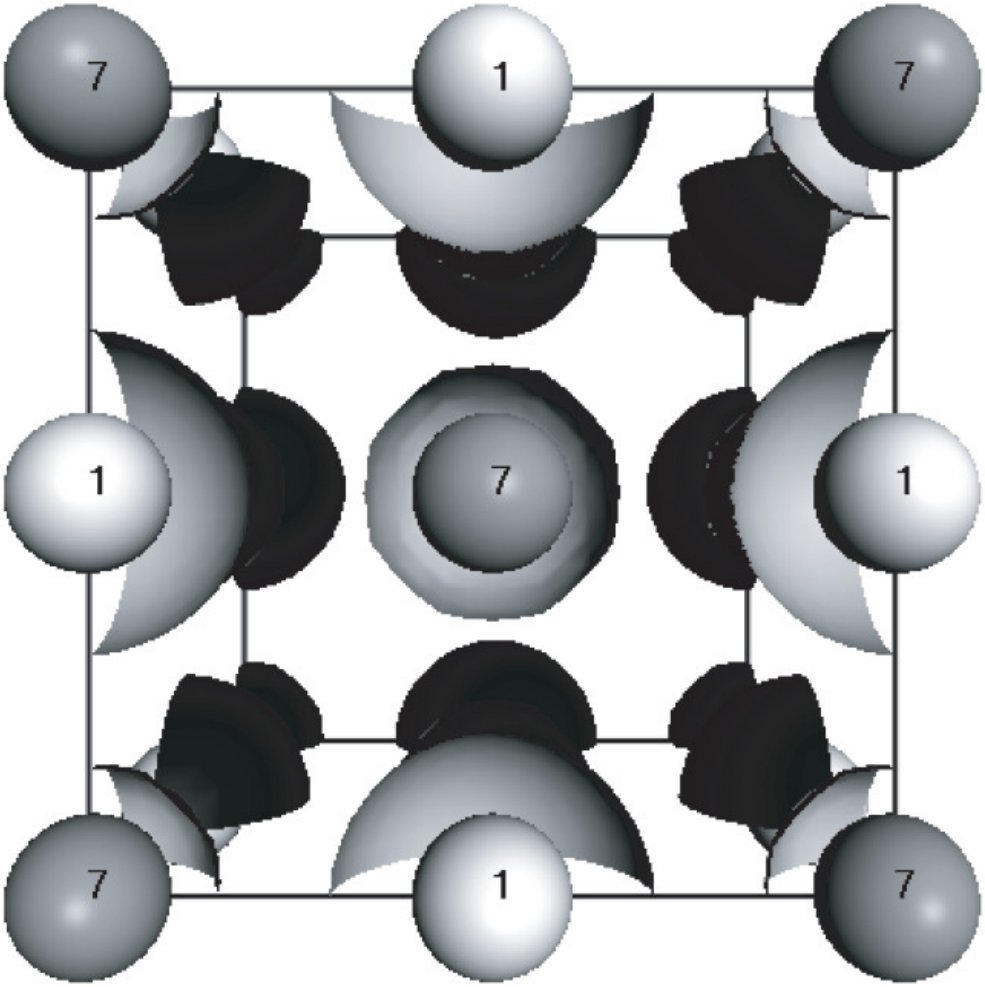

Figure 4. Structure of LiH used as input for the PW-DFT calculations explained in detail in the main text. The numbers indicate the atomic masses for ^{7}Li and ^{1}H. The concentric shells depict the predominantly isotropic character of the total electron density around a given atom, consistent with a formal oxidation state of +1 and -1 for Li and H, respectively, and the non-directional character of ionic bonding in this material.

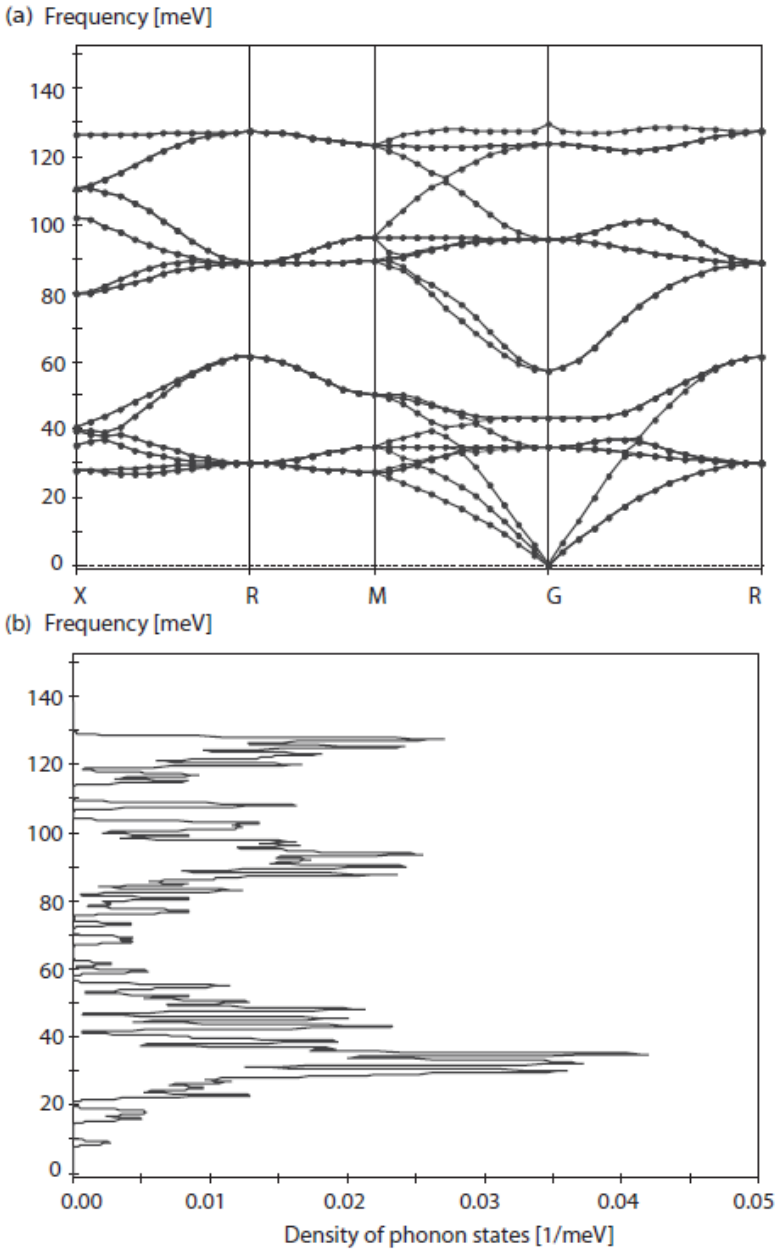

Figure 5. (a) LiH phonon-dispersion curves and (b) total VDOS. To facilitate comparison between (a) and (b), both figures share the same ordinate (energy) axis.

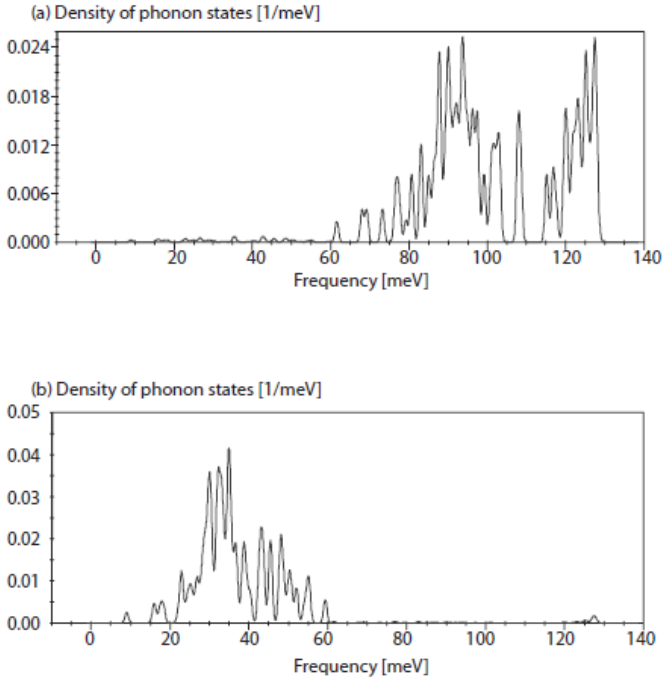

Figure 6. PVDOSs for LiH: (a) H and (b) Li.

of the width of the NMD, σ_n, calculated using Eq. (40) was also compared to the value obtained from Eq. (38).

The standard deviations of the NMDs along the $\hat{\mathbf{x}}$, $\hat{\mathbf{y}}$, and $\hat{\mathbf{z}}$ directions for LiH and LiD are reported in Tables 1 and 2, respectively. The values of σ were calculated for two distinct temperatures, 20 K and 300 K, using Eq. (38). The average isotropic widths calculated using Eq. (39) for each individual atom without imposing any symmetry constraints in the DFT calculations can also be compared to values obtained using Eq. (40), both of which lead to the same result within small numerical errors. As a consistency check, it is worth mentioning that the calculation yields values for the widths of the NMDs that are the same to within 1-2% for all identical nuclei within the LiH and LiD unit cells, as one would expect on the grounds of the cubic symmetry of this material.

Table 3 lists theoretical predictions for H and Li nuclei in LiH and LiD at 20 K and 300 K. These values have been obtained using *ab initio* PVDOSs and Eq. (40), and correspond to the average kinetic energy and the square root of the second moment of the NMD.

Similarly, Table 4 lists the theoretical values for H and Li atoms in LiH and LiD for the directional components of the Laplacian of the effective Born-Oppenheimer potential (*cf.* Eq. 50). In addition, we also report the spherical average of the Laplacian, $\langle \nabla^2 V \rangle$, obtained from the phonon dispersion relations [cf. Eq. (47)], and from the PVDOSs [cf. Eq. (42)]. A comparison of the latter two values provides a sound consistency check of the validity of our *ab initio* calculations for both LiH and LiD. In both LiH and LiD, the components of the Laplacian along all crystallographic directions do not differ from the spherical average by more than 5%. Thus, the effective Born-Oppenheimer potential

Table 1. NMD widths along $\hat{\mathbf{x}}$, $\hat{\mathbf{y}}$, and $\hat{\mathbf{z}}$ for all nuclei in the LiH cell shown in Fig. 4. These widths have been calculated using Eq. (38). The average isotropic widths shown in the last column have been calculated using Eq. (39).

nucleus n	$\sigma_n(\hat{\mathbf{x}})$ [Å^{-1}]		$\sigma_n(\hat{\mathbf{y}})$ [Å^{-1}]		$\sigma_n(\hat{\mathbf{z}})$ [Å^{-1}]		σ_n [Å^{-1}]	
	20 K	300 K	20 K	300 K	20 K	300 K	20 K	300 K
H	3.53	3.60	3.39	3.57	3.44	3.53	3.49	3.57
H	3.53	3.60	3.39	3.57	3.44	3.53	3.49	3.57
H	3.53	3.60	3.39	3.57	3.44	3.53	3.49	3.57
H	3.53	3.60	3.39	3.57	3.44	3.53	3.49	3.57
Li	5.66	7.18	5.60	7.15	5.51	7.10	5.59	7.14
Li	5.66	7.18	5.60	7.15	5.51	7.10	5.59	7.14
Li	5.66	7.18	5.60	7.15	5.51	7.10	5.59	7.14
Li	5.66	7.18	5.60	7.15	5.51	7.10	5.59	7.14

Table 2. NMD widths along $\hat{\mathbf{x}}$, $\hat{\mathbf{y}}$, and $\hat{\mathbf{z}}$ for all nuclei in the LiD cell shown in Fig. 4. These widths have been calculated using Eq. (38). The average isotropic widths shown in the last column have been calculated using Eq. (39).

nucleus n	$\sigma_n(\hat{\mathbf{x}})$ [Å^{-1}]		$\sigma_n(\hat{\mathbf{y}})$ [Å^{-1}]		$\sigma_n(\hat{\mathbf{z}})$ [Å^{-1}]		σ_n [Å^{-1}]	
	20 K	300 K	20 K	300 K	20 K	300 K	20 K	300 K
D	4.19	4.47	4.15	4.44	4.09	4.39	4.14	4.43
D	4.19	4.47	4.15	4.44	4.09	4.39	4.14	4.43
D	4.19	4.47	4.15	4.44	4.09	4.39	4.14	4.43
D	4.19	4.47	4.15	4.44	4.09	4.39	4.14	4.43
Li	5.69	7.18	5.62	7.15	5.52	7.10	5.61	7.15
Li	5.69	7.18	5.62	7.15	5.52	7.10	5.61	7.15
Li	5.69	7.18	5.62	7.15	5.52	7.10	5.61	7.15
Li	5.69	7.18	5.62	7.15	5.52	7.10	5.61	7.15

Table 3. Average kinetic energies $\langle E_K \rangle$ and NMD widths σ for H and Li in LiH and LiD.

nucleus	$\langle E_K \rangle$ [meV]		σ [Å^{-1}]	
	20 K	300 K	20 K	300 K
H in LiH	75.8	79.4	3.49	3.57
Li in LiH	28.1	45.9	5.57	7.13
D in LiD	53.4	61.2	4.14	4.43
Li in LiD	28.2	45.9	5.59	7.13

experienced by the nuclei can be considered predominantly isotropic within the accuracy of the present calculations.

Table 5 lists the experimental values obtained for protons in LiH from DINS experiments at 20 K and 300 K on the VESUVIO spectrometer [87], as well as INS measurements on TOSCA [88], a vibrational neutron spectrometer also located at the ISIS Facility, Rutherford Appleton Laboratory, United Kingdom [89]. These data include average kinetic energies ($\langle E_K \rangle$), NMD widths (σ, calculated from $\langle E_K \rangle$), and the spherical average of the Laplacian of the effective Born-Oppenheimer potential ($\langle \nabla^2 V \rangle$), calculated within the isotropic 3D-HO approximation.

From Table 5 it is apparent that PW-DFT *ab initio* calculations using VDOSs within the harmonic approximation provide good estimates of the experimental values for both the kinetic energy and the width of the proton NMD in solid LiH. The value of $\sigma_{\mathrm{H}} = 3.57$ Å^{-1} in LiH obtained from our *ab initio* calculations at T=300 K is only ∼2%

Table 4. Theoretical predictions for the $(\hat{\mathbf{x}}, \hat{\mathbf{y}}, \hat{\mathbf{z}})$ components of the Laplacian of the effective Born-Oppenheimer potential [*cf.* Eq. (50)] and isotropic average of the Laplacian $\langle \nabla^2 V \rangle$. In the last two columns, P denotes calculated values using phonon dispersion relations [cf. Eq. (47)], whereas V corresponds to explicit use of the relevant VDOS [*cf.* Eq. (42)]. All values are given in units of meVÅ^{-2}.

nucleus	$\frac{\partial^2 V_n}{\partial x^2}$	$\frac{\partial^2 V_n}{\partial y^2}$	$\frac{\partial^2 V_n}{\partial z^2}$	$\langle \nabla^2 V \rangle_P$	$\langle \nabla^2 V \rangle_V$
H in LiH	7984	7652	7209	7622	7622
Li in LiH	8602	8137	7378	8055	8053
D in LiD	8033	7664	7202	7641	7642
Li in LiD	8641	8147	7377	8072	8070

Table 5. Experimental values for protons in LiH: average kinetic energies ($\langle E_K \rangle$), NMD widths (σ), and the spherical average of the Laplacian of the effective Born-Oppenheimer potential ($\langle \nabla^2 V \rangle$), all calculated within the isotropic 3D-HO approximation.

T [K]	method	$\langle E_K \rangle$ [meV]	σ [Å^{-1}]	$\langle \nabla^2 V \rangle$ [meV Å^{-2}]
300	DINS [87]	76.0 ± 0.3	3.49 ± 0.05	7382 ± 423
20	DINS [87]	73.8 ± 0.3	3.44 ± 0.05	6968 ± 405
20	INS [88]	80 ± 1	3.59 ± 0.05	8265 ± 460

larger than 3.49 ± 0.05 Å^{-1}, the isotropic average value obtained from previous DINS measurements at the same temperature. Most interestingly, the *ab initio* value of σ_{H} at T=20 K, 3.49 Å^{-1}, is bracketed by previous experimental values for σ_{H}, namely, 3.44 Å^{-1} (DINS measurements), and 3.59 Å^{-1} (INS measurements). Also, the *ab initio* values of the isotropically averaged Laplacians of the effective Born-Oppenheimer potentials in LiH, $\langle \nabla^2 V \rangle$, agree well with those derived from DINS and INS experiments assuming an isotropic 3D-HO model. A theoretical value of $\langle \nabla^2 V \rangle$=7622 meV Å^{-2} for H in LiH is also bracketed by experimental values of 6968 and 8265 and it is only 3% higher than the value measured in DINS experiments at 300 K.

As long as it is possible to define a unit cell with translational invariance, the approach described above can be used to study *any* material regardless of complexity using first-principles periodic DFT methods and phonon calculations for comparison with DINS experiments. To a first-order approximation, the effects of temperature on DINS observables may be accounted for via recourse to the quasiharmonic approximation [90]. This approximation amounts to performing separate phonon calculations for a set of structures that reproduce the thermal expansion of the material [91]. In this spirit, the solid-acid $CsHSO_4$ has been studied in some detail recently using DINS and INS [92]. This material is a superb proton conductor above *ca.* 400 K and has already been used as the solid electrolyte in intermediate-temperature fuel cells [93]. $CsHSO_4$ is also an intriguing material in its own right, exhibiting the exclusive formation of a metastable crystalline phase when grown in aqueous protic media at room temperature. The formation of this metastable phase is suppressed when the deuterium-to-hydrogen molar ratio of the aqueous growth medium is higher than 50%, an intriguing isotope effect which has defied a microscopic explanation to date. Figure 7 shows the structure of this phase, and serves to illustrate the increased level of complexity of this material relative to the relatively simple binary hydride presented above.

Table 6 shows a comparison between calculated and classical predictions for spatially averaged NMD widths in $CsHSO_4$. Recalling the concepts introduced in Section 2.2.1, the classical limit is given by

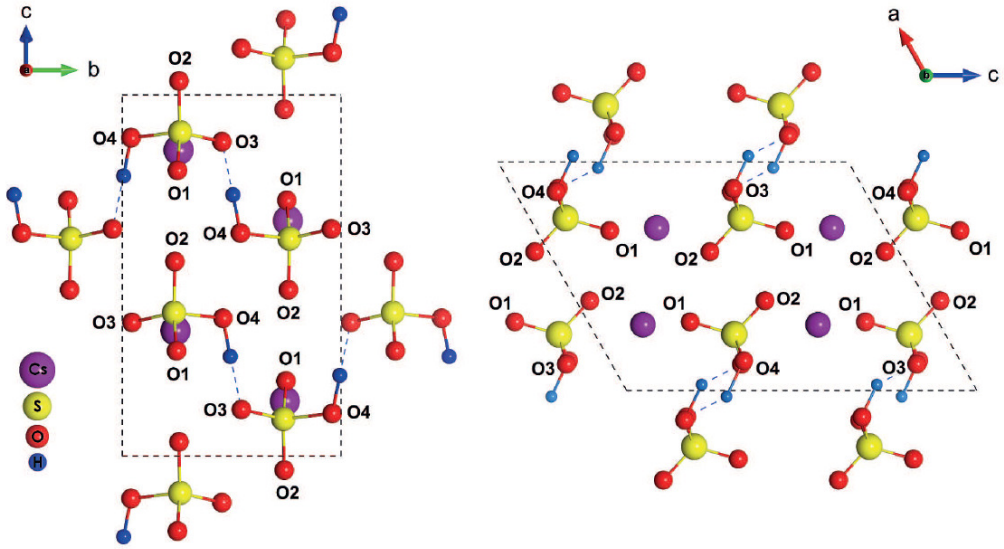

Figure 7. Crystallographic structure of the metastable phase of the proton conductor $CsHSO_4$. Atom types are represented by different colours as shown in the figure: blue (H), red (O), yellow (S), and purple (Cs).

$$\sigma_{cl} = \frac{\sqrt{Mk_BT}}{\hbar} \tag{51}$$

These classical values provide a *lower* bound to this DINS observable, as the spatial confinement arising from chemical-binding forces implies an increase in mean atomic kinetic energies. Phonon calculations, therefore, enable us to capture NQEs to first order in the form of an overall ZPE associated with *all* normal modes of the system projected onto a given atom [*cf.* Eq. 38]. To put these ideas on quantitative grounds, we can define a *Quantum-energy Excess* (QE) as

$$\mathrm{QE} = \frac{\sigma^2}{\sigma_{cl}^2} = \frac{\hbar^2}{Mk_BT}\sigma^2 \tag{52}$$

where we note that this quantity is inversely proportional to temperature T and nuclear-mass M. It is important to note that both of these variables exhibit the same functional dependence as one approaches the classical limit (QE=1). From Table 6, the QEs associated with the proton remain well over unity up to room temperature, a consequence of the predominantly quantum character of this species up to the transition to the stable crystallographic phase around 350 K. As this phase is not observed for the deuterated

Table 6. Comparison of calculated DINS observables for the metastable phase of $CsHSO_4$ relative to classical (Maxwell-Boltzmann) predictions. The atom labels shown in the first column correspond to those shown in Fig. 7. The last column reports the corresponding QE, defined by Eq. (52) in the main text.

nucleus	σ [Å^{-1}]		σ_{cl} [Å^{-1}]		QE	
	10 K	300 K	10 K	300 K	10 K	300 K
H	4.7	4.7	0.5	2.5	92.5	3.6
O1	10.6	12.4	1.8	9.9	34.1	1.6
O2	10.8	12.6	1.8	9.9	35.4	1.6
O3	10.8	12.4	1.8	9.9	35.0	1.6
O4	10.8	12.5	1.8	9.9	35.0	1.6
S	17.7	19.4	2.8	14.1	47.6	1.9
Cs	12.2	28.8	5.2	28.8	5.4	1.0

analogue $CsDSO_4$, this result suggests that differences in ZPEs are related to the emergence of a metastable phase for the H-containing species. At 10 K, the heavier species also exhibit significant NQEs yet we note that S is characterised by a QE that is sensibly higher than that for the lighter O, and these differences are still evident at room temperature. This trend can be traced back to the tetrahedral binding environment around S relative to the peripheral location of O within a given SO_4 unit. Of all atomic species, only Cs has a QE of unity at room temperature. These findings need to be put in the context of the extensive use of classical molecular dynamics simulations to study this material, where atomic species (or sometimes rigid fragments containing well-defined structural units) are treated as classical entities from the outset. Also, these considerations highlight the ability of DINS to provide important insights on the local binding environment around a given species, very similar to those afforded by other techniques such as EXAFS and other X-ray-based spectroscopies [94]. These capabilities have been recently applied to the study of phase polymorphism in organic crystals [95], showing that DINS along with INS, diffraction, and first-principles calculations can provide a powerful means of distinguising between different scenarios associated with either phase coexistence or the progressive onset of dynamical processes as a function of temperature.

It is also noteworthy that the first-principles calculations presented so far to calculate DINS observables using a phonon-based description of the material within the framework of DFT methods are well within the reach of modest computational resources (few processors, of order $2^3 - 2^5$). Much of the progress seen in the development and use of DINS over the past decade is owed to synergies between the use of first-principles materials modelling (particularly DFT) and experiment, as well as on the increasing availability of high-resolution INS data to benchmark these calculations in detail – see, for example, the compilation of over 700 entries in Ref. [96]. The explosive growth experienced by the former in the past few years has made it possible to go beyond heuristic and phenomenological models of the DINS and INS response, and to obtain quantitative estimates using well-defined approximations for the underlying potential energy landscape at a relatively low computational cost. Using well-established and widely available DFT codes, it is possible to treat materials with up to hundreds of atoms per unit cell, yet this upper limit is constantly being improved by developments in DFT methodologies, particularly linear-scaling techniques [97].

All in all, the *ab initio* approach described in this section provides a convenient framework for the prediction of NMDs in solid-state systems, an observable also accessible via DINS measurements. Likewise, such a framework makes it possible to explore in a controlled and systematic fashion those features that contribute to the DINS line shape.

We shall return to this particular (and increasingly important) point in the case studies presented in Section 3.

2.2.3. Beyond phonons and crystalline order

DINS observables can be calculated beyond the harmonic approximation and a perfectly ordered lattice. From a computational viewpoint, a treatment of the latter requires calculations with a sufficiently large simulation cell such that the effects of disorder can be captured adequately by the model. The usual approach involves the calculation of experimental observables as a function of cell size in order to ensure scale invariance. Steady advances in DFT have paved the way to deal with up to a few thousand atoms per unit cell, and it would be interesting to see how these methods could be applied to a number of systems already studied by DINS. These include seminal studies on molecular [98], metallic [99], and proton glasses [100], and more recent studies on molecular and cluster confinement in zeolites [101], or the solid phases of metal-ammonia compounds [102].

Liquids represent the ultimate limit of disorder in condensed matter, and an up-to-date review on NQEs in aqueous systems is given in Ref. [103]. In this case, the existence of well-defined normal modes of vibration cannot be taken generally as a good starting point, and NMDs need to be calculated explicitly in order to obtain DINS observables for comparison with experimental data. To this end, *Path Integral* (PI) methods are used. In essence, PI allows for a numerically exact evaluation of $n(p)$ from the density matrix $\rho(\vec{\mathbf{r}},\vec{\mathbf{r}}') = \langle\vec{\mathbf{r}}|\exp(-\widehat{H}/k_BT)|\vec{\mathbf{r}}'\rangle$ where $\widehat{H}$ is the Hamiltonian operator. In terms of these quantities, the NMD is given by the following orientationally averaged Fourier relationship [104]

$$n(p) = \Big\langle \frac{1}{2\pi\hbar^3}\int d\vec{\mathbf{r}}d\vec{\mathbf{r}}'\exp\big[\frac{i}{\hbar}\vec{\mathbf{p}}(\vec{\mathbf{r}}-\vec{\mathbf{r}}')\big]\frac{\rho(\vec{\mathbf{r}},\vec{\mathbf{r}}')}{Z}\Big\rangle_\Omega \tag{53}$$

where Z is the partition function

$$Z = \int d\vec{\mathbf{r}}\rho(\vec{\mathbf{r}},\vec{\mathbf{r}}) \tag{54}$$

We note that Z is an integral over diagonal terms, whereas $n(p)$ includes off-diagonal elements and, therefore, its evaluation is computationally costly. Increasingly efficient methods continue to be developed to speed up these calculations [44, 45]. In particular, Lin *et al.* [44] have proposed an efficient and physically insightful approach to evaluate the open-path distribution given by Eq. (53) whereby free-particle and environmental contributions may be separated and the latter is related to the free-energy landscape around the atom, thereby facilitating the interpretation of NQEs such as tunelling, particle delocalisation, and isotope effects [105].

The most widely used PI method is PIMD, introduced earlier when discussing NQEs in Fig. 3. Other PI methods include *Ring-Polymer* and *Centroid Molecular Dynamics*, all of which assume the validity of the Born-Oppenheimer approximation to separate nuclear and electronic motions. The essence of these methods is illustrated in Fig. 8, where the description of the quantum problem for nuclear motions is achieved via the use of a number of replicas (or beads) which are connected to each other via harmonic springs in a sequential fashion, and these are propagated in *imaginary time*, *i.e.,* a time-independent quantum system is mapped onto a time-dependent classical one in the limit of an infi-

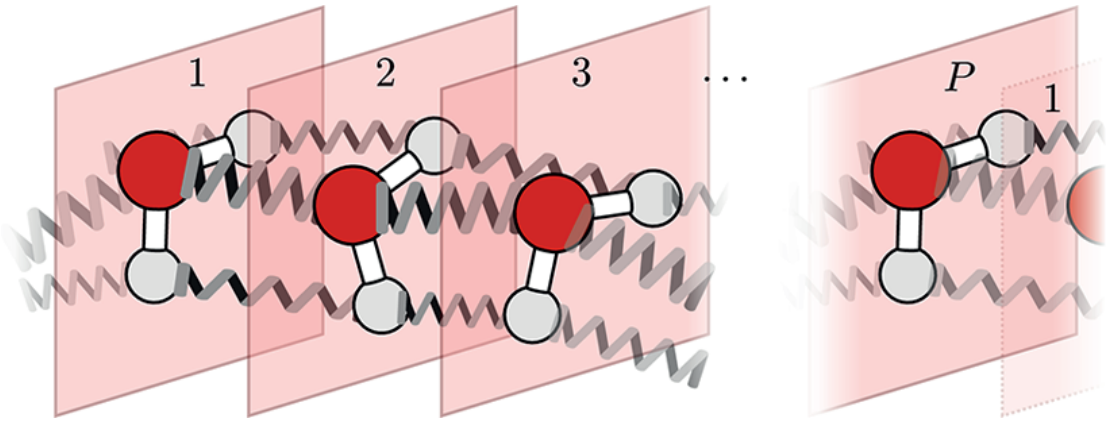

Figure 8. Schematic diagram illustrating the PI method. The water molecule is used as example. Adjacent beads are connected to each other with harmonic springs and the entire ensemble of beads is subjected to periodic boundary conditions. Reproduced from Ref. [103].

nite number of beads. Convergence to this limit needs to be always checked carefully, making these calculations quite costly. New software tools to perform PI are also being developed with a view to their widespread use in conjunction with an increasing number of materials modelling codes [106]. With the exception of quantum-mechanical particle-exchange requiring more sophisticated approaches [107], PI captures all the requisite physics associated with *static* properties at thermodynamic equilibrium of an ensemble of *distinguishable* quantum particles, the NMD being one such quantity. Extension of these methods to the calculation of real-time correlation functions (and, therefore, scattering observables in the INS and QENS regimes) remains an unsolved challenge in chemical physics and is still an active area of research. For a recent review, see Ref. [108]

2.3. *The practice of electron-volt neutron spectroscopy*

2.3.1. The VESUVIO spectrometer

This section provides a detailed description of VESUVIO, a so-called inverted-geometry neutron spectrometer designed to measure NMDs using eV neutrons. We place emphasis on recent technical developments since the field of eV neutron spectroscopy was last reviewed in detail [1]. In its current incarnation, VESUVIO has been operational for about a decade at the ISIS Facility, Rutherford Appleton Laboratory, United Kingdom [11, 29–32]. The neutron energies available on VESUVIO are up to two orders of magnitude

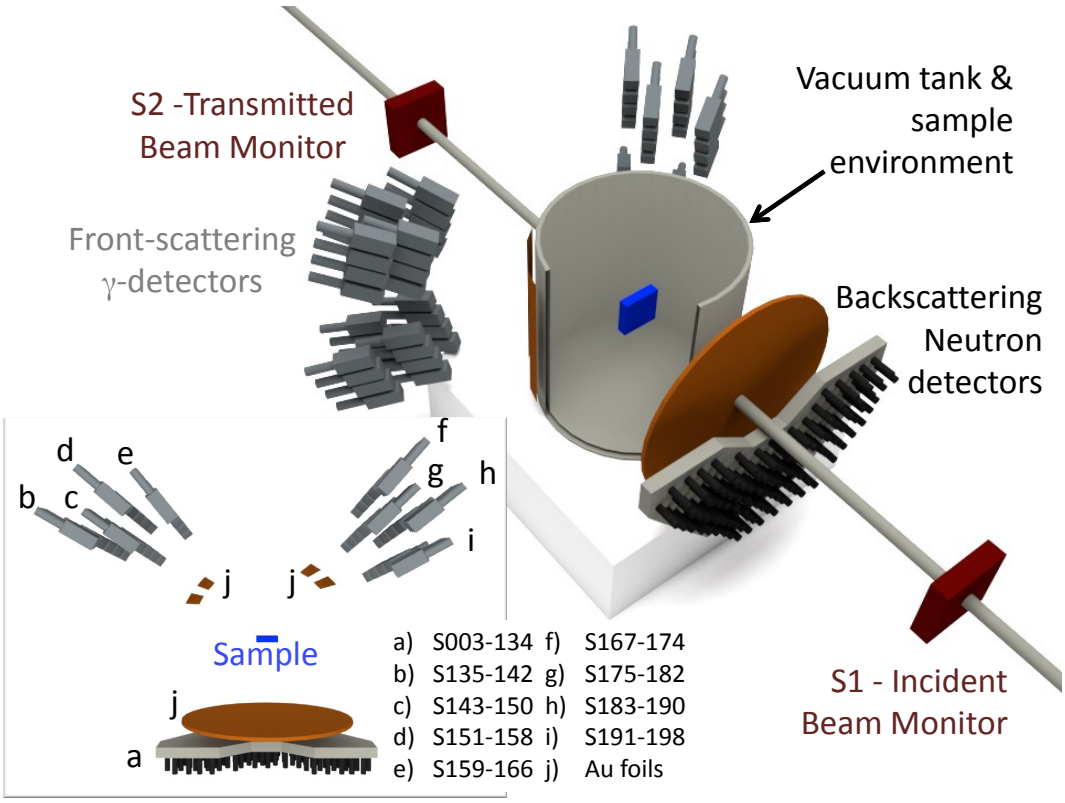

Figure 9. Schematic diagram of the VESUVIO spectrometer. Labels in the main figure describe the main components of the instrument. The inset on the left offers a view from the top, where letters are used to designate the location of different detector banks. The numbers associated with each detector bank indicate the present numbering sequence. For further details, see the main text.

higher than any other neutron instrument in the world currently supporting a science programme. In this context, we note recent and exciting developments associated with the construction and commissioning of a DINS spectrometer at the Bariloche Electron LINAC in Argentina [109–111], as well as initiatives in support of similar instrumentation at the CSNS in China [112] and the SNS in the USA [113]. In terms of energy and momentum transfers, VESUVIO provides routine access to 0.5 eV$< \hbar\omega <$ 150 eV and 20 Å$^{-1} < \hbar Q <$ 300 Å^{-1}, respectively. This wide coverage guarantees that the neutron-scattering regime accessible in the experiments is well within the framework of the IA (see Section 2.1.1). A schematic layout of the instrument is shown in Fig. 9.

As an inverted-geometry spectrometer, VESUVIO uses a polychromatic incident neutron beam characterized by an energy spectrum $I(E_0)$, peaked at about 0.03 eV and with an $E_0^{-0.9}$ tail in the epithermal region, as shown in Fig. 10. A recent upgrade of the water moderator at *ISIS Target Station I* has improved considerably the flux at thermal energies, opening up new opportunities for the simultaneous acquisition of DINS, diffraction, resonant capture, and transmission data over several orders of magnitude in neutron energy. Incident neutrons having initial energy E_0 travel a distance L_0 from the moderator to the sample. After scattering at an angle ϕ, neutrons with final energy E_1 travel a distance L_1 to the detector as schematically shown in Fig. 9 [114–117]. Energy selection on the instrument is performed using a resonance filter after scattering by the sample, typically Au or U foils (see discussion below).

The incident and transmitted beam monitors (S1 and S2 in Fig. 9) consist of beads of ^{6}Li-doped scintillator glass. The instrument is equipped with forward and backscat-

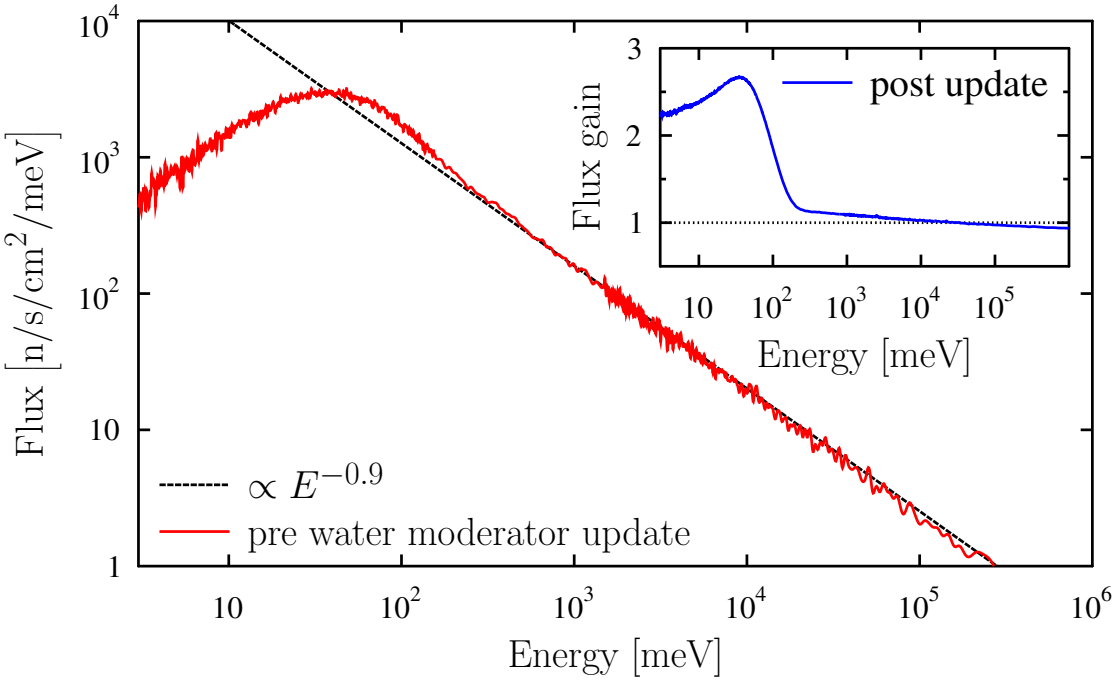

Figure 10. Incident neutron flux on VESUVIO as a function of energy – please note the logarithimic scales for both ordinate and abcissa in the main figure. The dashed black line corresponds to a fit of the experimental data to a power-law of the form $E^{-0.9}$. The inset shows the flux gain as a function of energy following a recent upgrade of the water moderator.

tering detector banks. The forward bank employs 64 Cerium-doped Yttrium Aluminium Perovskite (YAP) γ-ray detectors, at present the best detectors of their kind in terms of efficiency and signal-to-background ratio [12, 14, 18, 19, 21, 118]. These scintillators are located at a distance between 50 and 75 cm from the sample position (S135–S198 in Fig. 9), covering an angular range $33° < \phi < 67°$. YAP is a fast, mechanically rugged, and chemically resistant scintillator material with a density of 5.55 g/cm^3, which ensures a light yield of 18000 photons/MeV and constant detection efficiency as a function of time t. The detector has a short decay time of $\tau = 27$ ns and a wavelength of maximum emission of 350 nm. This material is relatively stable over a wide temperature range and its chemical composition is such that no neutron resonances are present over the range 1-200 eV. An array of 132 ^{6}Li-doped neutron detectors is used for the backscattering bank, arranged in a semicircle below the scattering plane. Located between 45 and 70 cm from the sample position (S3–S134 in Fig. 9), they cover a range of angles $130° < \phi < 163°$. With ^{6}Li, detection efficiencies are roughly proportional to t and count rates are thus significantly reduced at short t.

At present, VESUVIO can operate in two modes, namely, Resonance-Filter (RF) and Resonance-Detector (RD) configurations [1, 119, 120]. Both configurations utilize a so-called analyzer foil of a specific material, such as ^{238}U or ^{197}Au, located in the secondary flight path. This analyzer foil strongly absorbs neutrons within narrow energy intervals around nuclear resonances, thus selecting the energy of the scattered neutrons *i.e.*, $E_1 \sim 4.9 \pm 0.15$ eV for the Au foil currently in use. This tight spectral resolution in the eV region remains unique to inverted-geometry instrumentation like VESUVIO. Reference [121] provides an up-to-date appraisal of the complementarity between VESUVIO-like spectrometers and direct-geometry instruments using mechanical methods to effect

the selection of incident neutron velocities, *e.g.,* use of choppers.

In the RF configuration currently used in backscattering geometry, the analyzer foil is cycled in and out of the scattered neutron beam and two measurements are taken, one with the foil between sample and detector (foil-in) and the other with the foil removed (foil-out). DINS time-of-flight (TOF) spectra correspond to the difference between the two measurements which are collected by ^{6}Li-doped glass detectors, primarily sensitive to neutrons. This standard protocol is referred to as the *Single-Difference* (SD) technique [1, 29]. *Double-Difference* (DD) techniques are also in use on VESUVIO to improve final-energy resolution [122, 123]. With DD techniques, the Lorentzian long tails are largely removed and, thus, energy resolution is improved considerably. More details can be found in Refs. [1, 123].

The RD configuration used in forward scattering geometry employs the foil to define the energy of the scattered neutrons via resonant neutron absorption, and a γ-ray detector to probe the prompt cascade following the subsequent (n,γ) reaction [19]. In the RD configuration, the measurement of the time of arrival of the γ-rays, which coincides with neutron absorption by the foil, allows the determination of the initial neutron energy E_0 through TOF techniques. This configuration is currently the one chosen for the VESUVIO forward-scattering bank using the YAP γ-ray detectors described above, designed to function both as neutron and energy selectors via the use of Au foils placed on the YAP-detector surface. Since γ-ray emission is effectively instantaneous on the timescale of the neutron TOF measurements, both the TOF and the energy E_1 of the absorbed neutron are determined when a γ-ray is detected. By use of a secondary foil placed in two distinct positions, both energy resolution and signal-to-background ratios can be greatly improved. In foil-out measurements, scattered neutrons only see the primary foil, whereas foil-in measurements require them to pass through a secondary foil prior to reaching the primary foil. The secondary Au foil has the same nominal thickness as the primary foil and it is cycled, that is, moved repeatedly between the two positions within a data collection period. This cycling procedure removes drifts in detector efficiency with time caused by, for example, changes in temperature or other environmental factors. The final TOF spectrum in forward scattering is then obtained from subtraction of the foil-in from the foil-out raw data. This method, known as foil-cycling (FC), is illustrated in Fig. 11 [18, 124].

The foil-out neutron count rate at a given detector placed at a scattering angle ϕ is given by:

$$C_{out}(E_0, E_1, \phi) = C(E_0, E_1, \phi)A(E_1)\eta + B_{out}(E_0, E_1, \phi). \tag{55}$$

where η is the probability that the γ-ray cascade is registered by the YAP detector, and B_{out} is the γ background in the absence of the secondary foil. $C(E_0, E_1, \phi)$ is the standard expression for the count rate as a function of TOF on an inverted-geometry spectrometer, *i.e.,* the rate at which scattered neutrons impinge on a given detector after scattering by the sample. This function depends on the incident neutron spectrum and the scattering properties of the sample [*cf.* Eq. (62) in the next section].

For the foil-in measurement, the secondary foil is placed between the scattered neutron beam and detector, so that neutrons have to pass through it to reach the primary foil (see Fig. 11). Hence, the count rate from the primary foil is reduced by the factor $[1 - A(E_1)]$, that is,

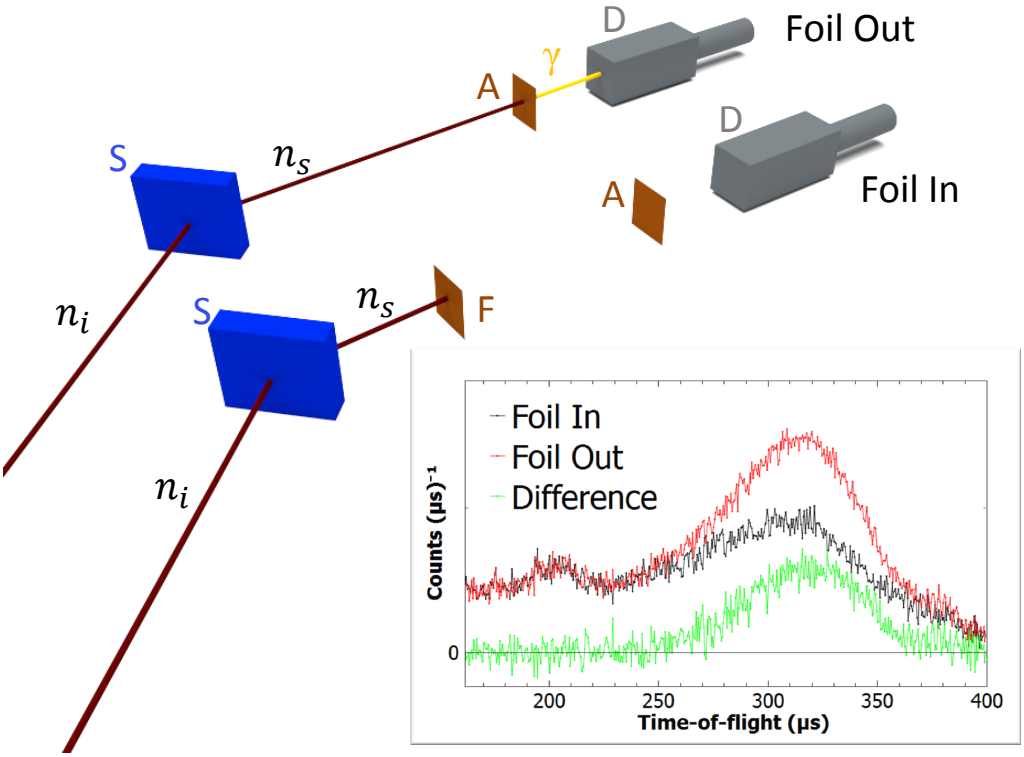

Figure 11. Illustration of the FC technique using a primary Au foil (A) covering the surface of the YAP detector (D) and a movable secondary Au foil (F) of identical thickness. S denotes sample and n_i and n_s correspond to the incident and scattered neutron, respectively. The inset shows the corresponding TOF data from a polythene standard at 300 K with and without the foil, as well the resulting difference in a different scale. For further details, see the main text.

$$C_{in}(E_0, E_1, \phi) = C(E_0, E_1, \phi)[1 - A(E_1)]A(E_1)\eta + B_{in}(E_0, E_1, \phi) \tag{56}$$

where B_{in} is the background in the 'foil-in' configuration. DINS data in TOF correspond to the difference between these two count rates:

$$C_{out}(E_0, E_1, \phi) - C_{in}(E_0, E_1, \phi) = C(E_0, E_1, \phi)A^2(E_1)\eta + [B_{out}(E_0, E_1, \phi) - B_{in}(E_0, E_1, \phi)] \tag{57}$$

This difference method removes most of the γ-ray background and also improves spectral resolution.

In summary, energy resolution is greatly improved with the RD configuration. Furthermore, the energy resolution function in the RF configuration is determined by the absorption profile of the foil $[A(E_1)]$ and has an almost Lorentzian line shape. As can be appreciated from Eq. (57), foil absorption in the RD method appears as $[A(E_1)]^2$, which considerably improves spectral resolution, as illustrated in Fig. 12.

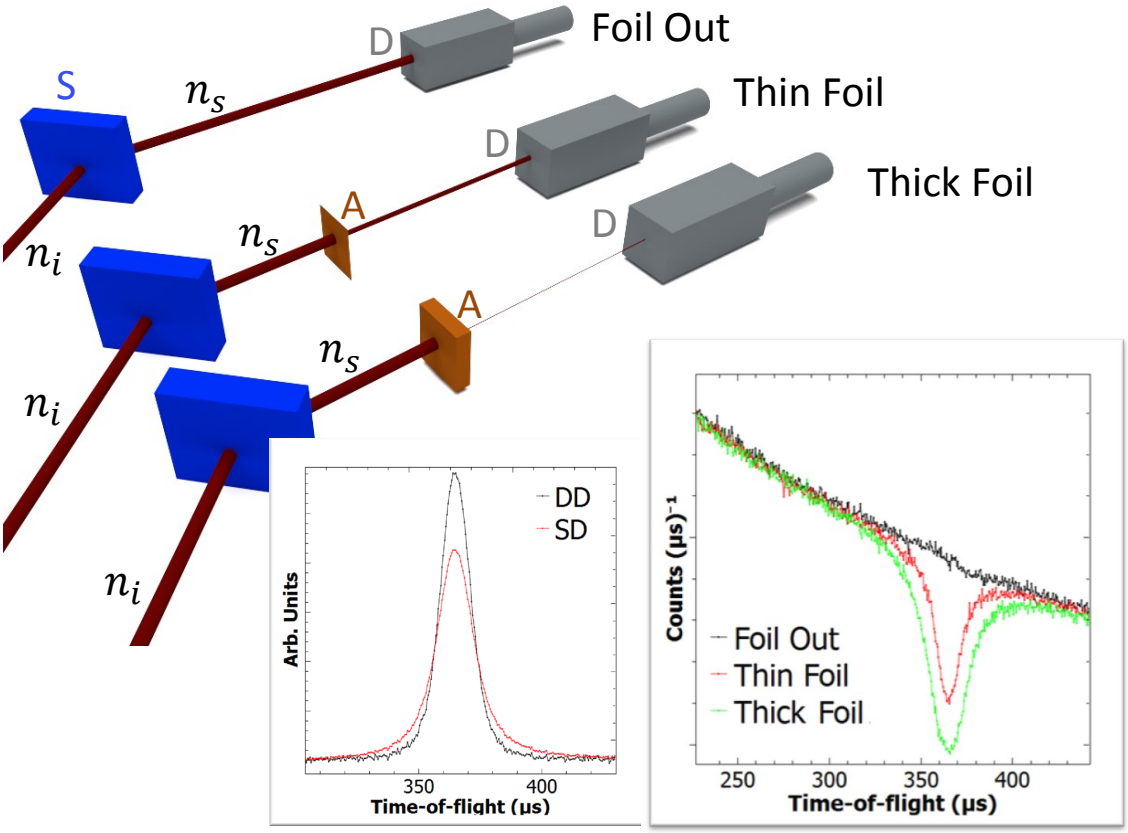

Figure 12. Illustration of the three RD configurations required to make use of both thin and thick foils, also described in more detail in the main text. The inset on the right shows the corresponding raw TOF data in backscattering for Fe at 300 K. The inset on the left shows the subtracted SD and DD data normalised to the same integrated area. DD (black) leads to a strong suppression of the long tails seen with SD (red), and a much-improved spectral resolution.

2.3.2. From raw neutron counts to momentum distributions

The analysis of DINS experiments relies on the application of TOF methods [48]. The total TOF t for a neutron traveling from moderator to a given detector may be obtained from:

$$t - \tau = \frac{L_0}{v_0} + \frac{L_1}{v_1} = A\left(\frac{L_0}{E_0^{1/2}} + \frac{L_1}{E_1^{1/2}}\right) \tag{58}$$

where τ is the time delay introduced by the instrument electronics, L_0 the distance from source to sample, L_1 the distance from sample to detector, v_0 and v_1 the incident and scattered neutron velocities, E_0 and E_1 are the corresponding energies, respectively, and A is a constant equal to 72.3 $\mathrm{eV}^{1/2}\mu\mathrm{s\ m}^{-1}$.

Likewise, energy transfer is defined as:

$$\hbar\omega = E_0 - E_1 \tag{59}$$

and the magnitude of the momentum transfer by:

$$\hbar Q = B\Big(E_0 + E_1 - 2\sqrt{E_0 E_1}\cos\phi\Big)^{1/2} \tag{60}$$

with $B = (\frac{2m}{\hbar^2})^{1/2} = 21.97$ Å^{-1} eV$^{-1/2}$. Equations (58) and (59) can be used to define E_0 for a given scattering angle ϕ in terms of E_1 and t:

$$E_0(E_1, t) = \frac{m}{2}\left(\frac{L_0 v_1}{v_1(t-\tau) - L_1}\right)^2. \tag{61}$$

The standard expression for the count rate as a function of t on an inverse-geometry spectrometer is [48]:

$$C(t) = 2\left(\frac{2}{m}\right)^{1/2}\frac{E_0^{3/2}}{L_0} I(E_0) D(E_1) N \frac{d^2\sigma}{d\Omega dE_1}\Delta\Omega \tag{62}$$

where $I(E_0)dE_0$ is the number of incident neutrons per unit time with energies between E_0 and $E_0 + dE_0$ and $D(E_1)$ is the probability that a neutron of energy E_1 is detected. N is the number of atoms illuminated by the incident beam, $\frac{d^2\sigma}{d\Omega dE_1}$ the double differential scattering cross section defined earlier via Eq. (1), and $\Delta\Omega$ the solid angle subtended by a given detector. Combining Eqs. (62) and (11) for a sample containing different atoms of mass M, and introducing a mass-dependent resolution function $R_M(t)$, one can write:

$$C(t) = \frac{E_0 I(E_0)}{Q}\sum_M A_M M J_M(y_M) \otimes R_M(t) \tag{63}$$

where

$$A_M = [\frac{2}{L_0} D(E_R)\sqrt{\frac{2E_R}{m}}\Delta\Omega] N_M b_M^2 \tag{64}$$

with b_M^2 related to the 'free' total scattering cross section via the expression $\sigma_M^2 = \frac{4\pi b_M^2}{[1+\frac{M}{m}]^2}$ [2]. DINS measurements as currently implemented on VESUVIO give access to scattered intensities as a function of energy ($\hbar\omega$) and momentum transfer ($\hbar Q$). We also recall that the convolution product $\otimes$ constitutes an approximation whose validity has been tested thoroughly in the context of VESUVIO data analysis [56, 57] – *cf.* Eq. (20) in Section 2.1.1. Through the TOF profiles as a function of scattering angle ϕ [see Eq. (58)], it becomes possible to explore NMDs in a quantitative manner. For systems comprising of more than one nuclide, DINS can then be viewed as a (rather unique!) mass-spectroscopic technique where each nucleus in the sample contributes to the overall TOF spectrum as a Doppler-broadened recoil peak (see Section 2.3.3 below). Representative recoil data are shown in Fig. 13 to illustrate different yet, at the same time, equivalent ways of treating the experimental data (left panels), as well as the ability to separate the response from different masses.

Beyond recoil scattering, Figure 14 illustrates the plethora of information given by an instrument like VESUVIO, emphasizing the *concurrent* nature of these measurements.

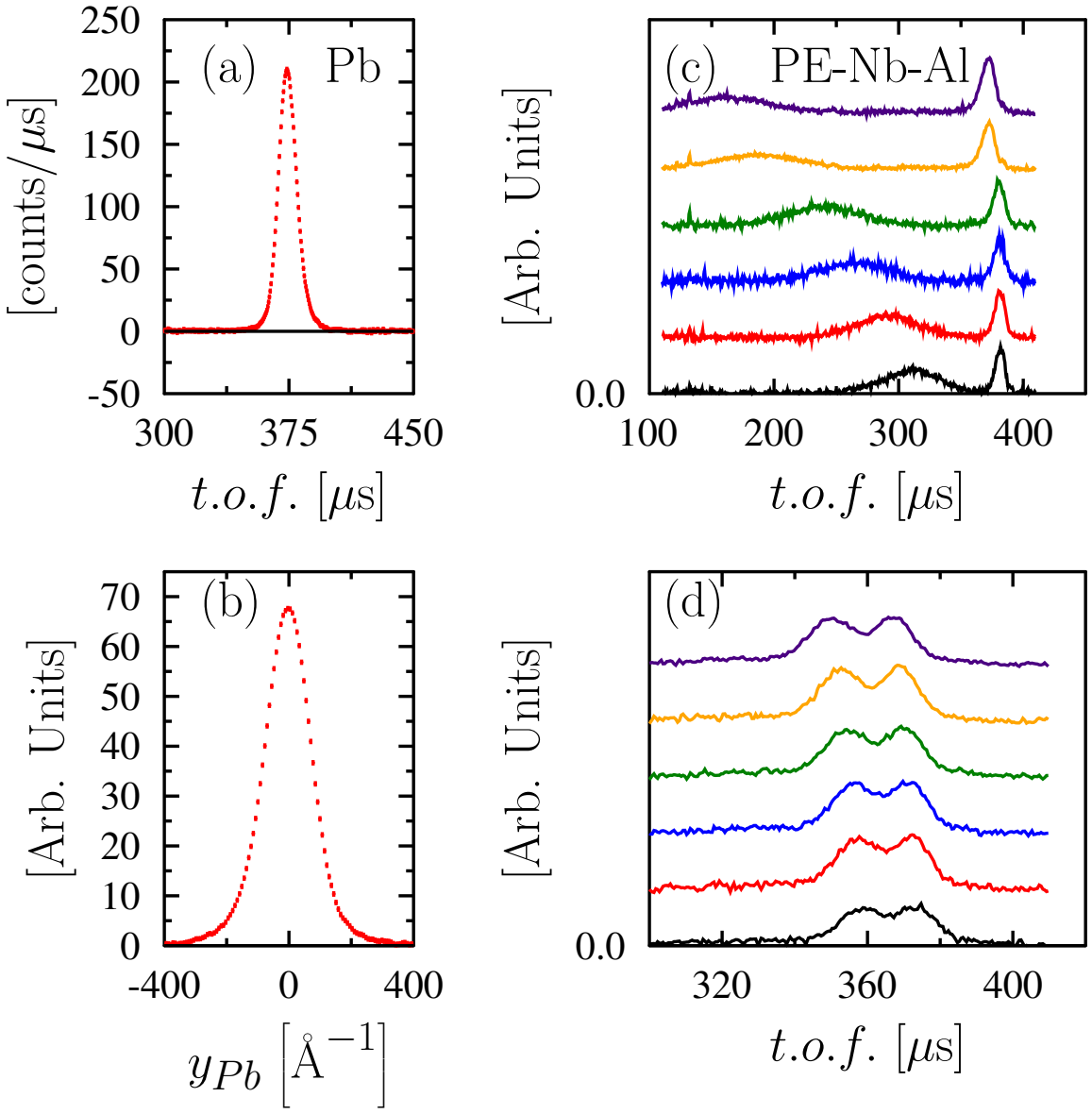

Figure 13. Representative recoil data using eV neutrons. Left: a 2-mm Pb standard at 300 K represented in either TOF (a) or y space (b). Right: a mixture of polythene, Al, and Nb, to illustrate the intrinsic mass-selectivity of these measurements. (c) and (d) correspond to forward and backscattering geometries, respectively. To ease visualisation, individual datasets for a particular scattering angle are shown with different colours and have been offset by arbitrary constants along the ordinate axis. As expected on kinematic grounds, the broad feature in forward scattering corresponds to H. Also note that in backscattering, the response from the heavier masses can be separated more readily than in forward scattering.

These include neutron diffraction, resonant capture, as well transmission data over several orders of magnitude in incident neutron energy. This versatility is a fortunate consequence of the unavoidable need with current detector technologies to implement foil-cycling techniques in order to effect energy analysis with eV neutrons. When the foils are absent, VESUVIO is for all practical purposes a neutron diffractometer. This feature has been exploited rather sporadically in the past [126–128], and its usefulness in the study of complex materials is further demonstrated in Section 3.2. Moreover, the use

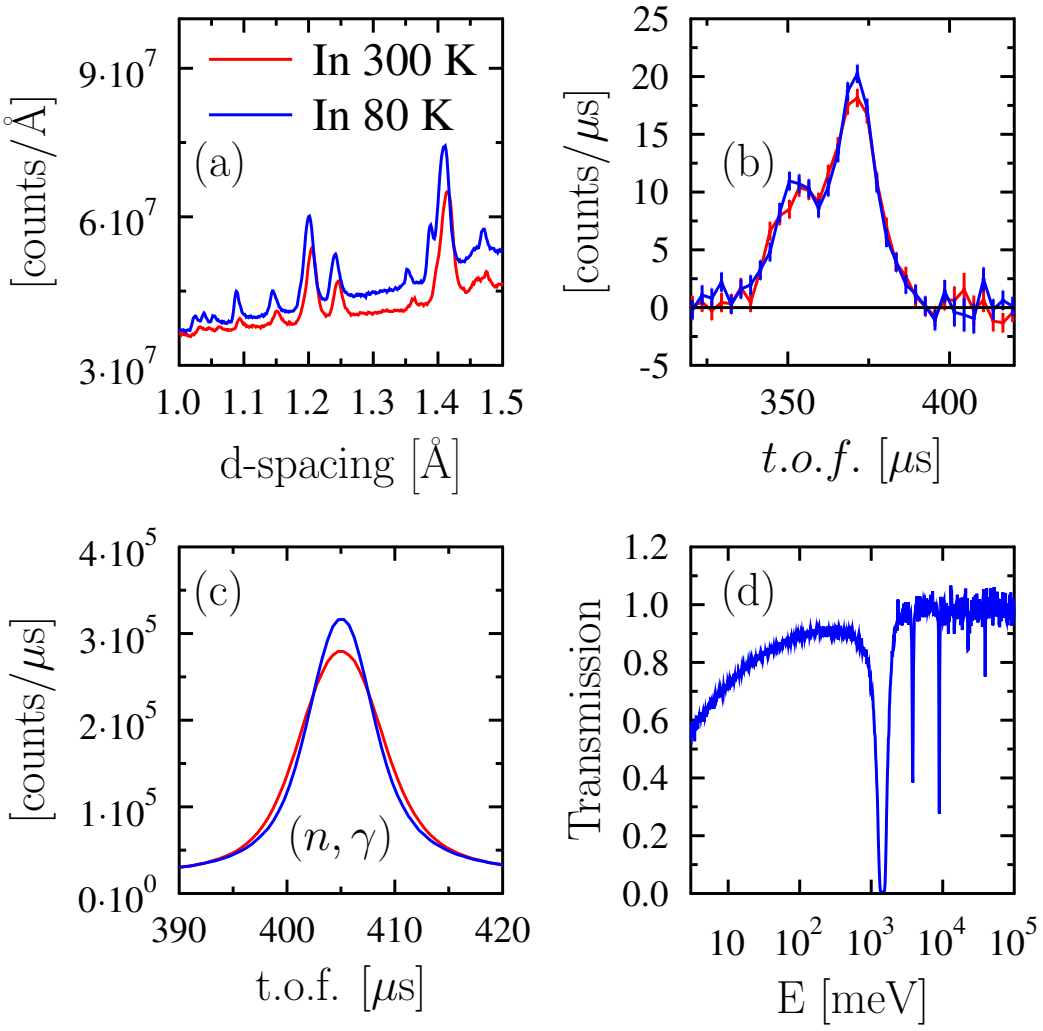

Figure 14. Simultaneous neutron measurements on a 0.25-mm Indium foil. Blue(red) data corrrespond to 80(300) K, respectively. Left: neutron diffraction (a) and resonant (n,γ) neutron capture (c). The diffraction data have been obtained from the cumulative sum of all backscattering detectors, and have been shifted by an arbitrary constant along the ordinate axis in order to facilitate comparison. Right: the top panel shows recoil data in TOF (b), including the contributions from Al (sample environment) and In. Panel (d) corresponds to transmission data, noting the logarithmic scale for the abscissa. The strong dips above 1 eV in these data arise from resonant scattering.

of γ-sensitive detectors also allows for the detection of reaction products from resonant neutron capture. In the simplest of cases, these data have already been used to quantify in a non-destructive manner the elemental composition [129] and effective temperature of a respectable number of (typically heavy) elements in materials [130]. These features are illustrated in Fig. 14, where the line shape of a neutron-capture resonance from Indium exhibits a marked temperature dependence. These changes are ultimately related to the underlying NMD, and new methods to perform this analysis in a quantitative manner are the subject of intense research and development efforts at the present time.

The usual approach to analyse experimental recoil data is to account for the Doppler broadening of a recoil peak by relating it to the underlying NMD of the target nucleus. In practice, DINS data analysis requires a quantitative comparison of NMDs obtained from data at different scattering angles. $n(p)$ is eventually calculated using one of the models

introduced in Sections 2.1 and 2.2 and model parameters are optimised using data-fitting protocols. FSE corrections at finite Q (*cf.* Section 2.1.2) are routinely incorporated into the data treatment using the expression detailed in Eq. (18) as well as the instrumental resolution function, $R_M(t)$, which for each M is described by a y- and Q-dependent line shape for each detector l, *i.e.,* $R_l(y,Q)$ introduced in Eq. (20) [124]. It is important to note that the physically relevant variables y and Q are to be regarded as explicit functions of all instrument parameters t, L_0, L_1, ϕ, and E_1. As such, they can be calculated for each TOF channel at a given detector l. The instrument resolution also varies across detectors and is determined through calibration procedures whereby y for a given mass M is also an explicit function of instrument parameters, that is, $y = y(t, L_0, L_1, \phi, E_1)$. The contribution of a given parameter p to the resolution can be then obtained from the relation [124]

$$\Delta y_p = \frac{\partial y}{\partial p}\Delta p \tag{65}$$

where Δp denotes the measured uncertainty in p. Figure 15 shows values for these different components and for different nuclei in momentum space. In this treatment, these are assumed to be Gaussian except for the energy resolution function which is a Voigt profile, *i.e.,* the convolution of Lorentzian and Gaussian line shapes. For all masses, the two dominant components to the resolution are those associated with the scattering angle and neutron energy. For the case of the proton, the angular resolution component dominates and for masses up to around 20 amu, the overall resolution is about one-fourth of intrinsic peak widths [124]. Further improvements of the resolution for moderate-mass and heavier nuclides can be achieved in a number of ways. These include using YAP detectors in backscattering geometry and the use of U foils rather than Au to effect final-energy analysis [124]. Another possibility that has been recently considered would be to increase the incident flight path L_0 from the current 11 m to over 20 m [125]. As many of the separate resolution components depend on the ratio of primary to secondary paths L_0/L_1, this change alone would result in an overall improvement of the resolution for all nuclei, both light and heavy. In addition to the works cited above, Ref. [22] provides a more detailed account of the formalism used to calculate the instrumental resolution in indirect-geometry spectrometers, with special emphasis on its application to spectroscopy with epithermal neutrons.

In order to derive the NMD for a particular mass, it is necessary to subtract all unwanted contributions to the experimental TOF data. Such contributions include multiple scattering, the scattering response from species other than the mass of interest, and γ-backgrounds. Multiple scattering is calculated for each scattering angle using a Monte-Carlo procedure described in Ref. [123] and then subtracted from the data. The unwanted scattering contributions from other atoms in the sample are subtracted by fitting the data and subtracting the fits to masses other than that of interest. For hydrogenous samples where the proton peak is well separated from those of other atoms, cross-correlations between fitting parameters for different masses are small and this procedure is very efficient. Once all unwanted components have been removed, the data consist of a series of TOF spectra containing only the recoil peaks of the masses of interest. These spectra are simultaneously fitted to Eq. (63) convolved with the appropriate instrument resolution function. Since the resolution function on VESUVIO varies significantly with scattering angle, each DINS spectrum needs to be fitted following this procedure. In an

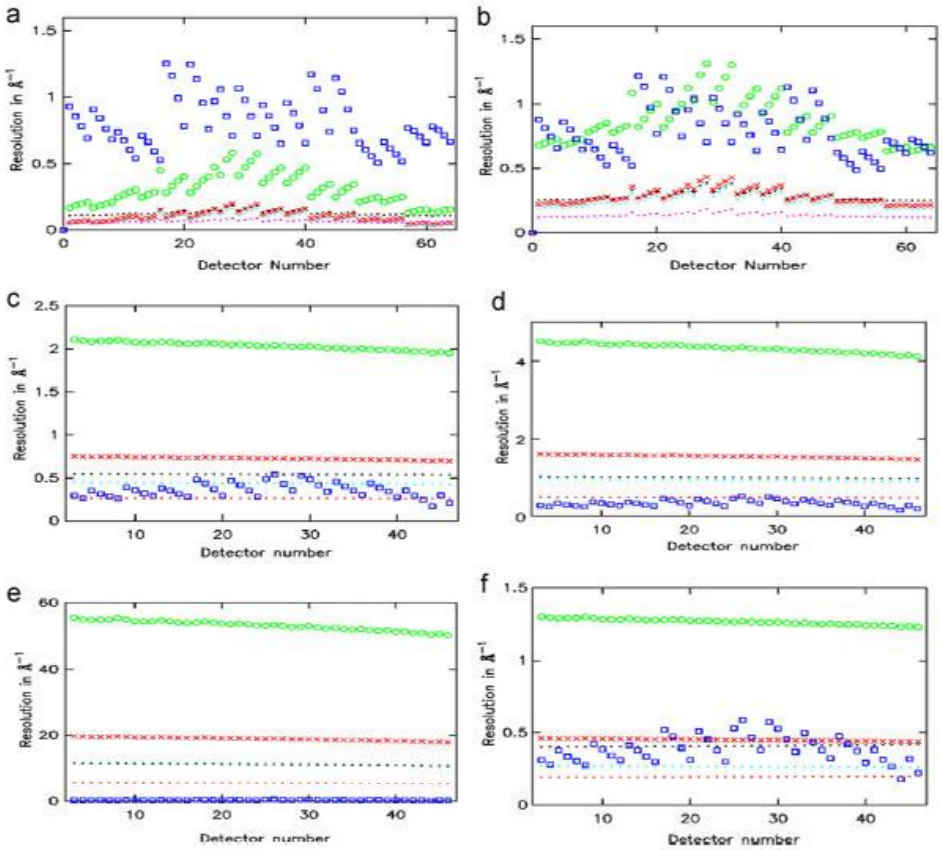

Figure 15. Resolution components in momentum space on VESUVIO for H (a) and D (b) in forward-scattering geometry using YAP detectors. (c)-(f) correspond to the resolution in backscattering using DD: Li; O; Pb; and ^{4}He. Colours and symbols indicate different components to the overall resolution function: angular (blue rectangles); Gaussian energy component (green open circles); Lorentzian energy component (red crosses); uncertainty in L_0 (black filled circles); uncertainty in L_1 (pink filled circles); time uncertainties (light blue filled dots). Typical NMD widths are 3-5, 5-6, 7-8, 10-15, 30-40, and 1 Å^{-1} for H, D, Li, O, Pb, and liquid ^{4}He, respectively. Reproduced with permission from Ref. [124].

isotropic sample, there are typically a total of 64 spectra fitted simultaneously, whereas with a single-crystal sample as many as 300 spectra comprising several crystal orientations relative to the incident beam may be fitted simultaneously [55]. Then, $n(p)$ can be reconstructed as described in Section 2.1.2. Reference [131] describes recent software developments aimed at providing a unified framework for the analysis of DINS data. These include the use of Bayesian inference methods to effect model selection [132], a tool of increasing importance and relevance to assess the information content of oftentimes sparse data sets, particularly those exhibiting intrinsic mass selectivity in TOF – *cf.* Section 2.3.3 and Ref. [133]. Its first use in the analysis of experimental DINS data enabled the determination of the maximum number of statistically significant coefficients in the Hermite polynomial expansion of the NMD [31]. More recent work has examined general model-selection protocols taking as starting point a set of possible NMD 'priors' [134]. Further details of DINS data analysis can also be found in Refs. [1, 31].

2.3.3. Mass-selective neutron spectroscopy

Beyond the study of individual nuclides in a condensed-matter or molecular system, the recoil data shown in Fig. 2 has already illustrated that neutron scattering using incident

energies in the eV range may also be regarded as a mass-selective spectroscopic technique where each atomic mass in the material contributes to the overall TOF spectrum in the form of a Doppler-broadened recoil peak [1]. The use of epithermal neutrons with energies up to hundreds of eV (orders of magnitude above phonon frequencies in condensed matter) guarantees sufficiently high momentum transfers such that the width of recoil peaks in the energy domain can be related to the NMD of the target nucleus prior to the scattering event, *i.e.,* the celebrated IA discussed earlier. With sufficient spectral resolution (as that afforded by inverted-geometry neutron spectrometers like VESUVIO), the overall widths of these recoil lines become sensitive to the chemical binding environment of a particular atom. Such mass and chemical selectivity (particularly for light nuclides) places DINS in a unique position relative to other scattering techniques. As discussed in the previous sections, the primary application of DINS has focused on the study of NQEs associated with proton motions. Beyond the proton, recent instrument developments offer the exciting prospects of extending the realm of applicability of DINS techniques to MANSE studies of materials containing heavier nuclides including D, Li, B, C, O, F, *etc.* In this context, it is worth recalling pioneering work on molecular and metallic glasses [98, 99] as an early illustration of the use of DINS and computer simulation to explore the consequences of spatial disorder and glassy behaviour in the solid state. For the case of hydrogenated and deuterated methanol, it was found that the crystal had an excess mean kinetic energy of up to 5 meV relative to the glass. The origin of such a difference was attributed to the 'lattice' contribution to H/D NMD widths since internal molecular frequencies were not expected to exhibit strong variations in passing from glass to crystal, and the same was expected to apply to mean-square displacements. The contribution of inter and intramolecular modes to the VDOS for the low-temperature glass and the crystal were first taken from force-field-based classical molecular dynamics and phonon calculations carried out on ensembles of rigid molecular units. Such an energy distribution for the VDOS implied a complete separation between internal and external molecular modes, and was further validated via comparison with experimental DINS data. Based on the model proposed, it was found that the dominant contribution to calculated H NMD widths stemmed from intramolecular modes with only about 7-12% attributable to collective (lattice) motions. The authors also argued that the net result of anharmonicity in the glassy state translates into a *narrowing* of NMDs, an effect which arises from the use of a simple anharmonic (up to fourth-order) perturbation to the harmonic potential. Estimates of such effects indicated that rather large anharmonicities (above some 5% in terms of the ratio of quartic to quadratic force constants) were required in order to translate these into a measurable effect on NCPs using the instrumentation available at the time. Similar conclusions in terms of *lower* atomic mean kinetic energies in the glassy state relative to the thermodynamically stable crystal phases were subsequently reported for $Ni_{0.83}B_{0.17}$ alloys, further demonstrating that a number of microscopically anomalous features of metastable matter can be traced back to the very-short timescales amenable to investigation using DINS. These findings tell us that the fingerprints characteristic of glassy dynamics are not confined to low frequencies but, rather, they can extend over at least fourteen decades in frequency, from long-time relaxation processes all the way up to atomic motions. The effects of topological disorder brought forward via glassification are then translated into a measurable modification of atomic NMDs. Even if the measured effects are relatively weak, the analysis in terms of molecular and lattice contributions to the total kinetic energy provided a solid framework for an understanding of the experimental DINS data.

Since these initial (and quite remarkable) investigations in the early days, an increasing number of MANSE studies have been reported recently including bulk and nanoencap-

sulated NaH [101], ^{7}LiF [135], and LiH and its deuterated counterpart LiD [78, 136]. In spite of the relatively low neutron-scattering cross sections of elements like Li, these studies have demonstrated sufficient sensitivity to the underlying NMD for this technologically relevant nuclide via a judicious choice of experimental conditions. In what follows, we summarise current developments in this emerging area of application of the DINS technique by revisiting in some detail the case of LiH and LiD, covered earlier in Section 2.2.2 when discussing the calculation of DINS observables for crystalline materials. For more details on recent developments of the MANSE technique, the reader is referred to Refs. [136, 137].

MANSE data for LiH and LiD measured on the VESUVIO spectrometer are shown in Figs. 16-17. These data are shown as TOF spectra in both forward and back-scattering geometries, in order to highlight that the (nearly) isobaric nature of the neutron relative to the proton dictates that the latter can only scatter in the forward direction, provided that the observed signal originates from single-scattering events. Use of TOF data directly for data analysis necessarily implies that the underlying NMDs (most naturally expressed in y-space) are 'forward-convolved' to simulate experimental data.

We recall that for a total of N different masses present in the sample, the total count rate $C_\phi(t)$ at a fixed scattering angle ϕ is given by Eq. (63)

$$C_\phi(t) = A'[\frac{E_0 I(E_0)}{Q}]_t \times \sum_{M=1}^{N} I_M M_M J_M[y_M(t)] \otimes R_M[y_M(t)] \quad (66)$$

where A' is an constant and the mass–independent factor $[\frac{E_0 I(E_0)}{Q}]_t$ is a function of the incident neutron spectrum $I[E_0(t)]$, the initial neutron energy $E_0(t)$, and $Q(t)$, all parametrically dependent on the TOF t. In Eq. (66), $J_M[y_M(t)]$ for a given mass M conforms to a suitable model for the NMD as discussed in Sections 2.1 and 2.2. Integrated peak intensities I_M are proportional to the scattering power for a given mass $I_M = AN_M\sigma_M$, where $\sigma_M = 4\pi b_M^2$ is the total (bound) neutron-scattering cross section [2, 84]. Equation (66) encapsulates the merits and strengths of MANSE. First, MANSE data provides a simple head count of different elements in the sample, an observable that might not be a trivial one to measure (*i.e.*, think of minute concentrations of H or Li in a heavy-metal matrix). Current limits of detection of H on VESUVIO, for example, are estimated to be in the μmol/cm^2 range. Second, the line shape associated with the DINS response of each individual mass is directly related to the underlying NMD (*i.e.*, its second-order moment, which in turn is related to the average kinetic energy $\langle E_K \rangle$).

The solid lines in Figs. 16-17 correspond to the best fits to the experimental data using Eq. (66) over the entire angular range in forward and backscattering. These experimental data, therefore, correspond to the cumulative sum of unit-area-normalised TOF data on a detector-by-detector basis across the entire angular range available on the instrument, a procedure that leads to an order-of-magnitude increase in detected flux with little loss in information content – *i.e.,* it is still possible to extract reliable information associated with the NMD for each individual nuclide. In this particular case, the underlying NMDs assume Gaussian behaviour as well as FSEs compliant with a 3D–HO model, in line with previous experimental and first-principles studies [78]. The agreement between experimental data and associated fits of unit-normalised sums for LiH and LiD TOF spectra is very good both in forward and backscattering, as well as bring to the fore a number

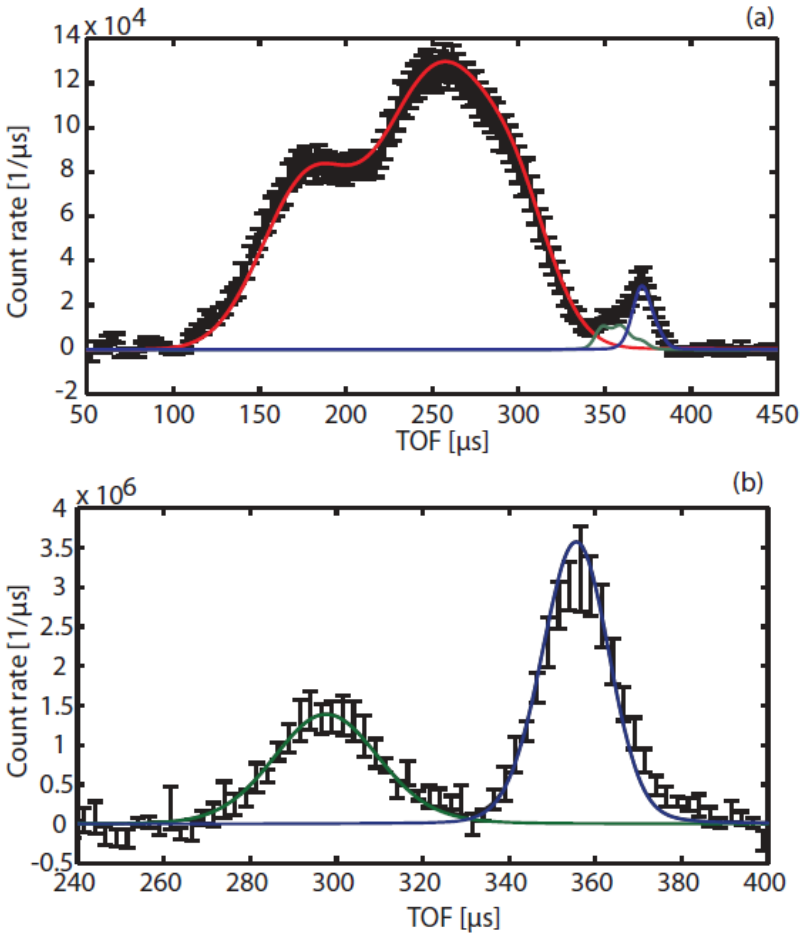

Figure 16. Sum of unit-area-normalised LiH TOF spectra (black symbols) in forward (a) and backscattering (b) compared with the sum of unit-area-normalized individual fits (black line). Individual mass contributions are shown by the solid lines. See the main text for further details.

of features in these data worthwhile commenting upon in some depth. These summed TOF data contain broad distributions from H(D) in LiH(LiD). This feature arises from purely kinematic considerations defining the centre of recoil profiles, with H and D peaks appearing over a broad range of TOFs at different scattering angles ϕ. In backscattering (*cf.* Figs. 16b and 17b), such a dependence of recoil-peak TOF positions as a function of ϕ is far less pronounced. This situation clearly offers the possibility of clean isolation of detector-summed DINS data arising from individual recoil peaks for M $>$ 1 amu,

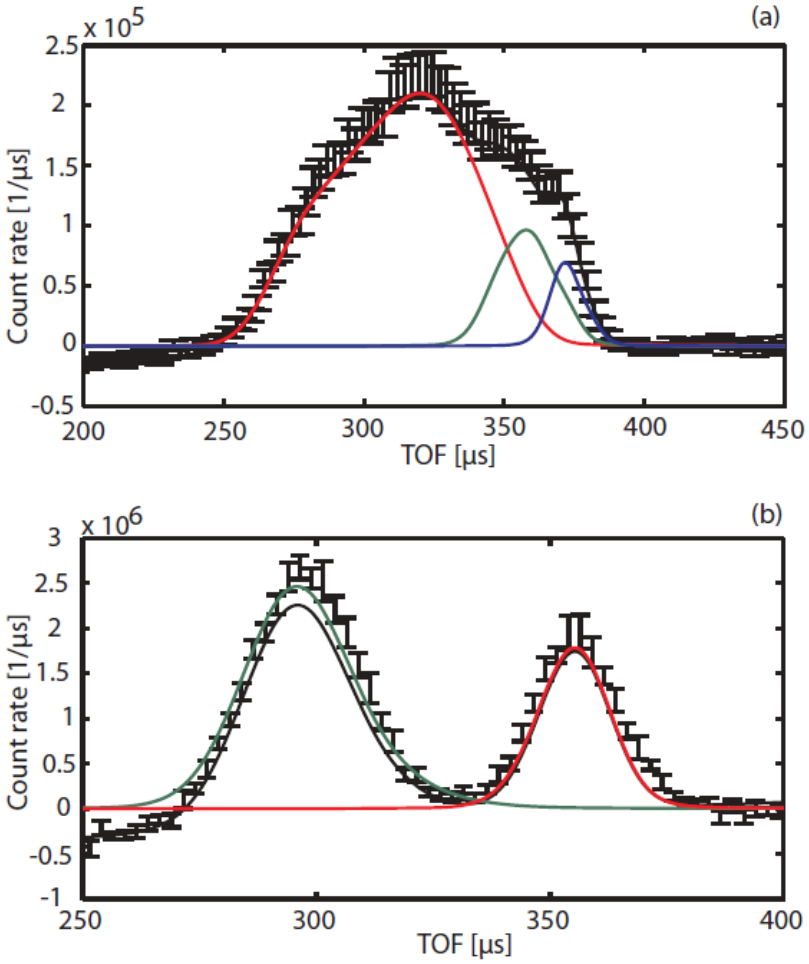

Figure 17. Sum of unit-area-normalised LiD TOF spectra (black symbols) in forward (a) and backscattering (b) compared with the sum of unit-area-normalized individual fits (black line). Individual mass contributions are shown by the solid lines.

In addition, these results show that a similar strategy is also possible in forward scattering, as the sums of unit-normalised TOF data are resolved well enough to be unique functions of the underlying individual NMDs. This feature is further demonstrated in Figs. 16a and 17a showing the presence of distinct shoulders and subsidiary maxima in the H and D recoil spectra, as well as a reasonable degree of separation of Li and Al (sample container). It is also important to note that the insights brought forward by the analysis of these summed data are of direct relevance to the exciting prospects of signifi-

cant enhancements in effective count rates in future DINS studies of complex materials. With the present experimental setup on VESUVIO, these gains can be greater than two orders of magnitude, provided that the resulting DINS line shape is still sensitive to the spectral moments of the underlying NMD. Whereas the viability of this approach is quite clear for backscattering data, further work is required to assess its range of applicability in the forward-scattering direction. To this end, one possibility may involve increasing recoil-peak visibility by focusing specific sets of forward-scattering detectors to yield the best possible peak separation, *i.e.*, in the angular range between 55 and 65°. The other possibility would be the use of summed and normalised foil-in spectra. Here the gain would be twofold, firstly from a sheer signal-to-noise-ratio gain obtained by circumventing the need to perform foil-in/foil-out differencing and, secondly, from a significant reduction in data-acquisition times. These and other possibilities are discussed in more detail in Refs. [137, 138], including extension of the MANSE technique to the simultaneous study of hydrogen, carbon, and oxygen atoms in organic ferroelectrics.

3. Case studies in materials science

The previous sections have already presented a wide range of DINS studies performed over the past decade, with an emphasis on new classes of materials, as well as emerging experimental and computational methodologies to tackle these. In the following, we extend this discussion to illustrate the use of DINS in specific areas of contemporary materials research. Possibilities associated with the use of DINS remain practically unlimited, and much remains to be explored. Having both the DINS expert and novice in mind, the primary aim of this section is, therefore, to stimulate further and exciting work in the foreseeable future.

We start with water, a molecule central to both chemistry and life, as well as the subject of intense DINS research over the past decade. The structure and dynamics of this ubiquitous molecule in the liquid phase are directly (and profoundly) influenced by quantum mechanics, not only in terms of its electronic structure and chemical bonding, but also at the level of nuclear motions. NQEs include ZPEs, tunnelling across HBs, anomalous ionic conductivity, intriguing isotope effects in its thermodynamic properties, and large deviations from classical (Maxwell-Boltzmann) behaviour for both the average nuclear kinetic energy $\langle E_K \rangle$ of individual nuclei and their associated NMDs. As one would naïvely anticipate on qualitative grounds, these effects are most prominent for the proton, owing to its light mass. Recent DINS work has also established that NQEs can also be of key importance to explain the dynamics of the heavier O atom. As stressed earlier in this work, DINS observables provide unique information on the underlying potential energy surface that individual nuclei see as the local environment evolves, as, for instance, in the presence of proton tunnelling, delocalisation, and bond breaking. Changes to the properties of water as a result of extreme (nanoscale) confinement in porous materials or by direct interaction with the surface of biomolecules are also discussed in detail, with implications to charge and molecular transport of relevance to proton- and ion-conduction mechanisms in a growing number of situation of practical interest. The second case study presented in this section deals with the behaviour of H_2 adsorbed in nanostructured materials. In this case, we focus on the specific scientific questions that DINS can address in the study of energy materials, so as to illustrate to the unfamiliar readership how the technique can provide unique insights not amenable to investigation by other experimental probes, including the spatial orientation of the H_2 adsorbate or the characteristic energy scales associated with adsorbate-adsorbate interactions.

3.1. *Water, from the bulk to the nanoscale*

Water is an essential component on Earth, exhibiting a number of unique and anomalous physical and chemical properties in both bulk states and under confinement. The structural and dynamical properties of water play a central role in many phenomena of relevance to fundamental and applied science. These can be attributed to the ability of the water molecules to establish a dense but still very dynamic 3D HB network, in which both the number and the strength of HBs continuously fluctuate. As a result, NQEs in aqueous media can be very significant even at ambient conditions, and are known to affect in a fundamental way charge-transfer mechanisms underpinning acid-base chemistry. For example, the pH of liquid water exhibits strong changes upon isotopic substitution: it goes from 7.0 to 7.4 upon deuteration, and to 7.6 upon tritiation. Extrapolation of this trend to the classical limit of nuclear motions (*i.e.,* infinite mass), the pH of water would be 8.5, that is, a thirty-fold change in the equilibrium acid-dissociation constant [103]. Moreover, the water molecule is also known to control reactivity in biological media, as evidenced by dramatic effects on molecular and biomolecular stability upon H/D substitution [139, 140]. The HB network in water displays remarkable flexibility at room temperature, a consequence of its peculiar dynamics, while a decrease in temperature from liquid water to ice results in a much-stiffer HB network. The end result is that ice displays far fewer exceptional properties than liquid water and is no longer a life-supporting medium. The origin of this flexibility in liquid water can be traced back to large librational excursions that H_2O molecules can perform without breaking the HB network, a possibility that classical methods to describe ordinary liquids have great difficulties taking into account. Interest in a thorough understanding of this extended HB network at molecular and mesoscopic scales is continuously growing and experimental and theoretical studies of aqueous media constitute one of the main fields of interest in physics and chemistry. Historically, the description of these dynamic properties can be traced back to infrared and Raman studies of vibrational spectra, followed by more recent neutron investigations. This evolution has led to an assessment of subtle effects associated with anharmonicity and NQEs, concepts which naturally emerge when interpreting the exceptional spectroscopic properties of HBs, in an attempt to understand which bonding motifs constitute the primary path through which protons can be transferred across molecules at the mesoscale.

This section presents an overview of most significative results of microscopic single-particle dynamical properties of water investigated by DINS over the past decade. These studies were made possible by the development of the new techniques and experimental strategies described in Section 2.3.1. The technique has been extensively applied to refine the study of the single-particle dynamics of light nuclei such as H and D, as well as to extend these heavier nuclei such as O and beyond [35].

As far as water is concerned, DINS is currently a quantitative and well-established technique capable to get fresh insights into the intermolecular HB interactions at the heart of the peculiar properties of water, in many respects complementary to INS and optical spectroscopy [62, 141]. The most significant results of these investigations are reviewed in the following sections. These discuss DINS measurements of water around the triple point, water at room temperature, in the supercooled state and ice, as well as water in the supercritical state, confined in nanopores, and finally in proteins and DNA. The selected examples emphasize the experimental progress beyond the measurements of fundamental observables such as $\langle E_K \rangle$ and $n(p)$, for example the ability of DINS to look at directional components of the mean kinetic energy tensor, $\langle E_K \rangle_{x,y,z}$, of light and heavy nuclei, and to highlight the existence of competing NQEs [142] in water.

Intermolecular interactions in bulk water typically represent small changes in the energy of the primary constituents compared to the energy sequestered in the proton ZPE, primarily that of the OH-stretch mode. To the extent that this energy does not change by external interactions, it may be ignored (and it usually is). It is worthwhile noting that nearly all simulations of water in biological systems continue to be performed with models of water which do not include these changes, or are not considered because of the additional expense in treating NQEs from the outset. Yet the most prominent demonstration of the quantum nature of H nuclei is that their NMDs do not follow a Maxwell-Boltzmann distribution. Thus, the PI methods introduced in Section 2.2.3 constitute the fundamental tool to examine how DINS observables such as $\langle E_K \rangle$ and $n(p)$ [59] are affected by NQEs. DINS investigations also demonstrate the capability to follow changes in $\langle E_K \rangle$ as the structure of the HB network changes, as a function of temperature and pressure, as well as of the state of aggregation and confinement. The latter can arise by a restriction in space (for example, molecular bonds) or be a purely topological constraint (nanoscale confinement). DINS measurements of $\langle E_K \rangle$ value and $n(p)$ line shapes uniquely fingerprint and track these changes. For example, spatial localisation gives rise to an increase in $\langle E_K \rangle$, whereas bond softening leads to a reduction in $\langle E_K \rangle$.

3.1.1. Water around the triple point

Recent INS studies of ice and water in stable and metastable states around the triple point show that the OH-stretch component of $\langle E_K \rangle_z$ has almost identical values when interpreted within a harmonic framework: 98 meV, 100 meV and 100 meV for ice at 271 K, supercooled water at 271 K, and liquid water at 300 K, respectively [141]. This is an indication that NQEs associated with the OH stretching frequency, ω_z, are weakly temperature-dependent in the explored temperature range. This work has also shown that DINS measurements allow to go beyond the harmonic framework and can provide full directional components of the mean kinetic energy tensor [143].

A recent DINS study in the metastable phase of water (and ice) at T=271 K (*i.e.,* near the triple point), and liquid water at 300 K, provide accurate measurements of the proton $n(p)$ and its associated directional mean kinetic energy components $\langle E_K \rangle_\alpha$, where $\alpha = x, y, z$ [144]. The measurement on ice was specifically recorded at the same temperature as on supercooled water, in order to allow a quantitative benchmark with previous DINS experiments performed at the same thermodynamic point [59]. Values for σ_α from this experiment are reported in Table 7. These highlight a main distinctive feature between supercooled water and ice at $T = 271$ K: the anisotropy of the proton NMD is slightly more pronounced in the supercooled liquid than in the solid phase. Similar features have also been obtained in a combined INS-DINS investigation of water at T=285 K and ice at T=271 K [62]. Values of the proton total mean kinetic energy, $\langle E_K \rangle = 3\frac{\hbar^2\sigma^2}{2m}$, and the directional components along the three axes, $\langle E_K \rangle_\alpha = \frac{\hbar^2\sigma_\alpha^2}{2m}$, are derived for ice, supercooled water, and water at room temperature, as well as compared with values obtained from INS [141] and theory [145]. In this case, $\langle E_K \rangle$ for ice at T=271 K together with the σ_α values are the same, within experimental uncertainties, to those obtained in previous measurements at the same temperature [59]. This represents a reference benchmark which validates and strengthens the total value of $\langle E_K \rangle$ =156 meV, and its directional σ_α components obtained for supercooled water. The DINS technique fingerprints the competition between intra and intermolecular NQEs during the transition from a disordered phase (supercooled water) to a polycrystalline one (ice): the competition between the directional energy components $\langle E_K \rangle_\alpha$ is such so as to produce

Table 7. $\langle E_K \rangle$ and individual $\langle E_K \rangle_\alpha$ values in bulk supercooled water (SW) and ice at $T = 271$ K. For each sample, a simultaneous fit of experimental $F_l(y, Q)$s is accomplished using two parametric models for $n(p)$: (a) a model-independent line shape, hereafter Model 1 [M1, *cf.* Eq. (21)]; and (b) a 3D anisotropic Gaussian line shape derived from a quasi-harmonic model, hereafter Model 2 [M2, *cf.* Eq. (23)]. These are obtained using M2, while M1 gives $\langle E_K \rangle$, c_4 and σ. The latter is found to be equal to $\bar{\sigma} = \sqrt{\sum \sigma_\alpha^2/3}$ where values for σ_α are taken from M2 [144].

		SW	Ice	Ice[59]
T	[K]	271	271	271
M1				
σ	[Å^{-1}]	5.01±0.02	5.03±0.03	5.01±0.03
c_4		0.11±0.01	0.11±0.02	0.10±0.01
$\langle E_K \rangle$	[meV]	156.0±2.0	157.0±2.0	156.0±2.0
M2				
σ_x	[Å^{-1}]	2.9±0.5	3.7±0.1	3.7±0.3
σ_y	[Å^{-1}]	5.0±0.5	4.3±0.3	4.3±0.4
σ_z	[Å^{-1}]	6.5±0.2	6.6±0.2	6.5±0.4
$\langle E_K \rangle_x$	[meV]	17±5	28±2	29±4
$\langle E_K \rangle_y$	[meV]	52±10	38±5	38±9
$\langle E_K \rangle_z$	[meV]	86±5	91±5	87±9
$\langle E_K \rangle$	[meV]	156.0±2.0	157.0±2.0	154.0±2.0

a subtle cancellation effect, resulting in very similar values for $\langle E_K \rangle$ [146].

3.1.2. Water above melting: the supercritical state

Supercritical water is of fundamental and technological interest for applications as varied as producing hydrogen from glucose [147], the fabrication of YAG nanoparticles [148], or supercritical water-cooled reactors, promising candidates belonging to so-called Generation-IV nuclear-reactor technologies [149]. As for all supercritical fluids, small changes in pressure or temperature in water result in large variations in solubility. This allows the production of fine particles via precipitation of a solute from supercritical solution by rapidly exceeding the saturation point of the solute by dilution, antisolvent, depressurisation, or attemperation [150]. In addition to the above properties of supercritical fluids, supercritical water (SCW) exhibits peculiar properties due to the presence of intermolecular HBs. In SCW, more than 70% of HBs are destroyed to a nonpolar dimer, and further decomposed to monomer, H^+ and OH^- ions. Thus, SCW becomes a weakly polar solvent that can dissolve non-polar organics to produce fine particles via precipitation. On the other hand, high concentrations of H^+ and OH^- ions provide both basic and acidic reaction conditions for the synthesis of fine particles. Beyond its technological interest, the variation of the properties of water as it is heated under pressure to reach the supercritical point and above provides a means of investigating the effects of the HB network on those properties as this network is pulled apart.

The dynamics of protons in SCW have been fully characterized by DINS measurements performed from room temperature and pressure to above the supercritical point [151]. From this study the shape of the proton NMD in water has been derived and compared with theoretical calculations based on a polarizable water model [152]. The line shape of $n(p)$ in SCW was obtained using Eq. (23), taking Gaussian NMDs to describe motions both in and out of the molecular plane, and the assumption that the H dynamics along two orthogonal directions in the plane of the molecule were equivalent. The results show a transverse-momentum width slightly more than one half of the intrinsic width along

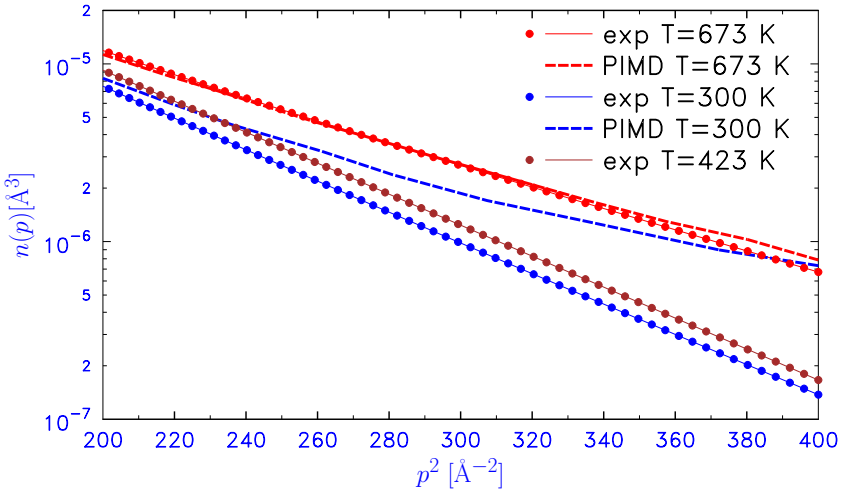

Figure 18. Proton NMDs in the region where they are dominated by motions along the O–H stretch direction: T = 673 K (red circles), T = 423 K (brown circles), and T = 300 K (blue circles). The calculated PIMD distribution at 673 K (red dashed line) is in very good agreement with the measured results and is nearly identical to that of the free monomer. The calculated result at 300 K (blue dashed line) gives too large a momentum width to describe the experimental data [151].

the OH-stretch direction. The $n(p)$ line shape along the HB direction is narrower in the dense phases and approaches that of the isolated molecule in the more dilute phases. The tail of the NMD arises from the momentum along the bond direction. The orientationally averaged NMD (which is what one measures for an isotropic fluid) is determined almost entirely by motions along the stretch direction at high momentum transfers (*cf.* Fig. 18 and discussion below). Since the proton is most tightly bound along this direction, and tight binding implies wide momentum widths, it is clear that this width has increased, which can be interpreted as arising from a slight increase in the average HB distance in water, so that the proton becomes more tightly bound to its covalently bonded O atom. The change in line shape reflects changes in HB and is easily observable, the difference being significantly beyond experimental uncertainties. Changes in covalent-bond lengths are only 4% [156], and the DINS measurements are clearly accurate enough to see the dynamical consequences of this shift. The calculated NMD at 673 K is in very good agreement with the DINS results and is nearly identical to that of the free monomer. The theoretical model, which includes only electrostatic interactions, is unable to explain the softening of the local potential experienced by the H nuclei in the dense phases, although it accurately predicts the NMD for the dilute phases, suggesting that covalency with the H-bonded O plays a significant role in determining the potential-energy landscape of the H nuclei. Evident structural changes in going from ambient to high-temperature conditions approaching the supercritical state are also readily discernible in Fig. 19 [151]. These data correspond to $\langle E_K \rangle$ for H in water as a function of temperature, obtained from DINS experiments.

Notwithstanding the above, a complete picture of water is far from being clear, as the interpretation of structural data is often carried out in terms of water as a collection of monomers interacting electrostatically. Recent theoretical work has compared the NMDs of aqueous protons obtained from DINS [151] with those calculated from two electronic-structure-based models. It was found that below 500 K, these electrostatic models, one based on a multipole expansion including monomer polarizability, are not able to even

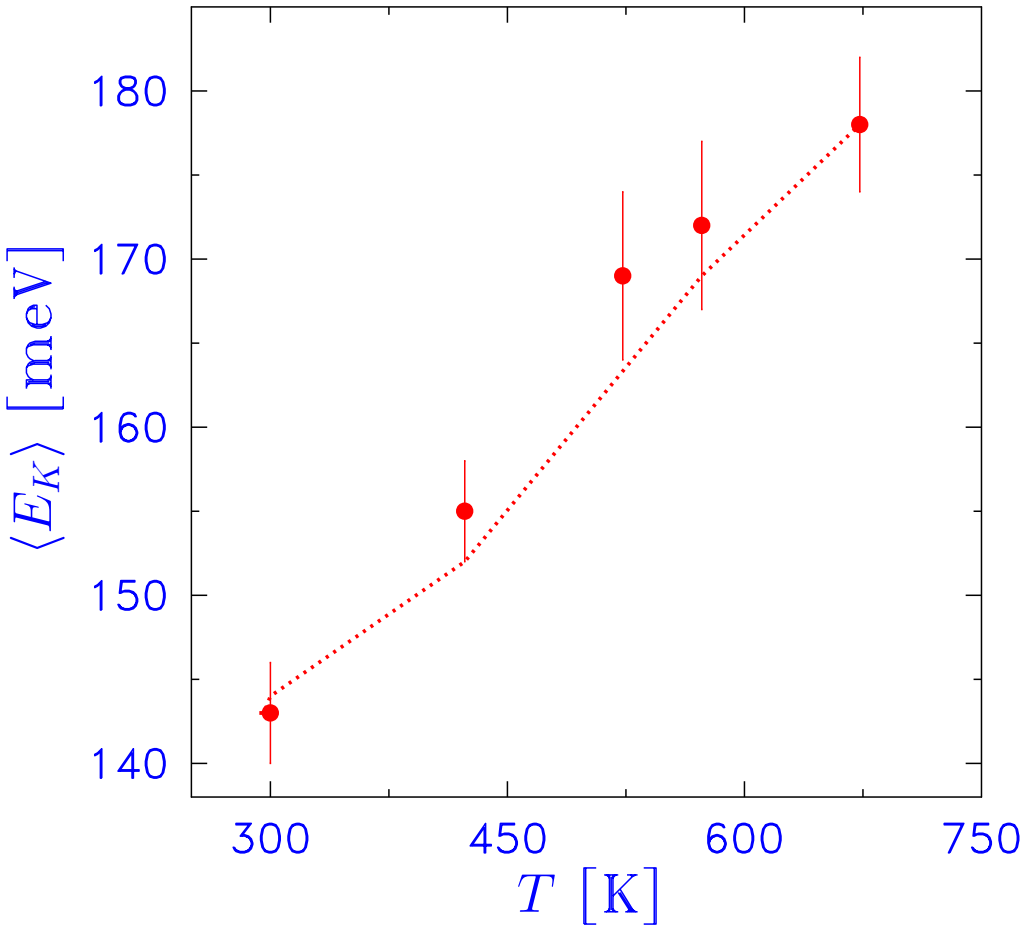

Figure 19. Temperature dependence of the proton $\langle E_K \rangle$ for the stable liquid and SCW (red circles with error bars, taken from Refs. [151, 153, 154]). The theoretical predictions from Moreh *et al.* [155] are shown as a red dotted line.

qualitatively account for a sizable ZPE contribution to the enthalpy of vaporisation [157]. This discrepancy provides strong evidence that the change in the proton NMD upon solvation cannot be entirely explained by electrostatic effects alone, but requires correlations of the electronic states on the molecules involved in HB to produce the observed softening of the potential energy landscape. At present, the vast majority of models and empirical potentials can account for the experimental structure factors of water [158, 159], yet they fail to reach the requisite accuracy to describe proton NMDs quantitatively. Indeed, a 10% change in the ground-state kinetic energy, which is very large on the scale of experimental uncertainties (less than 1%), amounts to a change in the width of the proton wavefunction by only 0.005 Å. This would make an indiscernible difference in the structure factors, where the scale length of the relevant features is about 1 Å. Given that the proton NMD is a function of the underlying potential energy surface, Burn-

ham *et al.* [157] have pointed out that that intermolecular perturbations of the proton potential-energy landscape in the bulk phases of water cannot be satisfactorily modeled using classical electrostatics alone. As evidenced by comparison with experiment, there appears to be an additional softening of the proton potential upon HB formation beyond that captured by electrostatic models.

3.1.3. Competing quantum effects in heavy water upon melting

Even though intrinsic NQEs can be very large (the ZPE of an O-H stretch mode, *i.e.,* $\frac{1}{2}\hbar\omega$, is in excess of 200 meV relative to classical predictions), it is often the case that their net effect on macroscopic properties can be relatively small. Sometimes, NQEs compete with each other and partially cancel each other out. This phenomenon is thought to play a role in determining the melting and boiling temperatures of water. For instance, the melting temperatures of light and heavy water differ by less than 4 K, and the boiling temperatures by just 1 K. From some recent theoretical work [142, 160], there are indications that these effects arise from a partial and rather subtle cancellation of NQEs in the intra and intermolecular components of the HB, so that the net effect is small even if the individual contributions are quite large. In particular, the competition between NQEs can be seen very clearly when decomposing changes in the quantum kinetic energy of protons and deuterons along different molecular axes [161, 162]. The mechanism that underlies the competition between changes in the different components of the quantum kinetic energy can be understood by considering a two-level quantum system with an environment-dependent off-diagonal coupling β. A small change in the coupling $\Delta\beta$ – arising from a phase transition or some other change in the environment of the system – will shift its eigenvalues by the same amount which is proportional to $\Delta\beta$, but in the opposite direction. Even though this picture is clearly oversimplified, it demonstrates that the notion of competing NQEs is not exotic, and explains why it returns in many circumstances in the study of water and other HB systems.

Competing NQEs, recently proposed in a variety of simulation work [142, 160–162], are likely to be at the root of the explanation as to why many of the properties of water depend only weakly on isotopic composition. Even at room temperature, quantum mechanics plays a major role in determining the quantitative behaviour of H and D nuclei in water, changing significantly the values of physical properties such as the heat capacity.

The first direct experimental observation of competing NQEs has been recently obtained via DINS measurements of the NMDs of D and O in heavy water and ice [36, 63] (*cf.* Fig. 20). DINS investigations supplemented by PIMD simulations provide the anisotropy of the quantum mean kinetic energy tensor $\langle E_K \rangle_\alpha$. Results show that two large components of NQEs partially cancel each other out resulting in a small net effect on the melting and boiling points of water [63]. The most interesting feature in $\langle E_K \rangle$ is observed upon freezing. A small change in the $\langle E_K \rangle$ during the melting process corresponds to the greatest changes of its internal components, namely the x and z components of $\langle E_K \rangle_\alpha$. These changes are in different directions, giving rise to a global cancellation: the increase of the x component is interpreted in terms of more hindered librations in the solid phase; a decrease along z is interpreted as a red shift of OH stretching due to an increase in HB, *i.e.,* the weakening of covalent OH bonds as seen in vibrational data.

NMD line shapes across the melting point of D_2O have very similar second moments, yielding kinetic energies of 108.3 ± 2.0 meV in the solid at T=274 K, and 111.3 ± 3.0 meV in the liquid at T=280 K, respectively. Nonetheless, the differences shown in their shapes reflect directly changes in the different components of the quantum kinetic energy

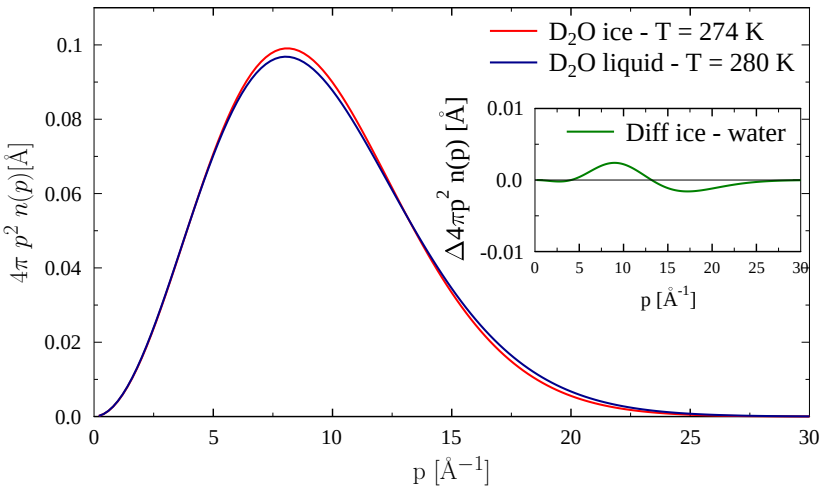

Figure 20. Radial $n(p)$ for D in solid heavy water at T = 274 K (red continuous line) and the liquid at T = 280 K (blue continuous line). The inset shows the raw difference.

in the two phases discussed above.

In conclusion, it is interesting to see how, despite the noticeable differences in the individual values of $\langle E_K \rangle_\alpha$, the theoretical and experimental n(p) line shapes for D are almost indistinguishable and how the computed n(p) depends only weakly on how the kinetic energy components are distributed, but in a more pronounced way on the total $\langle E_K \rangle$.

3.1.4. Confinement in nanopores

An understanding of adsorption processes in porous materials is of fundamental importance in processes such as gas storage and separation, chromatography, or catalysis. In this respect, neutron-scattering techniques provide direct information on the structure and dynamics of adsorbed molecules and, in particular, the role and influence of adsorbent microstructure (porosity, surface area) on these properties [2]. Experiment and theoretical calculations show that both the structure and diffusive motions of water are markedly perturbed when the pore size approaches the nanometer range (about 20 Å and below). In particular, results from experimental studies on confined water are sensitive to the nature of the confining environment [163]. First, we illustrate the use of DINS to study the adsorption of water in some model adsorbent systems, namely, xerogel, MCM-41, and carbon-based confining environments that can accommodate water or other organic molecular species. In these systems, water interactions with the adsorbent are of a predominantly hydrophilic or hydrophobic nature in the first two and last cases, respectively. The confinement lengths typical of these experiments are comparable to characteristic distances in biological media.

The bimodal NMD shown in Fig. 21 indicates that changes in the local structure around the proton are more evident for small pore sizes and that this effect ought to be related to the average potential. In this case, the bimodal distribution suggests that changes in the local structure around the proton occur, including distortions of the HB network. These results support mounting evidence that the protons exist in a characteristic quantum state when water is confined in tiny (nanoscopic) volumes. In this situation, the

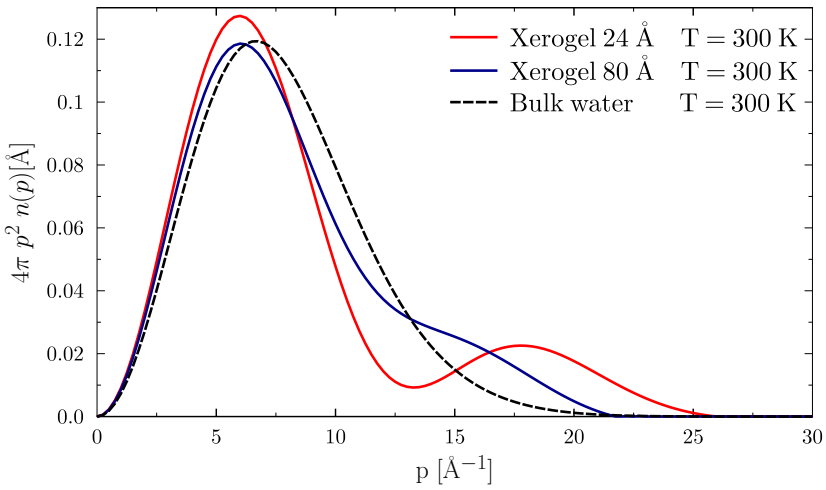

Figure 21. Radial NMD of the aqueous proton in xerogel samples at T = 300 K with different mean pore-size diameters: 24 Å (red continuous line), 80 Å (blue continuous line), and in bulk water at T= 300 K (black dashed line) [165].

intermolecular potential well exerts a significant force only over intermolecular distances around 10 Å, whereas quantum charge fluctuations take place across the HB network and become significant at the sub-Å scale typical of an individual-proton potential well [169]. In this picture, it is the response of the HB network to confinement that leads to unusually large changes in the mean kinetic energy observed in the DINS experiments. Since the characteristic length scales separating the building blocks across cells are of the order of tens of Å and such a distance is consistent with that characteristic of this quantum state of confined water, it might be surmised that these states may be playing a role in the development of cellular life.

Results from DINS experiments on MCM-41 at room temperature on dry and on hydrated samples highlight the interaction between the protons and the silanol groups on the confining surface. The level of hydration of the pores was controlled in order to adsorb an average of three water molecules per nm^2, corresponding to a 1:1 ratio of water-to-surface-silanol groups. A detailed analysis of the hydrated sample was performed in order to separate the contributions of the protons in the system, allowing to determine the arrangement of water molecules on the silanol groups. Information on the interaction between the substrate and the water absorbed on the pore walls was obtained from a DINS study of the water molecules adsorbed onto surface silanols [164]. In this particular experiment, there was only one molecule of water adsorbed per silanol group. Given the relatively long distance between two nearest silanols (about 5 Å), one could realistically consider each silanol group as isolated from one another. The two most favorable configurations that the water molecule can adopt are displayed in Fig. 22 [166, 167].

In each configuration, one HB and two non-interacting protons are present. From these configurations, it is possible to identify protons in different surroundings: non-interacting silanols (H_{dry}), non-HB water hydrogens (H_{mon}), water H bound to the silanol (H_w), and silanol H bound to the water oxygen (H_{sil}). In particular, in the two systems shown in Fig. 22 there are two configurations: (a) one H_{dry}, one H_w, and one H_{mon}; and (b) one H_{sil} and two H_{mon}. The response function of the hydrated sample $J(y)_{hyd}$ can then be expressed as the cumulative sum of the contribution from each H in the system,

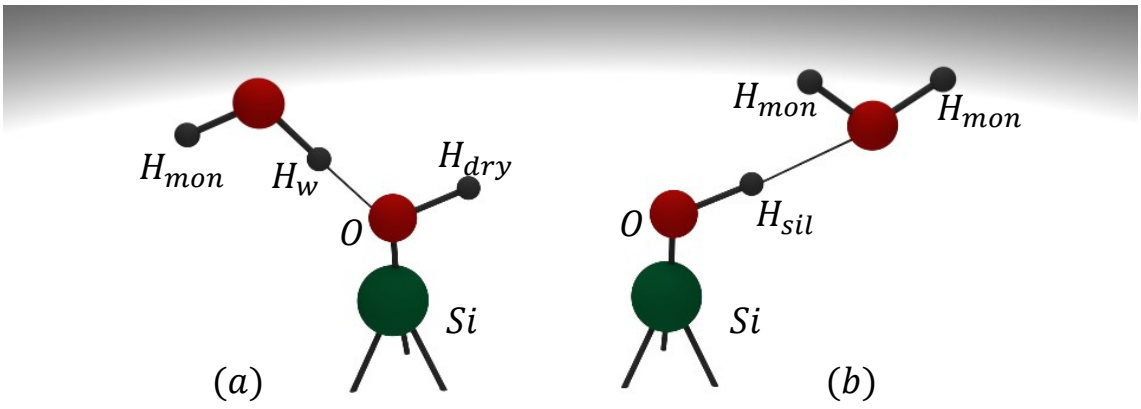

Figure 22. The two most favorable configurations of a single water molecule interacting with an isolated silanol group on the surface of an MCM-41 pore [164]. The meaning of the different labels shown in the figure are explained in the main text.

i.e., $J(y)_{dry}$, $J(y)_{mon}$, $J(y)_{sil}$, $J(y)_w$, using the above subscripts. Denoting by c the probability of finding the system in the (a) configuration of Fig. 22, this yields:

$$J(y)_{hyd} = 1/3[cJ(y)_{dry} + (1-c)J(y)_{sil} + cJ(y)_w] + \\ +1/3(2-c)J(y)_{mon} \quad (67)$$

where $J(y)_{dry}$ in the above equation has been obtained from the measurement of the dry sample. For $J(y)_{mon}$, the line shape used was the proton NCP derived in previous experiments on SCW at P=1060 bar and T=673 K [151], where it was shown that $n(p)$ had the same response as the free monomer. The fit of the hydrated response function was carried out by taking into account Eq. (67) with $J(y)_w$, $J(y)_{sil}$ and c as free variables. The result of the analysis is that both association states of the water, (a) and (b), exist with a slight preference for the former ($c = 0.61 \pm 0.14$). However, this configuration can experience two possible permutations due to the presence of two equivalent water H that can participate in HB. With this consideration in mind, it was concluded that the probability of HB formation involving either a silanol or a water H is comparable, with a slight preference for the latter. This result is in agreement with theoretical predictions showing that water-nanoporous-silica interactions can be described by assuming silanol as a model for the free-hydroxyl of amorphous silica [167].

The ability of DINS to measure proton NMDs in water directly and accurately has also been applied to a series of measurements of water in carbon nanotubes, showing that proton coherent delocalisation may be a generic feature of nanoscale confinement [168]. This effect leads to very different proton ZPEs highly sensitive to the confinement environment, 40(120) meV when water is in close proximity to single(double)-walled carbon nanotubes. The interpretation of earlier experiments was carried out in terms of a model of a single particle in an effective potential. The softening of the potential seen in the proton NMD for water confined in single-walled carbon nanotubes at temperatures below 268 K is consistent with an increase in the Debye-Waller factor observed previously [169, 170], but cannot be easily reconciled with the blue shift of the OH-stretch mode measured using INS [169]. For water in double-wall nanotubes, it has been hypothesized that the NMDs of the above experiments show evidence of correlated proton

motions resulting from the presence of an effective double-well potential. These changes, reported as a response to changes in the HB network, give rise to states of considerable anharmonicity, which can be expected to play a significant role in the energetics of biologically relevant macromolecules at the nanoscale. These considerations have been corroborated by subsequent work using X-ray Compton scattering in the fuel-cell material Nafion, an outstanding proton conductor. In this case, changes in the electronic environment of the proton were followed directly with this technique [171]. Furthermore, a more recent X-ray Compton scattering study has shown that the peculiar temperature dependence of water in carbon nanotubes as a function of confinement size can also be accounted for using a similar hypothesis, whereby the state of water cannot be simply described using a weakly interacting molecular picture [172]. All in all, these experimental results provide strong experimental evidence for the existence of a hitherto undetected state of nanoconfined water quite distinct from that of the bulk. In a wider context, the use of X-ray Compton scattering to confirm earlier DINS results certainly strengthens the integration of the latter in the spectrum of techniques available to study condensed matter.

Another example is a recent DINS experiment on water confined in 5 Å channels in the mineral beryl. The salient feature of this experiment is that the measured proton NMD reveals a coherent delocalisation of the protons in the ground state and extended proton delocalisation [173]. The data show that the $\langle E_K \rangle$ of H is 30% lower in beryl than in water in the liquid or solid state. The authors interpreted this lower energy as a consequence of the tunnelling which allows the proton to be at six possible crystallographic positions simultaneously and, thus, less confined. These experimental results are in excellent agreement with subsequent DFT calculations [174], evincing that the coupling of the water molecule to host lattice modes can give rise to proton states distinctly different from those found in ordinary water phases.

Most recently DINS measurements have also been performed on water and ice confined in hydrated and dried specimens of graphene-oxide (GO) membranes [175] and in 2D GO sponges [176] (see Fig. 23). The DINS study performed at room temperature on water confined in GO membranes [175] provided the first experimental determination of the mean kinetic energy of aqueous H adsorbed in GO membranes. The experiment was complemented by parallel X-ray diffraction, atomic force microscopy, and thermogravimetric analysis. Experimental results provide direct insight into the local chemical environment of the H nuclei under spatial confinement suggesting that the characteristic, quasi 2D confinement of water between GO sheets give rise to a binding environment remarkably similar to that found in the bulk. The authors surmise that this behaviour arises from a small fraction of hydroxyl groups relative to water molecules in graphene-oxide membranes, as well as the predominance of non-specific and weak interactions between water and the underlying nanostructured substrate [175].

The DINS study of water and 2D ice adsorbed in GO sponges, performed at T = 293 K and T = 20 K, probed the interaction of aqueous protons with the layered structure of the GO sponge [176]. It was shown that the H dynamics 2D-confined in the GO sponge is quantitatively different from that of water confined in other nanoporous hydrophilic surfaces, such as xerogel, MCM41 and nanotubes, and unlike any other form of water observed so far. The present results support a picture where the OH bonds of water and ice in GO are softer than in bulk water, *i.e.* the energy of the OH-stretch mode is also red-shifted and broadened.

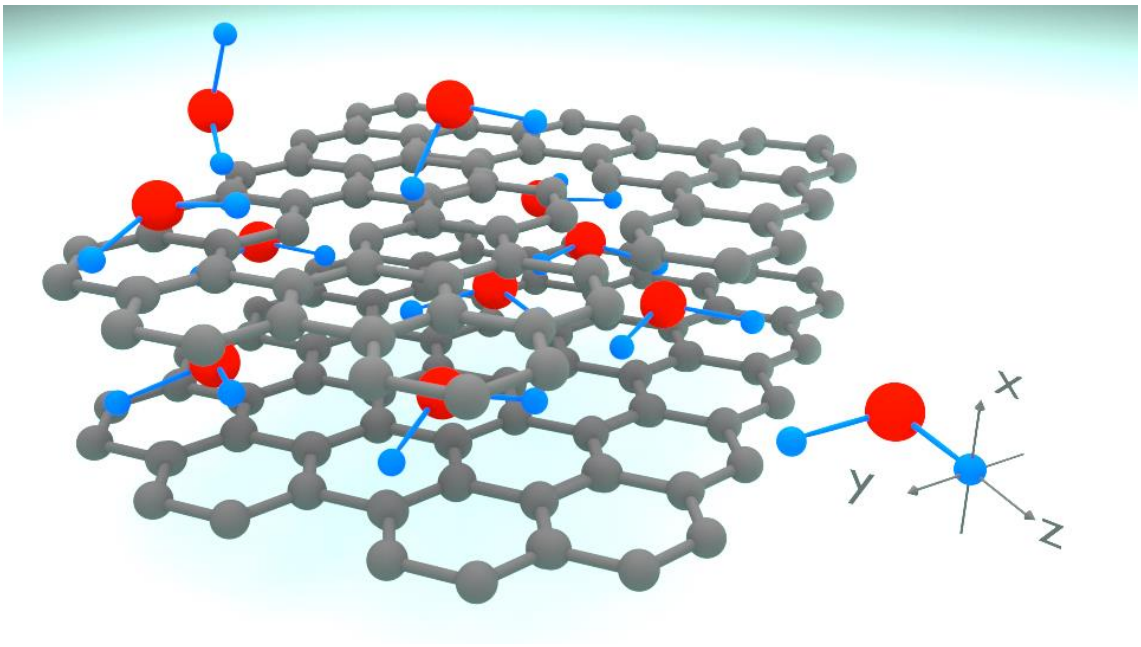

Figure 23. Orientation of the water molecules adsorbed on the GO surface and the axis reference system.

3.1.5. Hydrated proteins and DNA

Biological processes involving proton motions are prime candidates for the manifestation of quantum-mechanical effects. The interaction of water with proteins and macromolecules is essential for their physical configuration and biological function. Some work suggests that it is in fact the structure of the water surrounding the protein that drives configurational changes in these biomolecules. Likewise, the hydration structure of DNA can play a functional role by determining its conformation. More specifically, the conformational state of double-stranded DNA in solution is very sensitive to hydration: at low hydration, the most biologically relevant B-form undergoes conformational transitions to other forms. That hydration of DNA affects its conformation is also evident from the fact that dehydration stabilizes the A-form. Rather remarkably, quantum effects might be largely responsible for these phenomena [177]. Also, the importance of quantum-mechanical tunneling in enzyme catalysis continues to be a question of significant and heated debate. It has been proposed that enzymes have evolved to enhance tunneling in H-transfer reactions by employing finely tuned vibrational modes that serve to bring the hydrogen donor and acceptor atoms to an optimal reactive state. In this respect, tunneling may be used as a measure of protein motion that can be directly linked to catalysis, thereby enhancing our understanding of how enzymes make and break bonds [178]. Early DINS measurements were aimed at characterizing the proton NMDs from model peptides and polypeptides [179]. Subsequent DINS studies of hydration water were carried out following instrument upgrades on VESUVIO, which have enabled new capabilities in terms of count rate and spectral resolution. Lysozyme was chosen as a model system for the interpretation of experimental results, being a largely globular protein at room temperature, easily available, and well studied by other techniques. To investigate the interaction with water, samples were prepared at sub-monolayer water coverages. DINS measurements leading to H NMDs are shown in Figs. 24 and 25 [180].

In these data, no attempt has been made to subtract the response from lysozyme pro-

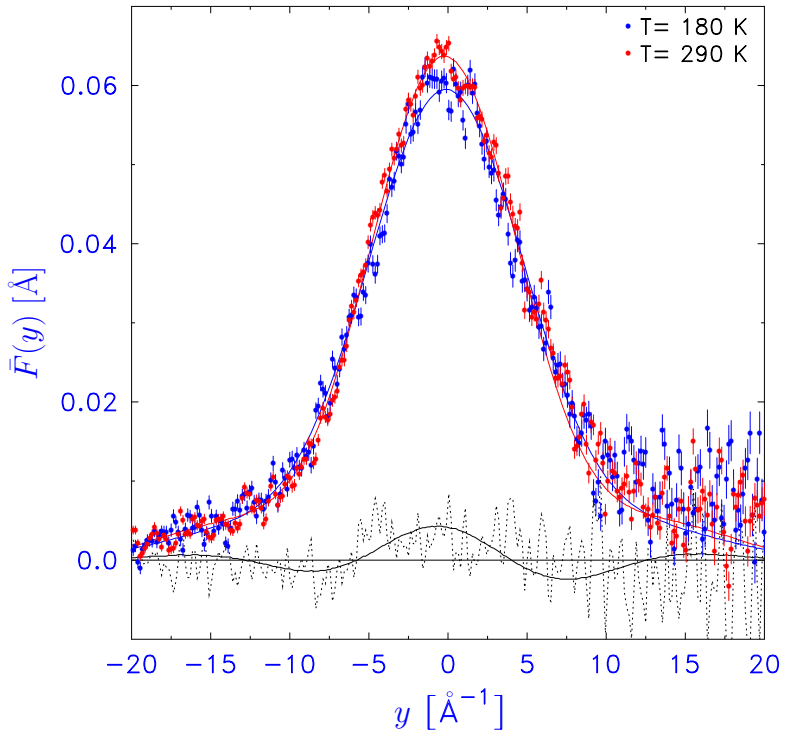

Figure 24. Detector-averaged profiles for hydrated lysozyme powder at T = 180 K (blue markers) and T = 290 K (red markers), together with their corresponding best fits (continuous lines). The difference between experimental profiles is reported as a black dashed line and the difference between the best fits is reported as a black continuous line.

tons relative to that arising from the water adsorbate. It is believed, however, that the protein-hydrogen NMD does not change significantly with temperature. It can be seen there is a significant difference in the H NMDs above and below what is believed to be a glass transition for the water on the surface, and that the higher-temperature data suggest coherent motion of some fraction of the protons. In particular, at 290 K, the results are consistent with a hydration shell that is slightly more dense than bulk water, with a shorter O-O distance confining the protons in a double well with the possibility of tunnelling between minima. These findings suggest that tunneling may occur even at room temperature on the hydration shell, with potential implications for biological function. These results complement the picture emerging from investigations of the collective dynamics at longer time scales. Indeed, the observed deviations from a purely classical behaviour of the collective dynamics probed on the millisecond timescale by dielectric spectroscopy have their origin in the single-particle dynamics probed by DINS, confirming that the dynamical behaviour of a hydrated protein is very well described in terms of a proton glass: a system showing dynamical arrest below a crossover temperature, and whose dynamical behaviour spans a broad range of timescales.

Studies on hydrated DNA have been aimed at exploring ZPE effects on the binding of water to A-DNA [181]. Dry DNA is not biologically active, and requires the uptake of

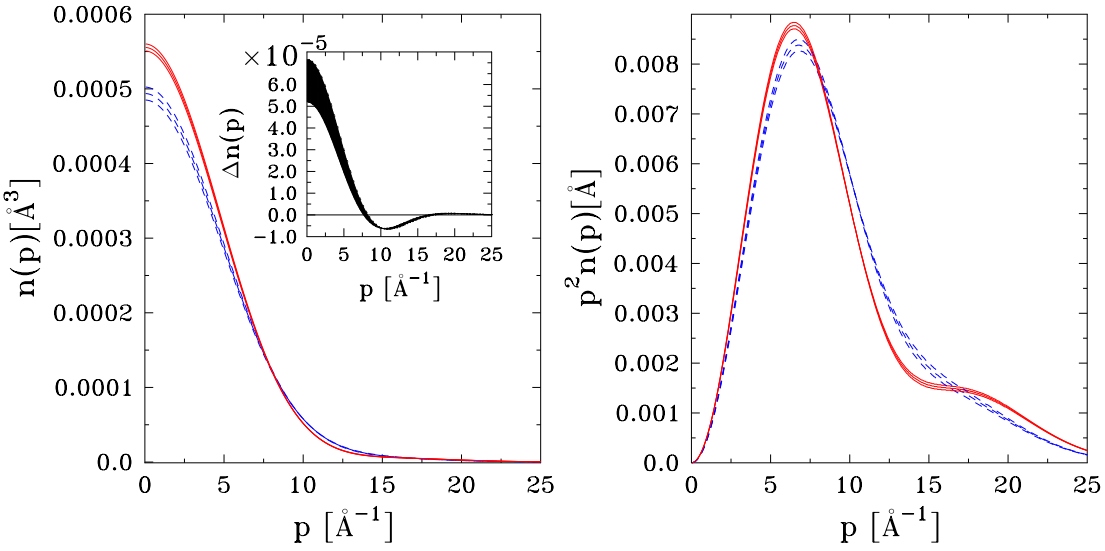

Figure 25. Left panel: H NMDs for hydrated lysozyme powder at T = 180 K (blue line) and T = 290 K (red line). The upper and lower lines delimit uncertainties derived from the line shape analysis. The inset reports their difference. Right panel: radial H NMDs for hydrated lysozyme powder at T = 180 K (blue line) and T = 290 K (red line). The upper and lower lines denote uncertainties derived from the line shape analysis.

about twenty water molecules to become so. As these are absorbed, the structure of the molecule changes, going from the A-phase to the biologically active B-phase. As it does so, ZPE motions of the proton in both the DNA and the adsorbed water change.

The electrostatic attraction between water and DNA and the associated energetic cost of distorting the DNA as the water is accepted into the structure just balance each other out. At higher levels of hydration, there seems to be little difference between the energy needed to remove a hydrating molecule and that required for the removal of one from bulk water. Whether the observed changes in kinetic energy of the hydrated water go to zero or not remains to be established. Calorimetric measurements show that this binding energy depends on the proportion of G-C to A-T base-pair bonds in the DNA. Further experiments on the kinetic energy of DNA as a function of hydration level and base-pair composition and temperature are needed to determine the extent to which coherence associated with ZPE motions may play a role in DNA function.

Figure 26 shows a comparison of H NMDs between dry and hydrated DNA via exposure to ambient conditions in order to achieve six water molecules/nucleotide. It is evident that the dry sample has a higher kinetic energy than the wet sample. It is also clear that some of the HBs in the dry DNA are double wells giving rise to coherent proton motions. The difference in kinetic energy is significant, amounting to 3.2 kJ/mol for the binding energy of the molecules, a figure which agrees with the energy measured by differential scanning calorimetry. From these data, it can be concluded that the entire binding energy in this case is due to changes in ZPE.

3.2. *Molecular hydrogen in carbon-based nanostructures*

Gas adsorption studies using DINS have been very scarce. DINS has been used to study He on activated carbon fibres at sub-monolayer coverages [182]. These NMDs were measured at 4.6 K and 10.2 K and $\langle E_K \rangle$ was found to be 30% higher than predictions based

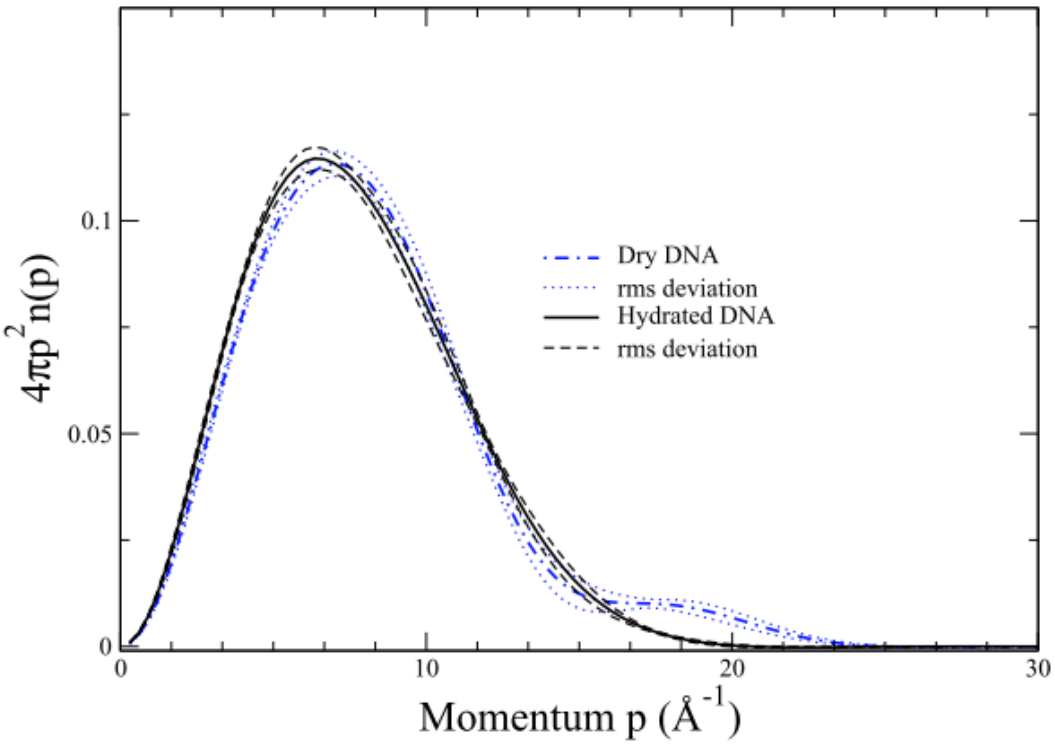

Figure 26. Radial H NMD in dry (blue dashed-dotted line) and hydrated (black line) DNA at room temperature. Upper and lower lines delimit uncertainties derived from the line shape analysis.

on a slit-pore geometry. This work has been extended to the adsorption of Ne in activated carbon [183] and He in cylindrical silica nanopores [184]. In the former case, adsorbed Ne was found to have a substantially higher $\langle E_K \rangle$ than the bulk solid owing to confinement effects. The adsorption of He in silica nanopores was explored as a function of pore diameter over the range 24-160 Å. These results were interpreted with a model where the adsorbate phase is arranged in concentric rings along the pores with $\langle E_K \rangle$ depending on the ratio between atomic and pore diameters. In what follows, we describe recent extensions of the realm of applicability of DINS to the investigation of gas-adsorption mechanisms in nanostructured materials and, in particular, the H_2 molecule. Given its potential as a clean energy vector, the behaviour of this seemingly simple molecular species as it interacts with novel materials continues to be the subject of extensive research worldwide, including the use of neutron-scattering techniques [185–187]. We take a close look at the case of H_2 uptake by KC_{24}, a nanoporous graphite intercalation compound (GIC) [126], to illustrate what can be learnt from the combined use of state-of-the-art DINS experiments and computational modelling using the conceptual framework and computational methodologies presented earlier in this work.

GICs are a versatile class of layered materials used for applications in batteries, supercapacitors, and superconductors [188]. Alkali metals readily intercalate into graphite to form superstructures of regular interlayer spacing, with a c-axis superlattice where n graphite layers separate each guest layer (so-called stage-n GICs). Alkali-metal GICs can adsorb gases such as H_2 and CH_4 and display uptake capacities comparable to other sorbents such as zeolites or activated carbons. A well-defined composition and regular

structure also make them suitable systems to explore the physical chemistry of H_2 uptake by metal-doped carbon-based materials. H_2 adsorption in GICs can occur in a variety of ways, in some cases leading to the breaking of the H–H bond, as has been observed in KC_8 [189]. Stage-2 compounds of stoichiometry MC_{24} (M = K, Rb, Cs) adsorb H_2 reversibly at ambient pressure up to $\sim 2H_2/M$ [190]. Below T = 100 K, MC_{24} is characterised by a commensurate $\sqrt{7} \times \sqrt{7}$ M superlattice bounded by a higher metal density in the inter-domain regions. The use of crystallography to study the arrangement of H_2 in GICs has proven elusive to date [188]. As alternative, H_2 uptake by RbC_{24} [191] and CsC_{24} [192] has been investigated using INS. The observed spectroscopic features at low energy transfers were attributed to the presence of two distinct adsorption sites. More recent work on KC_{24} at low temperatures has made extensive use of neutron diffraction, INS, and first-principles calculations to probe adsorption sites and GIC structure upon gas loading [193] – see unit-cell structure for H_2KC_{24} in Fig. 27. This ternary GIC of stoichiometry $(H_2)_xKC_{24}$ is characterised by a single adsorption site over the concentration range x=0–2. Moreover, neutron experiments have demonstrated the adequacy of PW-DFT calculations at describing the structure and energetics of $(H_2)_xKC_{24}$. Subtle effects such as GIC expansion upon H_2 uptake or the physisorptive nature of alkali-H_2 interactions appear to be well within the reach of present PW-DFT methodologies. In particular, the energies associated with orientational barriers are ∼100 meV, similar to experimental values for the enthalpy of adsorption [188]. These energies are two orders of magnitude larger than those found in undoped graphitic nanostructures [194]. The INS data also indicate a preferential pinning of the H_2 molecule along the quantisation axis. In addition, Purewal *et al.* [195] have observed a melting transition of the H_2 adsorbate at ∼35 K, a value well below any known phase transformation in this GIC. While insightful, the above studies have not been able to provide direct experimental signatures relating to the spatial arrangement of H_2 in KC_{24}. In what follows, we show how DINS has been used to address these pending questions in this important class of technological materials.

For a complex system like the ternary GIC $(H_2)_xKC_{24}$, it is critical to ensure that the desired experimental conditions in terms of molecular uptake have been attained. Sections 2.3.1 and 2.3.2 have already explained how for the case of elastic scattering (*i.e.*, no energy filter), TOF techniques on an inverted-geometry instrument like VESUVIO can be used to determine the incident neutron wavelength at a particular scattering angle and, consequently, obtain neutron-diffraction patterns – see, in particular Fig. 14. Moreover, the use of a backscattering geometry has the advantage of a high intrinsic resolution approaching 0.2% [196], in addition to the possibility of simultaneous structural and spectroscopic measurements. Such capabilities have already been used extensively on the IRIS spectrometer [197] to study H_2 uptake in the same GIC [193]. Other neutron spectrometers where a similar experimental approach is also available include OSIRIS [198–200] and TOSCA [201, 202], also located at the ISIS Facility.

In this particular case, simultaneous neutron-diffraction measurements during the DINS experiments were critical to ascertain *in situ* the alignment of KC_{24} with and without H_2. As a stage-2 GIC, KC_{24} displays a prominent (003) Bragg reflection at ∼2.9 Å. H_2 adsorption leads to a readily detectable ∼3% expansion of the GIC lattice along the c-axis [193]. Figure 28 shows diffraction data for $(H_2)_xKC_{24}$, obtained as a function of coverage and sample orientation. The presence of two diffraction features at ∼2.9 Å and ∼3.0 Å confirms the existence of well-defined domains of pristine and hydrogenated KC_{24}. At a coverage x=2, no diffraction features associated with pristine KC_{24} are observed, whereas at x=1 there is an equal proportion of both phases. These results confirm the structural integrity and high quality of the sample before and after

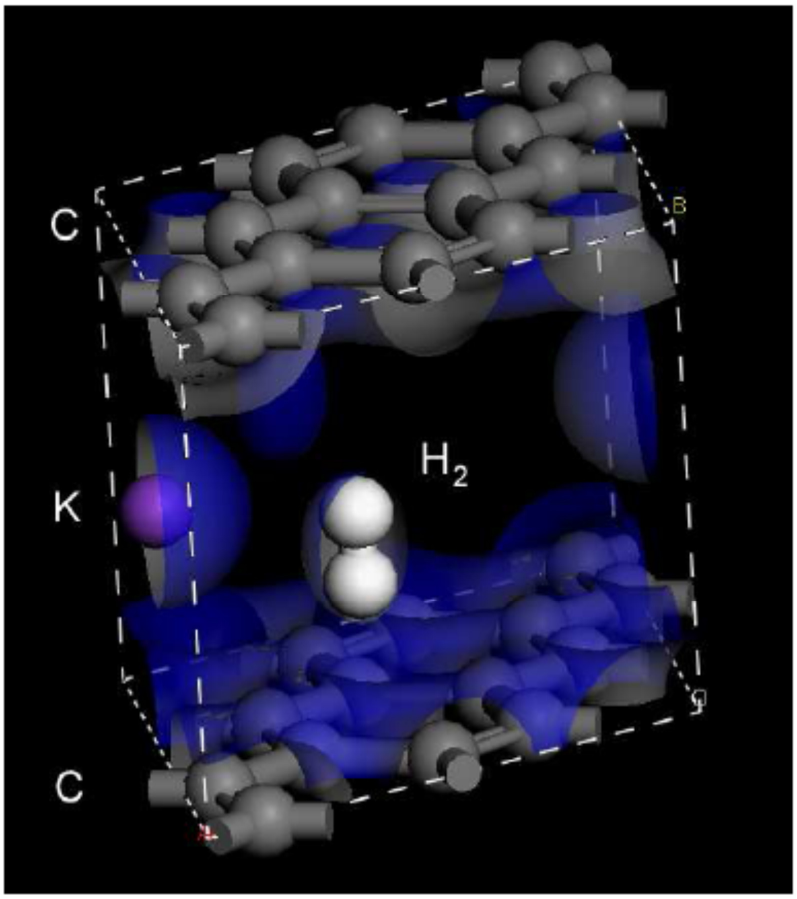

Figure 27. Minimum-energy unit-cell structure of H_2KC_{24} obtained from PW-DFT calculations (H: white; C: black, K: purple). The crystallographic *c*-axis runs along the vertical direction.

H_2 uptake.

3.2.1. Adsorption energetics

We first consider the isotropically averaged proton NCP, obtained by averaging over all sample orientations. Figure 29 shows a comparison between these measurements and those from liquid H_2. The instrumental resolution shown in this figure is *ca.* one order of magnitude narrower than the observed proton NCP widths. In this situation, its effect

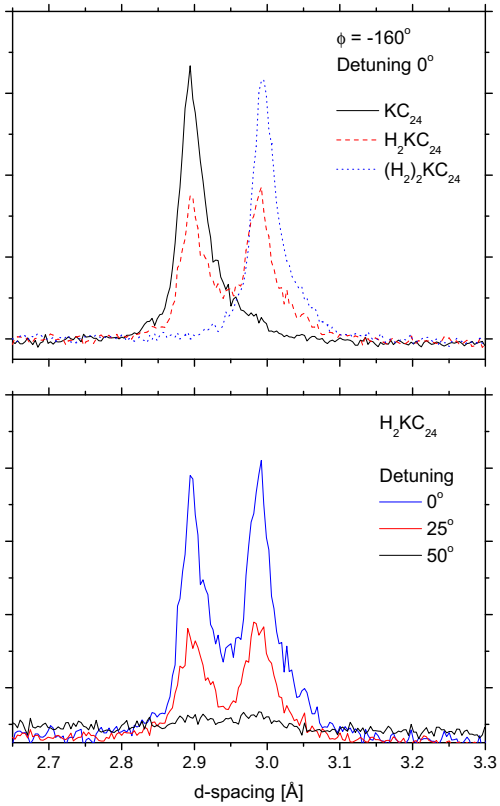

Figure 28. Neutron diffraction data at a fixed scattering angle ϕ as a function of H_2 coverage (top) and c-axis orientation relative to the transmitted beam (bottom). From these data, we obtain a mosaic spread of $\sim$15°. See the text for further details.

on the NCP is negligible, amounting to $\sim$1% of the total width in momentum space, as these add in quadrature to a very good approximation, *i.e.*, $\sigma^2_{obs} = \sigma^2_H + \sigma^2_{res}$. Similar remarks would also apply to any other VESUVIO data displaying comparable proton NCP widths, further highlighting the unrivalled spectral resolution of the VESUVIO spectrometer in the DINS regime, as explained earlier in Section 2.3.2.

The isotropic NMD for the proton in $(H_2)_xKC_{24}$ is markedly different from bulk H_2, as evidenced by a distinct spectral broadening. Such a feature indicates an enhanced interaction of H_2 with the surrounding medium. We recall that a broadening of the NCP in y-space results in a concomitant reduction in the spatial extent of the proton wavefunction as a result of a stronger confining potential. To be more quantitative, we can calculate the second moment σ_{iso} of the isotropic NCP $J_{iso}(y)$. We obtain $\sigma_{iso} = 3.17\pm0.02$ and 3.89 ± 0.04 Å^{-1} for the bulk and adsorbed proton NCPs shown in Fig. 29, respectively. The value for the bulk agrees well with 3.34 Å^{-1}, obtained earlier by Mayers [203]. Physically, the overall proton NCP arises from the convolution of vibrational $J_{vib}(y)$ and translational $J_{trans}(y)$ contributions for the rotationless (J=0) state of the H_2 molecule. The latter was negligible in comparison to the vibrational term, given a strong H–H bond of harmonic energy $\sim$500 meV and momentum width $\sigma_{vib} = 5.57$ Å^{-1}. The total width of $J_{iso}(y)$ for randomly oriented H_2 is dominated by the three-dimensional

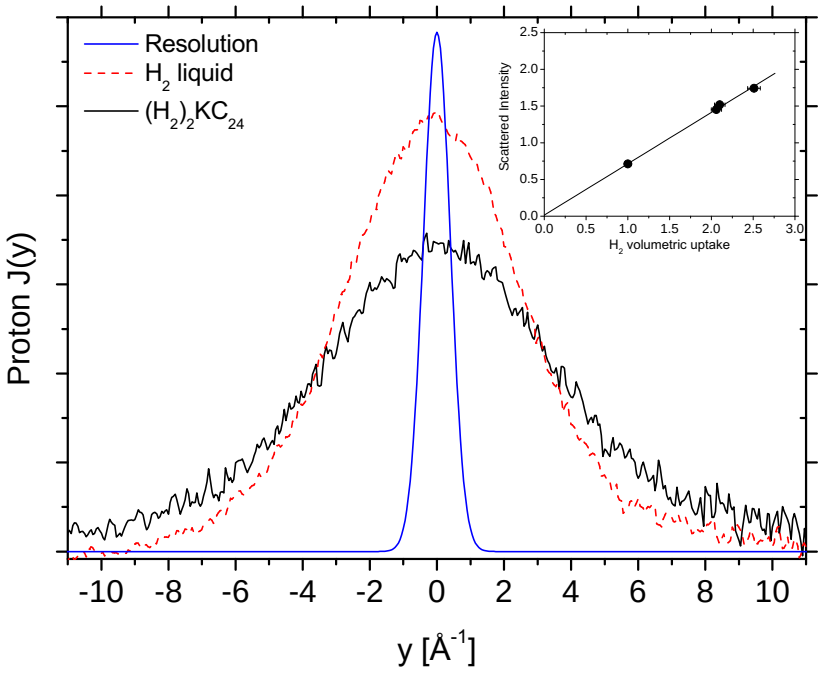

Figure 29. Isotropic proton NCPs for $(H_2)_2KC_{24}$ at T = 1.5 K and liquid H_2 at T = 20 K. For the purposes of comparison, both profiles have been normalised to unit areas. The blue curve corresponds to the instrumental resolution rescaled by an arbitrary constant. The inset shows the dependence of the total scattered intensity on volumetric dosage.

average of the NCP width along the bond axis, amounting to $5.57/\sqrt{3}$ Å^{-1} = 3.22 Å^{-1}.

The additional NMD width of H_2 in KC_{24} arises from contributions from the librational (*lib*) and translational (*trans*) centre-of-mass motions of the molecular adsorbate. Assuming Gaussian $J(y)$'s, a reduced second moment $\sigma \sim 2.2$ Å^{-1} accounts for the observed differences between adsorbed and bulk H_2. Dimensionally, this extra NCP width is partitioned between two-dimensional angular oscillations of the H atoms orthogonal to the H–H bond in the molecule-fixed frame, and three-dimensional translations of the entire H_2 molecule. The overall proton NCP width can then be written as

$$\sigma_{iso}^2 = \frac{1}{3}\left[\sigma_{vib}^2 + 2\sigma_{lib}^2 + 3\sigma_{trans}^2\right]. \tag{68}$$

Since σ^2 scales linearly with mass and characteristic frequency, *i.e.*, $\sigma^2 \propto M\omega$, Eq. (68) can be used to examine the origin of the observed spectral broadening. Previous work [193] has identified the fundamental transition for H_2 librations at ∼50 meV, which translates into σ_{lib} ∼1.8 Å^{-1}. From the measured value of σ_{iso}, we can then estimate $\sigma_{trans} \sim 1.6$ Å^{-1} and an energy of ∼40 meV. Such a value is in reasonable agreement with the value of 27 meV for the vibrational modes of the K–H_2 complex obtained in previous PW-DFT studies [193]. These translational motions are dominated by interac-

tions between the H_2 molecule and the K ions. The inset in Fig. 29 shows how the total intensity scales with H_2 coverage. Within a confidence band of 2–3%, we find a robust linear correlation between the amount of adsorbed H_2 and total scattered intensities. These results are also consistent with the diffraction data shown in Fig. 28 where it is shown that x=0 and 2 give rise to one diffraction feature whereas x=1 shows two equally populated domains of pristine and hydrogenated KC_{24}.

Within experimental uncertainties, we also note that σ is constant up to $x = 2.0$ and decreases slightly at $x = 2.5$. The latter result is consistent with the overloading of the sample with an extra mole fraction of 0.5 above the known H_2 saturation coverage of $x = 2.0$. From this dependence on coverage, we can also establish an upper bound for the characteristic energy scales associated with intermolecular H$\cdots$H interactions. Within the harmonic approximation, our uncertainties in the determination of reduced second moments imply a spread in NCP widths of at most $\sim$0.8 Å^{-1}, corresponding to an upper conservative bound of $\sim$10 meV.

These DINS results evince the presence of three well-defined energies associated with the adsorbed H_2 phase, corresponding to high-frequency intramolecular H–H vibrations, followed by intermolecular librations and translations of a similar frequency. Adsorbate-adsorbate interactions fall below sensitivity limits, yet from an analysis of experimental uncertainties in NCP widths, they are significantly less than well-defined motions associated with isolated adsorbate molecules.

3.2.2. Comparison to theoretical predictions

Following the formalism introduced in Section 2.2.2, PW-DFT calculations on a H_2KC_{14} unit cell were performed for a quantitative comparision with DINS data. The phonon calculations were restricted to the Γ-point in the evaluation of the double sum in Eq. (38). Figure 30 shows the calculated H PVDOS and NMD widths along with the experimental data. NMD widths are shown as a function of energy cutoff to highlight their dependence on vibrational energy. The sharp and isolated feature at 533 meV dominates the NMD response and corresponds to H–H internal vibrations, largely unaffected relative to a gas-phase value of 546 meV [41]. The agreement between experiment and calculation is excellent.

Table 8 shows NMD widths for all atoms in the unit cell. For H, the calculated isotropic value of 3.79 Å^{-1} compares very well to DINS (3.89$\pm$0.04 Å^{-1}). PW-DFT also predicts a marked anisotropy of NMD widths parallel and perpendicular to the c-axis as a result of the preferential alignment of the H–H bond axis. For C, the anisotropy is (nearly) cylindrically symmetric about the c-axis and it is reversed compared to H. Minor differences are seen for different C atoms owing to the presence of K and H, which tends to weaken C–C bonds due to electron transfer from K into the nearby C atoms. The value of 13.74 Å^{-1} for in-plane bonding is in excellent agreement with an experimental value of $\sim$14.0 Å^{-1} for Papyex [205]. An average out-of-plane C width of 8.23 Å^{-1} is significantly smaller than $\sim$11 Å^{-1} in graphite, caused by a sizable decrease in the interaction between graphite planes separated by 5.6 Å in comparison to 3.35 Å in graphite. Such a reduction in NMD width arises from a softening of out-of-plane carbon ZPEs by $\sigma^2_{x,y}/\sigma^2_z = (13.74/8.23)^2 \sim 2.8$. This value also explains the appearance of Raman features in K-doped graphene at 200 and 69 meV associated with C_{xy} and C_z vibrations, respectively [206]. NMD widths associated with K are narrower than those characteristic of C or H, and display a more marked anisotropy on the $x-y$ plane. A larger value for the z-component arises from a stronger interaction with the C layers. In-plane motions are also softer because of the non-specific character of the Coulomb interaction between the

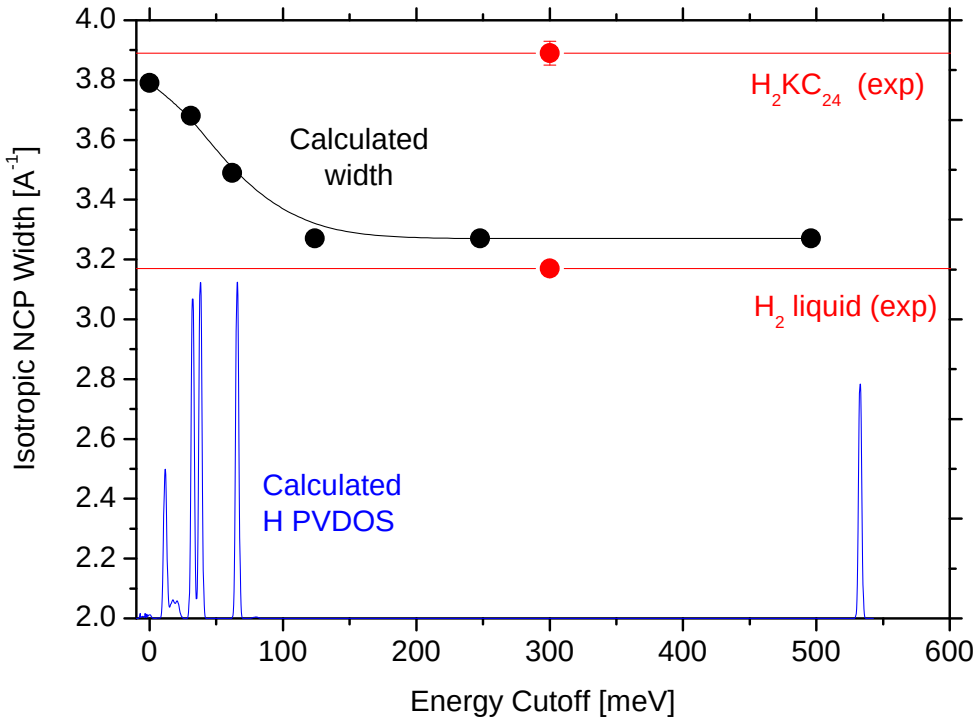

Figure 30. Dependence of the calculated H NMD width on the lower-energy limit of integration of the underlying PVDOS. The black data shows that this integration explores the dependence of NMD width on the progressive exclusion of features in the PVDOS, *i.e.*, a zero-energy cutoff implies that *all* normal modes are taken into account. Red data shows experimental values. The blue trace shows the calculated H PVDOS.

K ion and the diffuse negative charge residing on the C layers. All in all, these calculations demonstrate the added-value provided by state-of-the-art computational modelling in the interpretation of DINS data beyond heuristic or phenomenological models.

3.2.3. Anisotropic response and molecular alignment

The computational results presented above can be tested further by considering the anisotropy of the proton NMDs. This response can be obtained from the DINS data as a function of sample orientation χ over the range $\pm 90°$, where χ=0 corresponds to complete alignment of $\vec{Q}$ along the crystallographic c-axis. The results of this analysis for coverages x=1 and x=2 are shown in Fig. 31. The proton NCP widths are symmetric about $\chi = 0°$ and vary between $\sim$3.5 Å^{-1} for $\chi = \pm 90°$ to $\sim$4.5 Å^{-1} for $\chi = 0°$. Qualitatively, this behaviour indicates a stiffer spatial extent of the proton wavefunction along the GIC surface normal z compared to the $x-y$ plane. This result indicates a pinning of the H–H bond along the GIC c-axis, in qualitative agreement with the minimum-energy geometry predicted by the PW-DFT calculations. Moreover, there are no differences between the two H_2 coverages investigated, confirming that adsorbate-adsorbate interactions play a minor role.

Table 8. Calculated NMD widths, where z is parallel to the c-axis – *cf.* Fig. 27. Average values are shown in the last column, calculated using Eq. (39).

Atom	$\sigma(\hat{\mathbf{x}})/\text{Å}^{-1}$	$\sigma(\hat{\mathbf{y}})/\text{Å}^{-1}$	$\sigma(\hat{\mathbf{z}})/\text{Å}^{-1}$	$\sigma/\text{Å}^{-1}$
H	2.29	2.13	5.78	3.79
H	2.29	2.13	5.78	3.79
C	13.73	13.75	8.21	12.18
C	13.77	13.74	8.12	12.17
C	13.68	13.75	8.16	12.15
C	13.76	13.76	8.56	12.27
C	13.72	13.82	8.56	12.28
C	13.73	13.68	7.95	12.10
C	13.81	13.64	8.16	12.16
C	13.74	13.76	8.62	12.28
C	13.84	13.75	8.01	12.19
C	13.64	13.73	8.03	12.10
C	13.75	13.77	8.33	12.22
C	13.84	13.73	8.17	12.21
C	13.71	13.66	8.14	12.12
C	13.68	13.74	8.14	12.14
K	1.30	3.24	4.66	3.36

Quantitative estimates of observed anisotropy can be obtained by considering the angular dependence of the NCP parallel (par) and perpendicular (per) to the c-axis. In this case, $J(y;\chi)$ displays the following angular dependence

$$J(y;\chi) \sim \exp\left[-\frac{y^2}{2}\left[\frac{cos^2\chi}{\sigma_{par}^2}+\frac{sin^2\chi}{\sigma_{per}^2}\right]\right] \tag{69}$$

where the parallel and perpendicular NCP widths obey the relations $\sigma_{par} = \sigma_z$ and $\sigma_{per} = \sigma_x = \sigma_y$. NCP widths as a function of angle χ are then obtained by blurring the computational predictions by an intrinsic angular resolution R, that is,

$$\langle J(y;\chi)\rangle = \int R(\chi'-\chi)J(y;\chi')d\chi' \tag{70}$$

where $J(y;\chi)$ is given by Eq. (69) and R is taken as the convolution of GIC mosaic spread with the angular spread of the instrument. The resulting NCP width $\langle\sigma(\chi)\rangle$ is obtained by calculating the second moment of $\langle J(y;\chi)\rangle$. Using the experimental results to find values for σ_{par} and σ_{per} using Eq. (70) leads to the black-dashed curved in Fig. 31 and anisotropy parameters $\sigma_{par} = 4.45\pm0.07$ Å^{-1} and $\sigma_{per} = 3.55\pm0.08$ Å^{-1}. The associated isotropic value of $\sigma_{iso} \sim 4$ Å^{-1} is consistent with the one obtained from the isotropic $J(y)$. The weak orientational dependence of the reduced second moments of the proton NCP explains why this particular system renders itself to a reasonably straightforward description in terms of spatially averaged intra and intermolecular modes.

A similar procedure can be followed to compute a PW-DFT prediction for the angular dependence of proton NCP widths. Using the values reported in Table 8, these results are shown by the blue trace in Fig. 31. Good numerical agreement is obtained between these first-principles results and experiment when the scattering vector is preferentially aligned along the c-axis. Nonetheless, the PW-DFT calculations clearly overestimate the

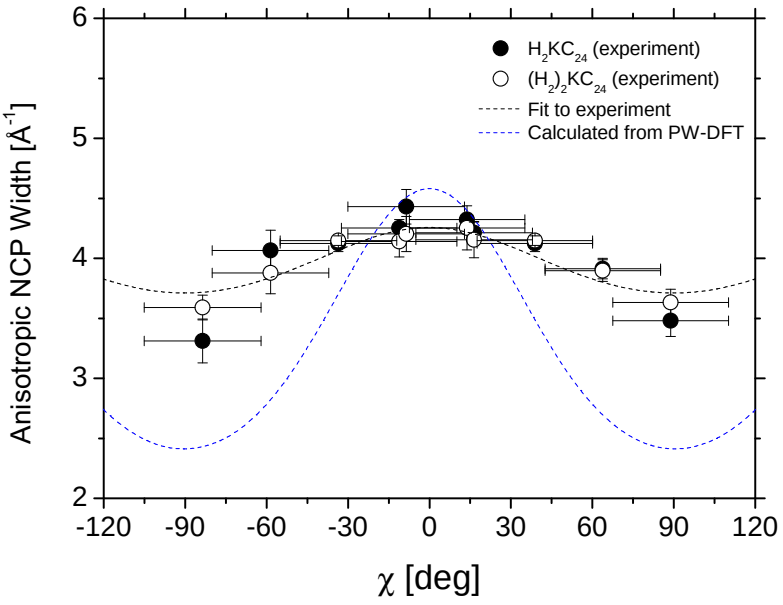

Figure 31. Dependence of proton NCP widths on χ for coverages $x = 1$ and 2. For further details, see the text.

extent of the anisotropy, with values for the proton NCP widths as low as $\sigma \sim 2.5$ Å^{-1}. The slight pinning along the c-axis is qualitatively consistent with the minimum energy geometry found in the PW-DFT calculations, albeit far less pronounced. From these results, it is clear that the computational model for the binding of H_2 to KC_{24} is not sufficient to provide a fully quantitative description of H_2 motions normal to the GIC c-axis.

Two scenarios can explain why the PW-DFT calculations underestimate the extent of proton localisation for in-plane motions. One possibility is a higher binding energy in the real material compared to the computational predictions. This being the case, comparison of experimental and theoretical NCP widths would imply an additional contribution to the NCP width at $\chi = 90$ ° of $\sigma \sim 2.8$ Å^{-1}, as well as an associated vibrational energy of $(\sigma^2/\sigma_z^2)\omega_{vib} \sim 120$ meV, where $\omega_{vib} = 533$ meV is the vibrational energy associated with vibrations along the H–H bond. From these energy scales, we can rule out this scenario as such an energy well exceeds the known experimental value of 88 meV for the total binding energy of H_2 in KC_{24} [195, 207]. Also, the PW-DFT model can account for ∼90% of this binding energy as arising from the interaction between the potassium ion and H_2 [207].

An alternative scenario implies a broader orientational distribution of the H–H bond axis than predicted by the calculations. Since there is no available evidence to indicate the presence of more than one adsorption site, this phenomenon must be intrinsic to a single H_2 molecule. In previous computational studies [193], the calculated H_2 orientational potential was found to be slightly anisotropic, with an energetic preference for H–H alignment along the c-axis. Such a disparity in energy barriers for H_2 rotations parallel and perpendicular to the K–H_2 bond implies facile two-dimensional rotational

motion about the latter. In order to explain the INS data, a delocalisation model for H_2 translational motions had to be invoked. The result of such a (purely classical) averaging process was to recover the same symmetry and functional form for the orientational potential as that found in the INS experiments. In the language of quantum mechanics, such an averaging process, however, does not imply that the underlying H_2 molecular wavefunction lacks a significant amplitude for H–H geometries orthogonal to the c-axis. The present DINS experiments are consistent with these considerations. Further, they suggest that delocalisation of the H–H bond axis beyond what is predicted by current PW-DFT methodologies is significant and cannot be neglected. Also, the interaction potential of H_2 with the substrate does not mix *para* and *ortho* nuclear-spin manifolds and these are independent of each other when considering rotations and librations about the centre of mass. It, therefore, appears as if particle exchange might also play an important role in this particular case, the very same process responsible for the entanglement of nuclear-spin and rotational degrees of freedom in isolated homonuclear diatoms such as H_2 [208]. The consequences of such effects are difficult to predict quantitatively unless the H_2 potential-energy surface in the GIC is mapped in detail and NQEs are fully taken into account. For H_2, this is not a trivial task given the presence of intramolecular exchange effects from the outset, *i.e.*, proton exchange associated with rotations about the molecular centre-of-mass need to account for its fermionic nature. PI calculations as those described in Section 2.2.3 still rest on this hard-to-treat approximation.

Notwithstanding the above limitations, the anisotropy data presented in Fig. 31 can be used explore the underlying H_2 librational wavefunction Ψ. In the free-rotor $|JM\rangle$ basis, Ψ can be expanded as a series of the form

$$\Psi = \sum_{J,M} c_{JM} \, |JM\rangle \tag{71}$$

where $|JM\rangle \equiv Y_{JM}(\chi, \varphi)$ is a spherical harmonic, and a given $|JM\rangle$ state has a rotational energy $E_J = B_{rot} J(J+1)$ with $B_{rot} = 7.35$ meV [41]. For the *para*-H_2 ground state, only even-J terms contribute to this sum. The nearest of these are characterised by rotational energies E_J of 44 (J=2), 147 (J=4), 252 (J=6), and 530 meV (J=8), the latter one being almost degenerate with the first vibrationally excited state. The orientational potential $V(\chi, \varphi)$ defining the librational interaction of H_2 with the GIC will introduce contributions from excited $|JM\rangle$ states into the ground-state, free-rotor wavefunction. Such an admixture is inversely proportional to the energy separation between levels. Thus, the combination of a relatively restricted subset of possible $|JM\rangle$ states ($J = 2, 4, 6...$) because of intrinsic particle-exchange effects, as well as their high energies above the ground state provide a qualitative rationalisation as to why departures from a purely isotropic $|00\rangle$ ground-state wavefunction require a strong orientational potential $V(\chi, \varphi)$, with orientationally energy barriers above 100 meV. These remarks can be made more quantitative by going back to the model introduced in Ref. [193] to rationalise the INS spectrum of this system. Such a potential is of the form $V(\chi, \varphi) = V_\Theta \sin^2 \chi$ with $V_\Theta = 137$ meV. In this case, inclusion of terms up to just $J = 4$ in the sum given by Eq. (71) is sufficient to converge the eigenvalues for the energies of ground and first excited states to within ∼1%. Free-rotor contributions from J=0 and 2 are dominant and of a similar weight, followed by a relatively modest contribution from J=4. Higher-order terms are negligible. Therefore, the small moment of inertia of the H_2 molecule combined with intramolecular quantum-mechanical exchange make it a real challenge to pin the H–H axis along a well-defined direction.

3.2.4. What DINS has taught us about hydrogen in the solid state

This case study has been chosen to show how state-of-the-art DINS and first-principles electronic-structure calculations can be used to study the adsorption of H_2 in KC_{24}, a prototypical GIC material. The intermolecular forces at play are stronger than those typical of carbon-only nanostructures, where dispersive interactions can account for the bulk of the interaction. DINS experiments on the VESUVIO spectrometer enabled the simultaneous characterisation of this material using high-resolution neutron diffraction and DINS. These additional capabilities were crucial to establish the integrity and degree of orientation of the substrate during *in situ* gas loading. Future DINS work involving the adsorption of H_2 and other gases on porous sorbents will undoubtedly benefit from these unique capabilities and further instrument developments.

The DINS response of H_2 has been analysed in detail, and comparison with the DINS response from bulk liquid H_2 has been instructive in order to assess the effect of intermolecular interactions between H_2 and the host. To a very large extent, the isotropic NCP widths are the result of the successive convolution in momentum space of all intra and intermolecular motions of the H_2 molecule. Furthermore, the coverage dependence of the DINS data has also provided new insights into the energy scales associated with H$\cdots$H interactions. For $(H_2)_xKC_{24}$ (x<2), these energies are of *ca.* 10 meV. Adsorbate-adsorbate interactions lie at the low end of the scale compared to other motions of individual H_2 molecules. It is important to note that such a quantity is not amenable to direct scrutiny using other spectroscopic techniques.

The oriented nature of the GIC allowed for a close scrutiny of the the H_2KC_{24} complex, to highlight where current methodologies based on a harmonic or single-particle description of hydrogen motions fail rather dramatically. The observed anisotropy in the proton NMD is far less pronounced than theoretical predictions yet, at a qualitative level, they show a similar behaviour, characterised by a preference for the H_2 molecule to be aligned along the crystallographic *c*-axis. Pinning the H–H axis along a well-defined direction in space appears to be a rather difficult task for physisorbed H_2, in spite of the presence of considerable energy barriers for rotation (>100 meV). It thus appears as if additional binding mechanisms approaching the chemisorptive regime such as those responsible for Kubas-like dihydrogen complexes [209] are required to achieve a strong pinning of H_2 in hydrogen-storage media. In either case, gaining further insights into the underlying mechanisms responsible for the binding of the H_2 molecule necessarily implies recourse to theoretical approaches where NQEs beyond the harmonic approximation (*e.g.,* PI methods) and possibly higher-order effects such as particle exchange must be incorporated from the outset.

4. Outlook and perspectives

The past decade has been an exciting one for eV neutron spectroscopy and its application across physics, chemistry, biology, and materials science. In addition to providing a critical account of the systems and materials studied during this period, this review has also presented a summary of the key conceptual and practical aspects of the technique, followed by specific case studies to enable you to identify aspects of your own work in which eV neutron spectroscopy could provide new and hitherto unexplored insights.

At this juncture, the technique has clearly moved beyond its intended use in the early days to explore fundamental systems and is now entering an exciting new era. Progress has been spectacular on a number of fronts owing to the judicious exploitation of pre-

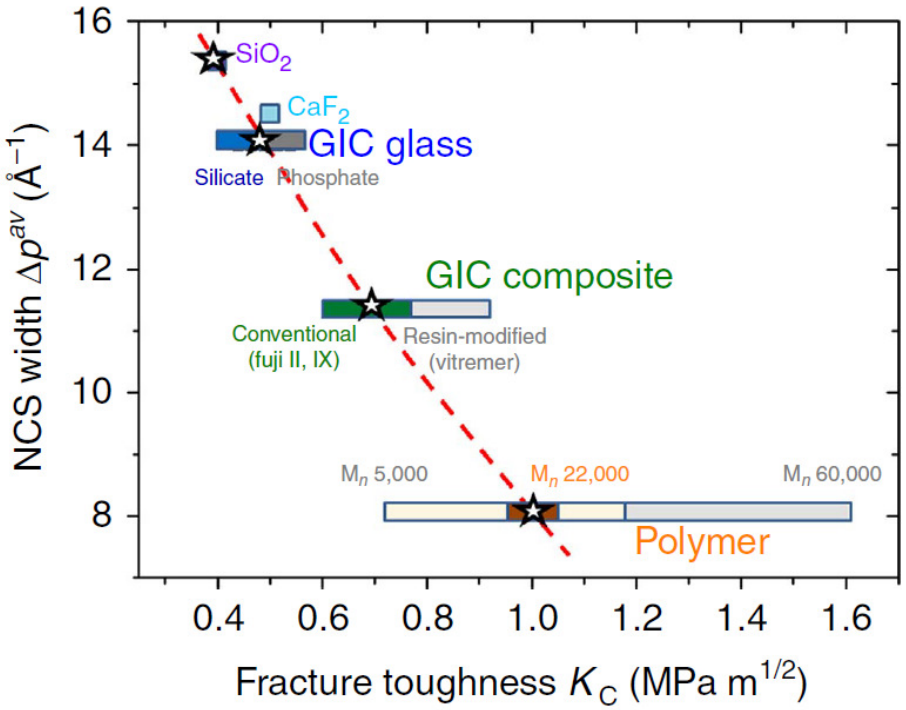

Figure 32. Correlation between average NMD width (ordinate axis) and fracture toughness (abscissa) for a range of materials including glass-ionomer cements (labelled GICs in the figure), polymer, and glass. Reproduced from Ref. [211].

viously inexisting synergies, the most notable ones being the progressive integration of last-generation computational modelling and analysis tools into existing experimental programmes, as well as steady and significant advances in neutron instrumentation and experimental strategies. We do not expect less from the years to come. In what follows, we offer our (by no means exhaustive) thoughts and reflections on how the field might evolve in the foreseeable future. For a more extensive account of ongoing discussions by the community, the reader is also referred to the proceedings of a recent international workshop [210].

In terms of new scientific opportunities, possibilities remain practically boundless and, to date, do not appear to be limited by the apparent complexity of the target material. This particular point is nicely illustrated by the very recent work of Tian *et al.* [211], where DINS has been used to study bioactive glass-ionomer cements. This work is novel in several important respects. First of all, DINS observables were monitored as a function of *time* during the setting process. The temporal evolution of NMD widths for individual atomic species was found to be markedly non-monotonic and characterized by abrupt and previously unreported features. As shown in Fig. 32, concentration-averaged NMD widths were also found to correlate well with the inverse of fracture toughness across a range of related materials, enabling the identification of a glass-ionomer coupling point, an early setting point where material toughness unexpectedly recovers, and a final and slow increase associated with an asymptotic decline towards long-term fracture-test val-

ues. The inherent complexity of these materials makes it prohibitely expensive from a computational viewpoint to tackle them at a quantitative level using *in silico* methods at this point in time. Nonetheless, this work demonstrates that the search for previously unexplored *correlations* between DINS observables and other material properties provides a useful framework for the future use of the technique. This is an area of work where much remains to be done across a wide spectrum of materials and situations of practical interest. To this end, the ability to perform parametric DINS studies becomes an important prerequisite. These can include physical variables such as temperature, pressure, or time, as well as others of relevance to chemistry (pH, ionic strength) or to materials science and engineering (preparation method, fatigue levels).

Without much doubt, light atomic species like H, D, Li, B, or C have been and will continue to be primary targets for future DINS studies, particularly in the context of *in situ* and *operando* studies of materials for energy, where we emphasize once more the suitability of neutron-scattering techniques to achieve this goal under realistic, real-world situations. Both Li and B are key elements for light-weight applications related to energy conversion and storage, *e.g.,* lithium-based battery electrodes for charge storage or metal-based borohydrides for hydrogen storage. In these two particular cases, the use of thermal and cold neutrons typically requires costly and cumbersome isotope-substitution protocols to avoid excessive absorption and attenuation. Owing to the linear dependence of neutron absorption on wavelength, studies using eV neutrons do not suffer from this limitation. High-surface-area and nanoporous materials like metal-organic frameworks are also well within the scope of DINS and MANSE, not only to explore molecular uptake and adsorption (as illustrated in Section 3.2), but also to probe the supramolecular dynamics that dictate material flexibility and (still-controversial) pore-breathing phenomena [212] in a mass-selective manner. Similar remarks apply to molecular and macromolecular intercalation in graphene-related and other layered materials, which has been already surveyed using neutron diffraction under the sudden approximation (total scattering) and high-resolution INS [213–221]. In this context, it is important to note that a quantitative theoretical description of soft layered materials remains a challenging task for DFT-based methods [222, 223], and such a gap in our understanding may require revisiting prototypical systems from an entirely new perspective as that offered by eV neutron spectroscopy. Beyond the above, the use of DINS and MANSE in chemical catalysis remains uncharted territory beyond a handful of early pilot studies using first-generation eV instrumentation [224, 225]. This is an area of research where neutron techniques and, in particular, INS have been gaining considerable ground in the recent past [226] and, therefore, one would expect interesting developments on the horizon.

The inclusion of D in the series of light elements listed above is by no means coincidental. Although the study of isotope-substitution effects might at first look like an academic exercise with limited practical value, such a view is clearly at odds with the increasing development and use of so-called 'heavy drugs' by the pharmaceutical industry to increase stability as well as control dose and uptake kinetics [227, 228]. Gaining a solid quantitative understanding of polymorphism in these compounds upon H/D substitution, for example, is certainly within the scope of eV neutron spectroscopy. Other phenomena of general relevance include the inversion of H/D isotopic fractionation ratios in the atmosphere at temperatures above ambient, a phenomenon that has been explained on the basis of competing quantum effects – *cf.* Section 3.1.3 and Ref. [105]. Furthermore, extension of these to the study of heavier masses is also possible at this point in time. Several examples have been presented in this work, particularly in the study of disordered and metastable states of matter where eV neutron spectroscopy may be viewed as the natural spectroscopic counterpart of total-scattering techniques and pair-

distribution-function methods for structural determination [229]. Beyond these cases, important phenomena remain to be explored with eV neutrons. These include: the coupling of electronic and nuclear motions underpinning the mechanism of superconductivity as well as the optical and electronic properties of high-T_c cuprates and pnictides [230], carbon-based materials [231, 232] and, more recently, molecular hydrides [233]; phonon softening and anharmonicity in thermoelectrics at high temperature [234], where we note that eV neutron spectroscopy is not affected by the strong suppression of spectral features associated with temperature or dynamical disorder, a feature which oftentimes imposes severe limitations on the use of other spectroscopic techniques; or subtle NQEs affecting the thermodynamic phase behaviour and metastability of ubiquitious materials, as explored recently using computer simulation for the case of the crystallisation of stishovite from shock-compressed fused silica [235]. Further instrumentation developments would certainly consolidate efforts to date, including the use of MANSE and resonant neutron capture.

Water and aqueous systems have been studied quite extensively, as evidenced by the growing number of examples and the emphasis given in this review to this important area of science. We do not expect that the interest seen so far will fade, given the enormous number of situations of practical and technological relevance involving aqueous media. The use of DINS and INS to probe the fundamental properties of solid, liquid, and supercritical water has been of pivotal importance to test theoretical and computational predictions beyond observables related to structural properties. Substantial efforts in this direction continue in order to find a predictive universal model for water that can account for all of its physico-chemical properties and long list of anomalies [236]. In the context of neutron spectroscopy, Fig. 33 gives a visual summary of what has been achieved to date. We have seen in Section 3.1 that the primary contribution to $\langle E_K \rangle$ of the proton in water comes from the ZPE of the OH-stretch vibration. This contribution can be evaluated via integration of the VDOS (obtained from INS or calculations) around those spectral features associated with this mode. Changes in the position of these is a suitable indicator of the overall effects of the HB network on the local potential around the proton. Whereas the analysis of INS data needs to rely on an underlying physical model, DINS can be used to probe the overall dependence of $\langle E_K \rangle$ on physical parameters like temperature or pressure, thereby providing stringent benchmarks for detailed theoretical studies. Recent work on amorphous ices has developed a means of quantifying the anharmonicity of atomic motions via the joint use of INS and DINS [143]. On a more applied front, the isobaric data shown around the liquid-to-supercritical phase transition in Fig. 33 are of direct relevance to the further development of nuclear power reactors, where computer models of the neutronic and thermodynamic response of water over a wide range of physical conditions still require detailed validation against experimental data. This line of work has been extended to simultaneous MANSE and transmission measurements on water mixtures, with a view to obtaining total scattering cross sections over a wide energy range, as well as nuclear effective temperatures for H, D, and O [237, 238]. In spite of its apparent simplicity as a light triatomic system, the study of water and aqueous systems continues apace on many exciting (and oftentimes unforeseen) fronts.

Further developments in the requisite instrumentation lie at the heart of further progress in the discipline. At this point in time, the overall detected flux on an instrument like VESUVIO constitutes the main limitation of eV neutron spectroscopy, as well as the primary reason as to why the technique has not been fully exploited to date. Much could still be done to move beyond the current status quo. From the lessons learnt thus far, a next-generation eV neutron spectrometer ought to combine as many different techniques using thermal and epithermal neutrons as possible. Section 2.3.1 presented a number of

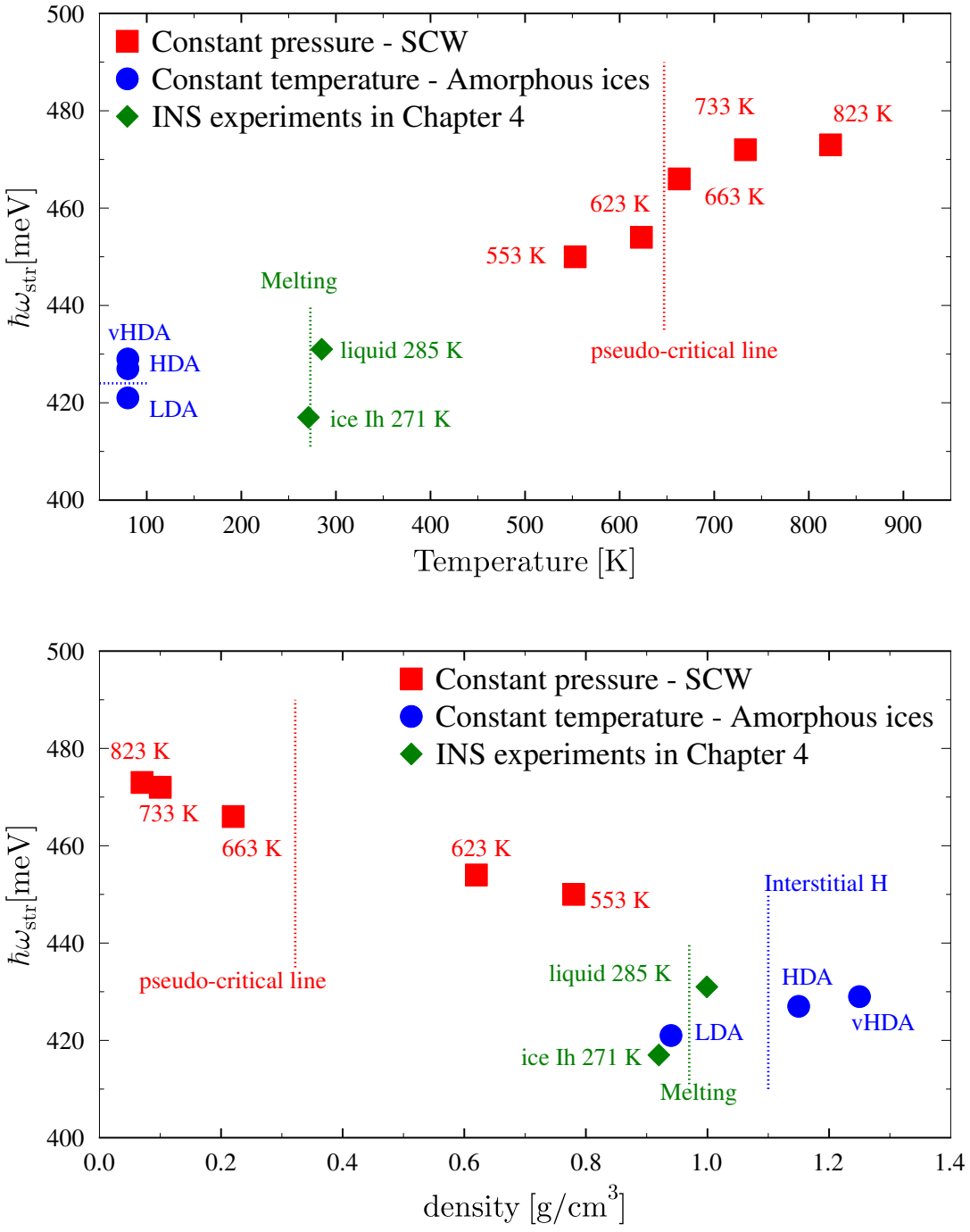

Figure 33. Vibrational energies associated with the OH-stretch mode in water as a function of temperature (top) and density (bottom). Different symbols and colours represent different phases: SCW at constant pressure (red squares); amorphous ices at a constant temperature of 80 K (blue circles) [143]; and liquid water and ice across melting (green diamonds) [62]. Vertical dotted lines denote the presence of structural changes or phase transitions. Reproduced from Ref. [63].

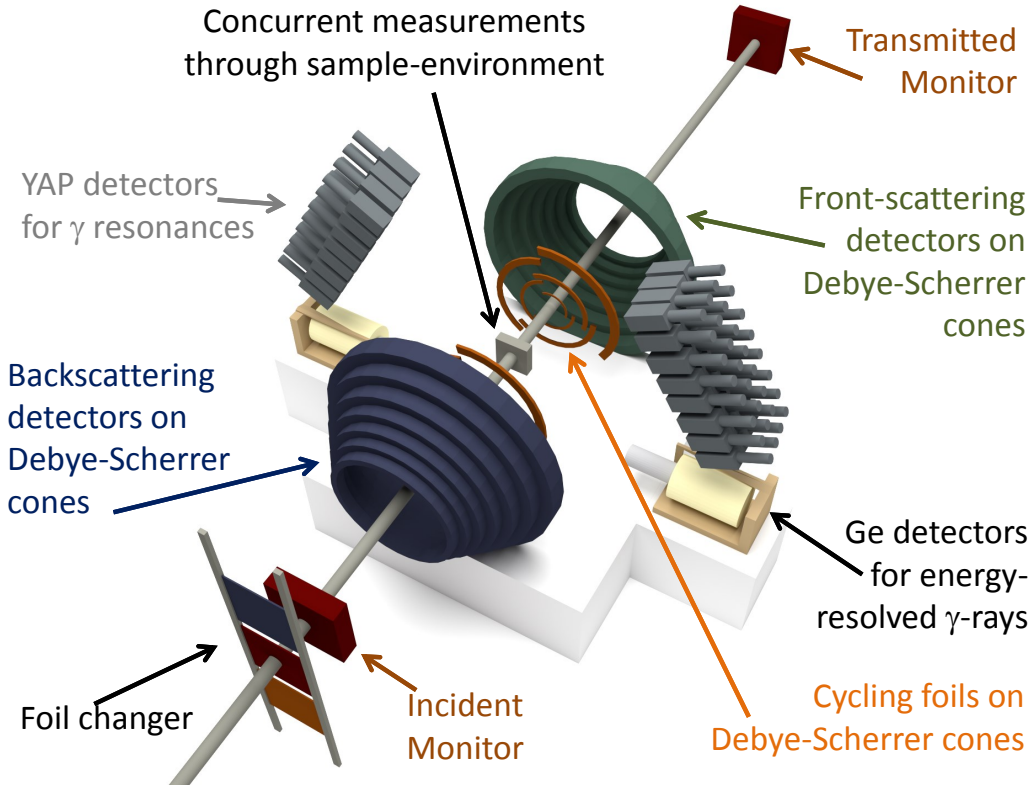

Figure 34. Schematic diagram of a next-generation eV neutron spectrometer. Front and backscattering detector banks are positioned along Debye-Scherrer cones. YAP detectors normal to the beam direction are used for the analysis of γ-rays from the resonant capture of eV neutrons. The Ge detectors immediately below these can be used for energy-resolved γ-ray analysis such as PGAA. A multiple-stage foil-changer in the incident beam is used to effect further energy selection. The black arrow above the sample indicates the possibility of utilising other experimental probes *in situ*. See also discussion in the main text.

ongoing developments in this direction, some of which can already be used on a routine basis along with DINS, *e.g.,* diffraction and transmission. The body of work reviewed herein provides solid ground for the further development of a fully fledged experimental station for *Epithermal and Thermal Neutron Analysis*, hereafter denoted as ETNA. Figure 34 offers some thoughts on what ETNA might look like in the foreseeable future to tackle and move beyond the scientific drivers and challenges presented throughout this review. A much-needed improvement involves significant changes to the geometry and detector coverage of forward and backscattering banks for recoil scattering and diffraction, as these could be chosen to follow the natural symmetry of a neutron-scattering experiment along Debye-Scherrer cones. This second-generation detector array would represent a step-change relative to the current set-up, including the implementation of multiplexing techniques via the use multiple resonant foils to enhance count rates even further. In this situation, energy selection of incident neutrons could be implemented either over a range of energies (*e.g.*, to suppress the thermal region) or at specific incident energies in order to discriminate between purely elastic and inelastic events, or to enhance mass selectivity and element specificity. As shown in the figure, this detector geometry for recoil scattering is also relatively open, thereby allowing for the presence of additional detector banks orthogonal to the neutron beam. The YAP-detector technology developed for VESUVIO and described in Section 2.3.1 could be then used in this configuration to perform elemental analysis and MANSE of much-heavier atomic species

using neutron-capture resonances at eV energies. Also, novel Ge-based detectors [241] in a similar geometry as the aforementioned YAP banks would enable the implementation of prompt-γ emission techniques for non-destructive elemental analysis across the periodic table. These techniques include Prompt-Gamma Activation Analysis (PGAA), extensively used at nuclear reactors [239]. Their use at short-pulse spallation neutron sources has been recently explored with success in Ref. [240]. These developments would increase the information content of a given experiment by at least two orders of magnitude relative to current figures. These enhancements can easily arise from improvements in both the primary (source strength, optimisation of incident pulse widths), as well as the secondary spectrometer (wider detector coverage using smaller detector elements, as well as the implementation of additional background-suppression strategies). Furthermore, such an increase in both capacity and capability could always be complemented via the use of additional *in situ* techniques. Raman spectroscopy is a natural choice to go along DINS and MANSE, and its merits have already been demonstrated for thermal and cold neutrons [242]. Further order-of-magnitude increases in flux can always come from improvements to the neutron source per se, *i.e.,* last-generation short-pulse spallation sources like SNS [113] at Oak Ridge National Laboratory (USA), or MLF [243] at J-PARC in Japan. The addition of an ETNA-like instrument to these facilities would certainly be a timely addition to existing capabilities in the global landscape to meet increasing demand. Likewise, a careful optimisation of target-moderator-reflector geometries to maximise the flux and temporal characteristics of epithermal neutrons could also offer additional and significant gains. The epithermal flux available on the CHIPIR irradiation beamline at ISIS [34, 244] represents a good example of what judicious neutronics-design efforts can achieve at a reasonable cost relative to major facility upgrades. Taking into account all of these factors, ETNA would provide a quantum leap in both capacity and capability, thereby transforming in a fundamental way how epithermal neutrons from short-pulse spallation sources could be exploited to the full of their potential in the years to come. As such, the future of the discipline looks brighter than ever.

Acknowledgments

We thank the two anonymous referees for their insightful comments on the original version of the manuscript. Our heartfelt gratitude also goes to a growing and vibrant community across the globe driving the field of eV neutron spectroscopy forward into the future, with exciting applications across science and engineering, new and imaginative technical developments, and advances in the theoretical foundations and associated computational tools underpinning a robust description of the quantum behaviour of the materials world around us. In particular, we thank the following people for engaging with us in many stimulating discussions and joint ventures using eV neutrons over the years: M.A. Adams, A. Arbe, J. Armstrong, E. Artacho, F. Barroso-Bujans, S.M. Bennington, F.J. Bermejo, L. Bernasconi, J.J. Blostein, D.T. Bowron, J. Boxall, A. Bracco, F. Bresme, F. Bruni, C. Cabrillo, F. Cacialli, R. Car, S.C. Capelli, J.M. Carpenter, C.R.A. Catlow, M. Ceriotti, S. Cerveny, G.A. Chass, P. Collier, J. Colmenero, D. Colognesi, R.A. Cowley, G.J. Cuello, A. D'Angelo, J. Dawidowski, S.O. Diallo, J.C. Dore, M.T. Dove, K. Drużbicki, P.P. Edwards, G. Festa, R. Fernández-Perea, F. Fillaux, A.D. Fortes, V. Garbuio, N.I. Gidopoulos, M. Gigg, H.R. Glyde, M.A. González, G. Gorini, J.R. Granada, G.N. Greaves, J.M.F. Gunn, M.J. Gutmann, A.J. Horsewill, C.A. Howard, S. Imberti, A. Ivanov, S. Jackson, M.R. Johnson, M. Karlsson, G.J. Kearley, A.I. Kolesnikov, A. Liscio, F. Liscio, C.-K. Loong, S.W. Lovesey, D.T. Major, F. Mallamace, D.E. Manolopoulos, J. Mayers,

K.A. McEwen, R.L. McGreevy, D. McPhail, A. Michaelides, S. Moorby, R. Moreh, J.A. Morrone, S. Mukhopadhyay, R.J. Nelmes, R.J. Newport, D. Nixon, J. Norris, C. Offer, E. Oram, E. Pace, V. Palermo, L.C. Pardo, S.F. Parker, M. Parrinello, E. Perelli Cippo, R.J.-M. Pellenq, A. Pietropaolo, D. Pooley, D.L. Price, D. Raspino, K. Refson, G.F. Reiter, N.J. Rhodes, M.A. Ricci, L.A. Rodríguez Palomino, S. Rudić, M.-L. Saboungi, C.G. Salzmann, A. Sartbaeva, E.M. Schooneveld, A.G. Seel, J. Silvestre-Albero, N.T. Skipper, G.P. Škoro, A.K. Soper, U.E. Steigenberger, W.G. Stirling, C. Stock, J.-Ll. Tamarit, M. Tardocchi, K.V. Tian, J.-C. Tan, A.D. Taylor, J. Tomkinson, P.D. Vaz, K.T. Wikfeltd, C.G. Windsor, I.G. Wood, and M. Zoppi.

Funding

The authors gratefully acknowledge the UK Science & Technology Facilities Council (STFC) for financial support, access to beam time at the ISIS Pulsed Neutron and Muon Source, and use of the e-Science SCARF Supercomputing Facility at the Rutherford Appleton Laboratory. This work has been partially supported within the framework of past and present (2014-2020) agreements between the CNR and the STFC for collaborative research between Italy and ISIS.

List of acronyms in alphabetical order

DFPT density functional perturbation theory
DFT density functional theory
DINS deep inelastic neutron scattering
DD double difference
FC foil cycling
FSE final-state effects
GIC graphite intercalation compound
GO graphite oxide
HB hydrogen bonding
IA impulse approximation
INS inelastic neutron scattering
MANSE mass-resolved neutron spectroscopy
NCS neutron Compton scattering
NCP neutron Compton profile
NMD nuclear momentum distribution
NQE nuclear quantum effect
PGAA prompt-gamma activation analysis
PI path-integral
PIMD path-integral molecular dynamics
PVDOS partial vibrational density of states
PW-DFT plane-wave density functional theory
QE quantum-energy excess
QENS quasielastic neutron scattering
RD resonance detector
RF resonance filter
SD single difference

SCW supercritical water
SW supercooled water
TOF time of flight
VDOS vibrational density of states
YAP ittrium aluminium perovskite ZPE zero-point energy
1BZ first Brillouin zone
3D-HO three-dimensional harmonic oscillator

References

[1] C. Andreani, D. Colognesi, J. Mayers, G. F. Reiter, and R. Senesi, *Adv. Phys.* **54** 377 (2005).
[2] F. Fernandez-Alonso and D.L. Price (eds), *Neutron Scattering – Fundamentals* (Academic Press, New York, 2013).
[3] F. Fernandez-Alonso and D.L. Price (eds), *Neutron Scattering – Magnetic and Quantum Phenomena* (Academic Press, New York, 2015).
[4] Url: http://www.isis.stfc.ac.uk (Last accessed 30 March 2017).
[5] R.N. Silver (ed), *Proceedings of the 1984 Workshop on High Energy Excitations in Condensed Matter* (Los Alamos National Laboratory, 1984). Url: http://www.osti.gov/scitech/servlets/purl/5858602 (Last accessed 30 March 2017).
[6] P. C. Hohenberg and P. M. Platzmann, *Phys. Rev.* **152** 198 (1966); P.M. Platzmann and N. Tzoar, in B. Williams (ed), *Compton Scattering* (McGraw Hill, New York, 1977).
[7] V. I. Gol'danskii, *Soviet Phys. JETP* **4** 604 (1957).
[8] G.K. Ivanov and Yu.S. Sayasov, *Usp. Fiz. Nauk.,* **90** 47 (1966); *Soviet Phys. Uspekhi* **9** 670 (1967).
[9] J.M.F. Gunn, C. Andreani and J. Mayers, *J. Phys. C: Solid State Phys.* **19** L835 (1986).
[10] J. Mayers, A.C. Evans, D.L. Timms, and M.J. Cooper, *Z. Nat.* **48A** 425 (1993).
[11] Url: http://www.isis.stfc.ac.uk/instruments/vesuvio/ (Last accessed 30 March 2017).
[12] C. Andreani, A. Pietropaolo, R. Senesi, G. Gorini, M. Tardocchi, A. Bracco, N. Rhodes, E. Schooneveld, *Nucl. Instrum. Meth. A* **481** 509 (2002).
[13] A. Pietropaolo, C. Andreani, A. DAngelo, R. Senesi, G. Gorini, S. Imberti, M. Tardocchi, N. Rhodes, and E.M. Schooneveld, *Appl Phys. A* **74** s189 (2002).
[14] M. Tardocchi, A. Pietropaolo, C. Andreani, A. Bracco, A. D'Angelo, G. Gorini, S. Imberti, R. Senesi, N.J. Rhodes, and E.M. Schooneveld, *Nucl. Instrum. Meth. A* **526** 477 (2004).
[15] C. Andreani, A. DAngelo, G. Gorini, S. Imberti, A. Pietropaolo, N.J. Rhodes, E.M. Schooneveld, R. Senesi, and M. Tardocchi, *Appl. Phys. A* **78** 903 (2004).
[16] G. Gorini, E. Perelli-Cippo, M. Tardocchi, C. Andreani, A. DAngelo, A. Pietropaolo, R. Senesi, S. Imberti, A. Bracco, E. Previtali, G. Pessina, N.J. Rhodes, and E.M. Schooneveld, *Nucl. Instrum. Meth. A* **529** 293 (2004).
[17] S. Imberti, C. Andreani, V. Garbuio, G. Gorini, A. Pietropaolo, R. Senesi, and M. Tardocchi, *Nucl. Instrum. Meth. A* **552** 463 (2005).
[18] E.M. Schooneveld, J. Mayers, N.J. Rhodes, A. Pietropaolo, C. Andreani, R. Senesi, G. Gorini, E. Perelli Cippo, and M. Tardocchi, *Rev. Sci. Instrum.* **77** 095103 (2006).
[19] A. Pietropaolo, C. Andreani, A. Filabozzi, R. Senesi, G. Gorini, E. Perelli Cippo, M. Tardocchi, N.J. Rhodes, and E.M. Schooneveld, *J. Instrum.* **1** P04001 (2006).
[20] A. Pietropaolo, C. Andreani, A. Filabozzi, E. Pace, and R. Senesi, *Nucl. Instrum. Meth. A* **570** 498 (2007).

[21] A. Pietropaolo, C. Andreani, M. Rebai, L. Giacomelli, G. Gorini, E.P. Cippo, T. Tardocchi, A. Fazzi, G. Verona Rinati, M. Marinelli, E. Milani, C.D. Frost, and E.M. Schooneveld, *Europhys. Lett.* **92** 68003 (2010).
[22] A. Pietropaolo and R. Senesi, *Phys. Rep.* **508** 45 (2011).
[23] A. Pietropaolo, C. Andreani, M. Rebai, L. Giacomelli, G. Gorini, E. Perelli Cippo, M. Tardocchi, A. Fazzi, G. Verona Rinati, C. Verona, M. Marinelli, E. Milani, C. D. Frost, and E. M. Schooneveld, *Europhys. Lett.* **94** 62001 (2011).
[24] M. Rebai, C. Andreani, A. Fazzi, C.D. Frost, L. Giacomelli, G. Gorini, E. Milani, E. Perelli Cippo, A. Pietropaolo, G. Prestopino, E. Schooneveld, M. Tardocchi, C. Verona, and G. Verona Rinati, *Nucl. Phys. B* **215** 313 (2011).
[25] M. Rebai, L. Giacomelli, C. Andreani, A. Fazzi, C.D. Frost, E. Perelli Cippo, A. Pietropaolo, N. Rhodes, M. Tardocchi, E. Schooneveldd, and G. Gorini, it J. Instrum. **7** C05015 (2012).
[26] S. Gerardin, M. Bagatin, A. Ferrario, A. Paccagnella, A. Visconti, S. Beltrami, C. Andreani, G. Gorini, and C. D. Frost, *IEEE T. Device Mat. Re.* **12** 437 (2012).
[27] A. Miceli, G. Festa, R. Senesi, G. Gorini, and C. Andreani, *J. Phys. Conf. Ser.* **470** 012001 (2013).
[28] E. M. Schooneveld, A. Pietropaolo, C. Andreani, E. Perelli Cippo, N.J. Rhodes, R. Senesi, M. Tardocchi, and G. Gorini, *Rep. Progr. Phys.* **79** 094301 (2016).
[29] R. Senesi, C. Andreani, Z. Bowden, D. Colognesi, E. Degiorgi, A.L. Fielding, J. Mayers, M. Nardone, J. Norris, M. Praitano, N.J. Rhodes, W.G. Stirling, J. Tomkinson and C. Uden, *Physica B* **276-278** S189 (2000).
[30] J. Mayers, J. Tomkinson, T. Abdul-Redah, W. G. Stirling, C. Andreani, R. Senesi, M. Nardone, D. Colognesi, and E. Degiorgi, *Physica B* **350** 659 (2004).
[31] J. Mayers and G. Reiter, *Meas. Sci. Technol.* **23** 045902 (2012).
[32] A.G. Seel, M. Krzystyniak, and F. Fernandez-Alonso, *J. Phys. Conf. Ser.* **571** 012006 (2014).
[33] G. Gorini, for the Ancient Charm collaboration, *Il Nuovo Cimento C*, **30** 47 (2007).
[34] C. Andreani, A. Pietropaolo, A. Salsano, G. Gorini, M. Tardocchi, A. Paccagnella, S. Gerardin, C.D. Frost, S. Ansell and S. P. Platt, *Appl. Phys. Lett.* **92** 114101 (2008).
[35] A.G. Seel, R. Senesi, and F. Fernandez-Alonso, *J. Phys. Conf. Ser.* **571** 011001 (2014).
[36] G. Romanelli, M. Ceriotti, D. E. Manolopoulos, C. Pantalei, R. Senesi, and C. Andreani, *J. Phys. Chem. Lett.* **508** 3251 (2013).
[37] D. A. J. Rand and R. M. Dell, *Hydrogen Energy: Challenges and Prospects* (RSC Publishing, Cambridge, 2008).
[38] D. Mori and K. Hirose, *Int. J. Hydrogen Energ.* **34** 4569 (2009).
[39] A. Kudo and Y. Miseki, *Chem. Soc. Rev.* **38** 253 (2009).
[40] G. Ertl, H. Knözinger, F. Schüth and J. Weitkamp, *Handbook of Heterogeneous Catalysis* (Wiley-VCH, Weinheim, 2008).
[41] G. Herzberg, *Molecular Spectra and Molecular Structure* (Krieger Publishing Co., Malabar 1989).
[42] F. Fernandez-Alonso, B. D. Bean, J. D. Ayers, A. E. Pomerantz and R. N. Zare, *Z. Phys. Chem. (Munich)* **214** 1167 (2000).
[43] W.H. Miller, *Proc. Natl. Acad. Sci. U.S.A.* **102** 6660 (2005).
[44] L. Lin, J.A. Morrone, R. Car and M. Parrinello, *Phys. Rev. Lett.* **105** 110602 (2010).
[45] M. Ceriotti and D. E. Manolopoulos, *Phys. Rev. Lett.* **109** 100604 (2012).
[46] K.T. Wikfeldt, *J. Phys. Conf. Ser.* **571** 011012 (2014).
[47] M. Ceriotti, *J. Phys. Conf. Ser.* **571** 011011 (2014).
[48] C. G. Windsor, *Pulsed Neutron Scattering* (Taylor and Francis, London, 1981)
[49] S. W. Lovesey, *Theory of Neutron Scattering from Condensed Matter* (Oxford University Press, Oxford, 1987).

[50] G. F. Reiter and R. Silver, *Phys. Rev. Lett.* **54** 1047 (1985).
[51] G. Watson, *J. Phys.: Condens. Matter* **8** 5955 (1996).
[52] G.B. West, *Phys. Rev. C* **18** 263 (1975).
[53] J. Mayers, C. Andreani, and G. Baciocco, *Phys. Rev. B* **39** 2022 (1989).
[54] V.F. Sears, *Phys. Rev. B* **30** 44 (1984).
[55] G. F. Reiter, J. Mayers, and J. Noreland, *Phys. Rev. B* **65** 104305 (2002).
[56] D. Colognesi, A. Pietropaolo, R. Senesi, and A.J. Ramirez-Cuesta, *Phys. Rev. B* **76** 174206 (2007).
[57] R. Senesi, D. Colognesi, A. Pietropaolo, and T. Abdul-Redah, *Phys. Rev. B* **72** 054119 (2005).
[58] C. Andreani, E. Degiorgi, R. Senesi, F. Cilloco, D. Colognesi, J. Mayers, M. Nardone, and E. Pace, *J. Chem. Phys.* **114** 387 (2001).
[59] D. Flammini, A. Pietropaolo, R. Senesi, C. Andreani, F. McBride, A. Hodgson, M. Adams, L. Lin, and R. Car, *J. Chem. Phys.* **136** 024504 (2012).
[60] L. Lin, J.A. Morrone, R. Car and M. Parrinello, *Phys. Rev. B* **83** 220302 (2011).
[61] M. Ceriotti, G. Miceli, A. Pietropaolo, D. Colognesi, A. Nale, M. Catti, M. Bernasconi, and M. Parrinello, *Phys. Rev. B* **82** 174306 (2010).
[62] C. Andreani, G. Romanelli, and R. Senesi, *Chem. Phys.* **427** 106 (2013).
[63] G. Romanelli, *Ph.D. Thesis*, Università degli Study di Roma – Tor Vergata, Italy (2015).
[64] G. Romanelli, F. Fernandez-Alonso, and C. Andreani, *J. Phys. Conf. Ser.* **571** 012003 (2014).
[65] R. Senesi, *Nucl. Instrum. Meth. A* **661** 70 (2012).
[66] R. Senesi, D. Flammini, G. Romanelli, and C. Andreani, *Nucl. Instrum. Meth. A* **704** 36 (2013).
[67] D. Homouz, G. Reiter, J. Eckert, J. Mayers, and R. Blinc, *Phys. Rev. Lett.* **98** 115502 (2007).
[68] K. Huang, *Statistical Mechanics* (John Wiley, New York, 1987).
[69] A.A. Maradudin, E.W. Montroll, G.I. Weiss, and I.P. Ipatova, *Theory of Lattice Dynamics in the Harmonic Approximation* (Academic Press, New York, 1971).
[70] M. Warner, S.W. Lovesey, and J. Smith, *Z. Phys.* **B51** 109 (1983).
[71] B. Militzer and E.L. Pollock, *Phys. Rev. Lett.* **89** 280401 (2002).
[72] E. Wigner, *Phys. Rev.* **40** 749 (1932).
[73] W.C. Kerr and K.S. Singwi, *Phys. Rev. A* **7** 1043 (1973).
[74] T.L. Beck, in Ch. Chipot and A. Pohorille (eds), *Free Energy Calculations – Theory and Applications in Chemistry and Biology* (Springer-Verlag, Berlin, 2007) pp. 387-420.
[75] C.P. Herrero and R. Ramirez, *J. Chem. Phys.* **134** 094510 (2011).
[76] R.N. Silver and P.E. Sokol (eds) *Momentum Distributions* (Plenum Press, New York, 1989).
[77] S. Baroni, S. de Gironcoli, A. dal Corso, and P. Giannozzi, *Rev. Mod. Phys.* **73** 515 (2001).
[78] M. Krzystyniak and F. Fernandez-Alonso, *Phys. Rev. B* **83** 134305 (2011).
[79] M.T. Dove, *Introduction to Lattice Dynamics* (Cambridge University Press, Cambridge, 1993).
[80] D. Colognesi, E. Degiorgi, and E. Pace, *Physica B* **293** 317 (2001).
[81] M. Krzystyniak, *J. Chem. Phys.* **133** 144505 (2010).
[82] J. Boronat, C. Cazorla, D. Colognesi, and M. Zoppi, *Phys. Rev. B* **69** 174302 (2004).
[83] V.F. Sears, *Phys. Rev. A* **7** 340 (1973).
[84] J. Mayers and T. Abdul-Redah, *J. Phys.: Condens. Matter* **16** 4811 (2004).
[85] V.G. Plekhanov, *Mater. Sci. Eng. R* **35** 139 (2001).
[86] J.P. Perdew, K. Burke, and M. Ernzerhof, *Phys. Rev. Lett.* **77** 3865 (1996).
[87] T. Abdul-Redah, P.A. Georgiev, M. Krzystyniak, D.K. Ross, and C.A.

Chatzidimitriou-Dreismann, *Physica B* **385-386** 57 (2006).
[88] D. Colognesi, A.J. Ramirez-Cuesta, M. Zoppi, R. Senesi, and T. Abdul-Redah, *Physica B* **350** E983 (2004).
[89] S.F. Parker, F. Fernandez-Alonso, A.J. Ramirez-Cuesta, J. Tomkinson, S. Rudić, R.S. Pinna, G. Gorini, and J. Fernández Castañon, *J. Phys. Conf. Ser.* **554** 012003 (2014).
[90] B. Fultz, *Prog. Mater. Sci.* **55** 257 (2010).
[91] S. Mukhopadhyay, M. Gutmann, and F. Fernandez-Alonso, *Phys. Chem. Chem. Phys.* **16** 26234 (2014).
[92] M. Krzystyniak, K. Drużbicki, and F. Fernandez-Alonso, *Phys. Chem. Chem. Phys.* **17** 31287 (2015).
[93] S.M. Haile, D.A. Boysen, C.R.I Chrisholm, and R.B. Merle, *Nature* **410** 910 (2001).
[94] J.J. Rehr and R.C. Albers, *Rev. Mod. Phys.* **72** 621 (2000).
[95] M. Krzystyniak, K. Drużbicki, G. Romanelli, M.J. Gutmann, S. Rudić, S. Imberti, and F. Fernandez-Alonso *Phys. Chem. Chem. Phys.* **19** 9064 (2017).
[96] Url: http://www.isis.stfc.ac.uk/instruments/tosca/ins-database (Last accessed 30 March 2017).
[97] D.R. Bowler and T. Miyazaki, *Rep. Prog. Phys.* **75** 036503 (2012).
[98] F.J. Bermejo, F.J. Mompeán, A. Srinivasan, J. Mayers, and A.C. Evans, *Phys. Lett. A* **189** 333 (1994).
[99] J. Dawidowski, F.J. Bermejo, L. Fernández Barquín, P. Gorria, J.M. Barandiarán, A.C. Evans, and J. Mayers, *Phys. Lett. A* **214** 59 (1996).
[100] Y. Feng, C. Ancona-Torres, T.F. Rosenbaum, G.F. Reiter, D.L. Price, and E. Courtens, *Phys. Rev. Lett.* **97** 145501 (2006).
[101] A.G. Seel, A. Sartbaeva, J. Mayers, A.J. Ramirez-Cuesta, and P. P. Edwards, *J. Chem. Phys* **134** 114511 (2011).
[102] A.G. Seel, E. Zurek, A.J. Ramirez-Cuesta, K.R. Ryan, M.T.J Lodge, and P.P. Edwards, *Chem. Commun.* **50** 10778 (2014).
[103] M. Ceriotti, W. Fang, P.G. Kusalik, R.H. McKenzie, A. Michaelides, M.A. Morales, and T.E. Markland, *Chem. Rev.* **116** 7529 (2016).
[104] B.J. Berne and D. Thirumalai, *Annu. Rev. Phys. Chem.* **37** 401 (1986).
[105] M. Ceriotti and T.E. Markland, *J. Chem. Phys.* **138** 014112 (2013).
[106] M. Ceriotti, J. More, and D.E. Manolopoulos, *Comput. Phys. Commun.* **185** 1019 (2014).
[107] D.M. Ceperley, *Rev. Mod. Phys.* **67** 279 (1995).
[108] S. Habershon, D.E. Manolopoulos, T.E. Markland, and T.F. Miller III, *Annu. Rev. Phys. Chem.* **64** 387 (2013).
[109] J.R. Granada, R.E. Mayer, J. Dawidowski, J.R. Santisteban, F. Cantargi, J.J. Blostein, L.A. Rodríguez Palomino, and A. Tartaglione, *Eur. Phys. J. Plus* **131** 216 (2016).
[110] L.A. Rodríguez Palomino, J.J. Blostein, and J. Dawidowski, *J. Instrum.* **8** P08016 (2013).
[111] L.A. Rodríguez Palomino, J.J. Blostein, and J. Dawidowski, *Nucl. Instrum. Meth. A* **646** 142 (2011).
[112] Url: http://csns.ihep.ac.cn (Last accessed 30 March 2017).
[113] Url: http://www.sns.gov (Last accessed 30 March 2017).
[114] C. Andreani, G. Gorini, E. Perelli-Cippo, A. Pietropaolo, N. Rhodes, E. M. Schooneveld, R. Senesi, and M. Tardocchi, *Appl. Phys. Lett.* **85** 5454 (2004).
[115] M. Tardocchi, A. Pietropaolo, R. Senesi, C. Andreani, and G. Gorini, *Nucl. Instr. Meth. A* **518** 259 (2004).
[116] M. Tardocchi, A. Pietropaolo, C. Andreani, G. Gorini, N. Rhodes, E. M. Schooneveld, and R. Senesi, *Rev. Sci. Instr.* **75** 4880 (2004).
[117] S. Ikeda and N. Watanabe, *Phys. Lett. A* **121** 34 (1987).
[118] G. Gorini, G. Festa, and C. Andreani, *J. Phys. Conf. Ser.* **571** 012005 (2014).

[119] A.C. Evans, J. Mayers, D.N. Timms, and M.J. Cooper, *Z. Naturforsch A: Phys. Sci.* **48** 425 (1993).
[120] R.J. Newport, M.P. Paoli, V.T. Pugh, R.N. Sinclair, A.D. Taylor, and W.G. Williams, *Proceedings of the Eighth Meeting of the International Collaboration on Advanced Neutron Sources* (ICANS VIII), *Rutherford Appleton Laboratory Report No. RAL-TR-85-110* (Chilton, 1985), p. 562.
[121] R. Senesi, A.I. Kolesnikov, and C. Andreani, *J. Phys. Conf. Ser.* **571** 012007 (2014).
[122] P.A. Seeger, A.D. Taylor, and R.M. Brugger, *Nucl. Instr. Meth. A* **240** 98 (1985).
[123] C. Andreani, D. Colognesi, E. Degiorgi, A. Filabozzi, M. Nardone, E. Pace, A. Pietropaolo, and R. Senesi, *Nucl. Instr. Meth. A* **497** 535 (2003).
[124] J. Mayers and M.A. Adams, *Nucl. Instrum. Meth. A* **625** 47 (2011).
[125] A. Filabozzi, E. Pace, and A. Pietropaolo, *Nucl. Instrum. Meth. A* **673** 1 (2012).
[126] M. Krzystyniak, M.A. Adams, A. Lovell, N.T. Skipper, S. M. Bennington, J. Mayers, and F. Fernandez-Alonso, *Faraday Discuss.* **151** 171 (2011).
[127] D.N. Timms, A.C. Evans, M. Boninsegni, D.M. Ceperley, J. Mayers, and R.O. Simmons, *J. Phys.: Condens. Matter* **8** 6665 (1996).
[128] A.C. Evans, J. Mayers, and D.N. Timms, *J. Phys.: Condens. Matter* **6** 4197 (1994).
[129] P. Schillebeeckx, A. Borella, F. Emiliani, G. Gorini, W. Kockelmann, S. Kopecky, C. Lampoudis, M. Moxon, E. Perelli Cippo, H. Potsma, N.J. Rhodes, E.M. Schooneveld, and C. Van Beveren, *J. Instrum.* **3** C03009 (2012).
[130] H.J. Stone, M.G. Tucker, Y. Le Godec, F.M. Méducin, E.R. Cope, S.A. Hayward, G.P.J. Ferlat, W.G. Marshall, S. Manolopoulos, S.A.T. Redfern, and M.T. Dove, *Nucl. Instrum. Meth. A* **547** 601 (2005).
[131] S. Jackson, M. Krzystyniak, A.G. Seel, M. Gigg, S.E. Richards, and F. Fernandez-Alonso, *J. Phys. Conf. Ser.* **571** 012009 (2014).
[132] D. Monserrat, A. Vispa, L.C. Pardo, R. Tolchenov, S. Mukhopadhyay, and F. Fernandez-Alonso, *J. Phys. Conf. Ser.* **663** 012009 (2015).
[133] D. Nixon, *M.Sc. Thesis*, Newcastle University, United Kingdom (2016).
[134] G. Romanelli and M. Krzystyniak, *Nucl. Instrum. Meth. A* **819**, 84 (2016).
[135] A. G. Seel, M. Ceriotti, and P.P. Edwards, *J. Phys.: Condens. Matter* **24** 365401 (2012).
[136] M. Krzystyniak, S.E. Richards, A.G. Seel, and F. Fernandez-Alonso, *Phys. Rev. B* **88** 184304 (2013).
[137] M. Krzystyniak, A.G. Seel, S.E. Richards, M.J. Gutmann, and F. Fernandez-Alonso, *J. Phys. Conf. Ser.* **571** 012009 (2014).
[138] A.G. Seel, M. Krzystyniak, R. Senesi, and F. Fernandez-Alonso, *J. Phys. Conf. Ser.* **571** 012014 (2014).
[139] L. Fu, S. Villette, S. Petoud, F. Fernandez-Alonso, and M.-L. Saboungi, *J. Phys. Chem. B* **115** 1881 (2011).
[140] D.L. Price, L. Fu, F.J. Bermejo, F. Fernandez-Alonso, and M.-L. Saboungi, *Chem. Phys.* **424** 62 (2013).
[141] R. Senesi, D. Flammini, A. I. Kolesnikov, E. Murray, G. Galli, and C. Andreani, *J. Chem. Phys.* **139** 074504 (2013).
[142] S. Habershon, T. E. Markland, and D. E. Manolopoulos, *Chem. Phys.* **131** 24501 (2019).
[143] A. Parmentier, J.J. Shephard, G. Romanelli, R. Senesi, C.G. Salzmann and C. Andreani, *J. Phys. Chem. Lett.* **6** 2038 (2015).
[144] C. Andreani, G. Romanelli, and R. Senesi, *J. Phys. Chem. Lett.* **7** 2216 (2016).
[145] Y. Finkelstein and R. Moreh, *Chem. Phys.* **431** 58 (2014).
[146] B. Cheng, J. Behler, and M. Ceriotti, 7 (12), pp 22102215 *J. Phys. Chem. Lett.* **7** 2210 (2016).
[147] A.J. Byrd, K.K. Pant, and R.B. Gupta, *Ind. and Eng. Chem. Res.* **42** 3574 (2007).
[148] A. Cabanas, J. Li, P. Blood, T. Chudoba, W. Lojkowski, M. Poliakoff, and E.

Lester, *J. Supercrit. Fluids* **40** 284 (2007).
[149] Y. Oka, *et al.*, *Super Light Water Reactors and Super Fast Reactors* (Springer, Berlin, 2010).
[150] Zhen Fang, *Rapid production of Micro- and Nano-particles using Supercritical Water* (Springer, Berlin, 2010).
[151] C. Pantalei, A. Pietropaolo, R. Senesi, S. Imberti, C. Andreani, J. Mayers, C. Burnham, and G. Reiter, *Phys. Rev. Lett.* **100** 177801 (2008).
[152] C.J. Burnham, G.F. Reiter, J. Mayers, T. Abdul-Redah, H. Reichert, and H. Dosch, *Phys. Chem. Chem. Phys.* **8** 3966 (2006).
[153] A. Pietropaolo, R. Senesi, C. Andreani, and J. Mayers, *Braz. J. Phys.* **39** 318 (2009), and references therein.
[154] R. Senesi, G. Romanelli, M.A. Adams, and C. Andreani, *Chem. Phys.* **427** 111 (2013).
[155] R. Moreh and D. Nemirovsky, *J. Chem. Phys.* **133** 084506 (2010).
[156] A.K. Soper and C.J. Benmore, *Phys. Rev. Lett.* **101** 065502 (2008).
[157] C.J. Burnham, T. Hayashi, R.L. Napoleon, T. Keyes, S. Mukamel, and G.F. Reiter, *J. Chem. Phys.* **135** 144502 (2011).
[158] A.K. Soper, *J. Phys. Chem. B* **115** 14014 (2011).
[159] A.K. Soper, *Chem. Phys.* **258** 121 (2000).
[160] X.Z. Li, B. Walker, and A. Michaelides, *Proc. Natl. Acad. Sci. USA* **108** 6369 (2011).
[161] T.E. Markland, and B.J. Berne, *Proc. Natl. Acad. Sci. USA* **109** 7988 (2012).
[162] J. Liu, R.S. Andino, C.M. Miller, X. Chen, D.M. Wilkins, M. Ceriotti, and D.E. Manolopoulos, *J. Phys. Chem. C* **117** 2944 (2013).
[163] S. Cerveny, F. Mallamace, J. Swenson, M. Vogel, and L. Xu, *Chem. Rev.* **116** 7608 (2016)
[164] C. Pantalei, R. Senesi, C. Andreani, P. Sozzani, A. Comotti, S. Bracco, M. Beretta, P.E. Sokol, and G. Reiter, *Phys. Chem. Chem. Phys.* **13** 6022 (2011).
[165] V. Garbuio, C. Andreani, S. Imberti, A. Pietropaolo, G.F. Reiter, R. Senesi, and M.A. Ricci, *J. Chem. Phys.* **127** 4501 (2007).
[166] B.C. Chakoumakos and G.V. Gibbs, *J. Phys. Chem.* **90** 996 (1986).
[167] P. Ugliengo, V. Saunders, and E. Garrone, *J. Phys. Chem.* **94** 2260 (1990).
[168] G.F. Reiter, A.I. Kolesnikov, S.J. Paddison, P.M. Platzman, A.P. Moravsky, M.A. Adams, and J. Mayers, *Phys. Rev. B* **85** 045403 (2012) and references therein.
[169] A.I. Kolesnikov, J.-M. Zanotti, C.-K. Loong, P. Thiyagarajan, A.P. Moravsky, R. O. Loutfy, and C.J. Burnham, *Phys. Rev. Lett.* **93** 035503 (2004).
[170] G. Reiter, C. Burnham, D. Homouz, P.M. Platzman, J. Mayers, T. Abdul-Redah, A.P. Moravsky, J.C. Li, C.-K. Loong, and A.I. Kolesnikov, *Phys. Rev. Lett.* **97** 247801 (2006).
[171] G.F. Reiter, A. Deb, Y. Sakurai, M. Itou, V.G. Krishnan, and S.J. Paddison, *Phys. Rev. Lett.* **11** 036803 (2013).
[172] G.F. Reiter, A. Deb, Y. Sakurai, M. Itou, and A.I. Kolesnikov, *J. Phys. Chem. Lett.* **7** 4433 (2016).
[173] A.I. Kolesnikov, G.F. Reiter, N. Choudhury, T.R. Prisk, E. Mamontov, A. Podlesnyak, G. Ehlers, A.G. Seel, D.J. Wesolowski, and L.M. Anovitz, *Phys. Rev. Lett.* **116** 167802 (2016).
[174] Y. Finkelstein, R. Moreh, S.L. Shang, Y. Wang, and Z.K. Liu, *J. Chem. Phys* **146** 124307 (2017).
[175] G. Romanelli, A. Liscio, R. Senesi, R. Zamboni, E. Treossi, F. Liscio, G. Giambastiani, V. Palermo, F. Fernandez-Alonso, and C. Andreani, *Carbon* **108** 199-203 (2016).
[176] G. Romanelli, R. Senesi, X. Zhang, K. Ping Loh, and C. Andreani, *Phys. Chem. Chem. Phys.* **17** 31680-31684 (2015).
[177] P. Ball, *The importance of water*, in I.W.M. Smith, C.S. Cockell, and S. Leach

(eds), *Astrochemistry and Astrobiology* (Springer, Berlin, 2013), p. 169.
[178] H. Engel, D. Doron, A. Kohen, and D.T. Major, *J. Chem. Theory Comp.* **8** 1223 (2012).
[179] H.D. Middendorf, U.N. Wanderlingh, R.L. Hayward, F. Albergamo, *Physica A* **304**, 266 (2002).
[180] R. Senesi, A. Pietropaolo, A. Bocedi, S.E. Pagnotta, and F. Bruni, *Phys. Rev. Lett.* **98** 138102 (2007).
[181] G.F. Reiter, R. Senesi, and J. Mayers *Phys. Rev. Lett.* **105** 148101 (2010).
[182] D. Nemirovski, R. Moreh, K.H. Andersen, and J. Mayers, *J. Phys.: Condens. Matter* **11** 6653 (1999).
[183] D. Nemirovski, R. Moreh, K. Kaneko, T. Ohba, and J. Mayers, *Surf. Sci.* **526** 282 (2003).
[184] C. Andreani, C. Pantalei, and R. Senesi, *Phys. Rev. B* **75** 064515 (2007).
[185] F. Fernandez-Alonso, F. J. Bermejo, and M.-L. Saboungi, in *Handbook of Nanophysics vol. 5* ed. K.D. Sattler (CRC Press, Boca Raton, 2010) pp. 129.
[186] A.J. Ramirez-Cuesta, M.O. Owen-Jones, and W.I.F. David, *Mater. Today* **12** 54 (2009).
[187] D.K. Ross, *Vacuum* **80** 1084 (2006).
[188] T. Enoki, M. Endo, and M. Suzuki, *Graphite Intercalation Compounds and Applications* (Oxford University Press, Oxford, 2003).
[189] A. Lovell, N.T. Skipper, S.M. Bennington, and R.I. Smith, *J. Alloy. Compd.* **446-447** 397 (2007).
[190] K. Watanabe, M. Soma, T. Onishi, and K. Tamaru, *Nature - Phys. Sci.* **233** 160 (1971).
[191] A.P. Smith, R. Benedek, F.R. Trouw, M. Minkoff, and L.H. Yang, *Phys. Rev. B* **53** 10187 (1996) and references therein.
[192] W.J. Stead, P. Meehan, and J.W. White, *J. Chem. Soc.: Faraday Trans. 2* **84** 1655 (1988).
[193] A. Lovell, F. Fernandez-Alonso, N.T. Skipper, K. Refson, S.M. Bennington, and S. F. Parker, *Phys. Rev. Lett.* **101** 126101 (2008).
[194] F. Fernandez-Alonso, F.J. Bermejo, C. Cabrillo, R.O. Loutfy, V. Leon, and M.L. Saboungi, *Phys. Rev. Lett.* **98** 077801 (2007).
[195] J.J. Purewal, J.B. Keith, C.C. Ahn, B. Fultz, C.M. Brown, and M. Tyagi, *Phys. Rev. B* 79 05435 (2009).
[196] G. Romanelli, M. Krzystyniak, R. Senesi, D. Raspino, J. Boxall, D. Pooley, S. Moorby, E. Schooneveld, N.J. Rhodes, C. Andreani, and F. Fernandez-Alonso (submitted).
[197] Url: http://www.isis.stfc.ac.uk/instruments/iris/ (Last accessed 30 March 2017).
[198] Url: http://www.isis.stfc.ac.uk/instruments/osiris/ (Last accessed 30 March 2017).
[199] M.T.F. Telling, S.I. Campbell, D. Engberg, D. Martín y Marero, and K.H. Andersen, *Phys. Chem. Chem. Phys.* **18** 8243 (2016).
[200] F. Demmel, D. McPhail, J. Crawford, D. Maxwell, K. Pokhilchuk, V. Garcia Sakai, S. Mukhopadhyay, M.T.F. Telling, F.J. Bermejo, N.T. Skipper, and F. Fernandez-Alonso, *EPJ Web Conf.* **83** 03003 (2015).
[201] Url: http://www.isis.stfc.ac.uk/instruments/tosca/ (Last accessed 30 March 2017).
[202] R.S. Pinna, S. Rudić, S.F. Parker, G. Gorini, and F. Fernandez-Alonso, *EPJ Web Conf.* **83** 03013 (2015).
[203] J. Mayers, *Phys. Rev. Lett.* **71** 1553 (1993).
[204] K. Refson, S.J. Clark, and P.R. Tulip, *Phys. Rev. B* **73** 155114 (2006).
[205] Y. Finkelstein, D. Nemirovski, R. Moreh, and G. Kimmel, *Physica B* **291** 213 (2000).
[206] C.A. Howard, M.P.M. Dean, and F. Withers, *Phys. Rev. B* **84** 241404R (2011).
[207] R.J.-M. Pellenq, F. Marinelli, J.D. Fuhr, F. Fernandez-Alonso, and K. Refson, *J. Chem. Phys.* **129** 224701 (2008).

[208] F. Fernandez-Alonso, C. Cabrillo, R. Fernández-Perea, F.J. Bermejo, M.A. González, C. Mondelli, and E. Farhi, *Phys. Rev. B* **86** 144524 (2012).
[209] G. J. Kubas, *Chem. Rev.* **107** 4152 (2007).
[210] A.G. Seel and R. Senesi (eds), *Proceedings of the VI Workshop in Electron Volt Neutron Spectroscopy*, *J. Phys. Conf. Ser.* **571** (2014). Url: http://iopscience.iop.org/issue/1742-6596/571/1 (Last accessed 30 March 2017).
[211] K.V. Tian, B. Yang, Y. Yue, D.T. Bowron, J. Mayers, R.S. Donnan, C. Dobó-Nagy, J.W. Nicholson, D.-C Fang, A. Lindsay Greer, G.A. Chass, and G.N. Greaves, *Nat. Commun.* **6** 8631 (2015).
[212] M.R. Ryder, B. Civalleri, T.D. Bennett, S. Henke, S. Rudić, G. Cinque, F. Fernandez-Alonso, and J.-C. Tan, *Phys. Rev. Lett.* **113** 215502 (2014).
[213] C. Cabrillo, F. Barroso-Bujans, R. Fernández-Perea, F Fernandez-Alonso, D.T. Bowron, and F.J. Bermejo, *Carbon* **100** 546 (2016).
[214] F. Barroso-Bujans, S. Cerveny, P. Palomino, E. Enciso, S. Rudić, F. Fernandez-Alonso, A. Alegría, and J. Colmenero, *Macromolecules* **49** 5704 (2016).
[215] F. Barroso-Bujans, P. Palomino, F. Fernandez-Alonso, S. Rudić, A. Alegría, J. Colmenero, and E. Enciso, *Macromolecules* **47** 8729 (2014).
[216] F. Barroso-Bujans, F. Fernandez-Alonso, and J. Colmenero, *J. Phys. Conf. Ser.* **549** 012009 (2014).
[217] F. Barroso-Bujans, P. Palomino, S. Cerveny, F. Fernandez-Alonso, S. Rudić, A. Alegría, J. Colmenero, and E. Enciso, *Soft Matter* **9** 10960 (2013).
[218] F. Barroso-Bujans, F. Fernandez-Alonso, J.A. Pomposo, S. Cerveny, A. Alegría, and J. Colmenero, *ACS Macro Lett.* **1** 550 (2012).
[219] F. Barroso-Bujans, F. Fernandez-Alonso, J.A. Pomposo, E. Enciso, J.L.G. Fierro, and J. Colmenero, *Carbon* **50** 5232 (2012).
[220] F. Barroso-Bujans, F. Fernandez-Alonso, S. Cerveny, S. Arrese-Igor, A. Alegría, and J. Colmenero, *Macromolecules* **45** 3137 (2012).
[221] F. Barroso-Bujans, F. Fernandez-Alonso, S. Cerveny, S.F. Parker, A. Alegría, and J. Colmenero, *Soft Matter* **7** 7173 (2011).
[222] G. Graziano, *Ph.D. Thesis*, University College London, United Kingdom (2015).
[223] G. Graziano, J. Klimeš, F. Fernandez-Alonso, and A. Michaelides, *J. Phys.: Condens. Matter* **24** 424216 (2012).
[224] C. Lamonier, E. Payen, P.C.H. Mitchell, S.F. Parker, J. Mayers, and J. Tomkinson, *Stud. Surf. Sci. Catal.* **130** 3161 (2000).
[225] P.C.H. Mitchell, D.A. Green, E. Payen, and A.C. Evans, *J. Chem. Soc. Faraday Trans.* **91** 4467 (1995).
[226] I.P. Silverwood, S.F. Parker, and C.R.A. Catlow, *Phys. Chem. Chem. Phys.* **18** 17140 (2016). This reference corresponds to the editorial for a themed *Phys. Chem. Chem. Phys.* issue entitled *Neutron Scattering in Catalysis and Energy Materials.*
[227] N. Notman, *Chemistry World* **13** 49 (2016).
[228] G.S. Timmins, *Expert Opin. Ther. Pat.* **24** 1067 (2014).
[229] T. Egami and S.J.L. Billinge, *Underneath the Bragg Peaks – Structural Analysis of Complex Materials* (Pergamon, London, 2012).
[230] P. Dai, *Rev. Mod. Phys.* **87** 855 (2015).
[231] E. Cannuccia and A. Marini, *Phys. Rev. Lett.* **107** 255501 (2011).
[232] T.E. Weller, M. Ellerby, S.S. Saxena, R.P. Smith, and N.T. Skipper, *Nature Phys.* **1** 39 (2005).
[233] A.P. Drozdov, M.I. Eremets, I.A. Troyan, V. Ksenofontov, and S.I. Shylin, *Nature* **525** 73 (2015).
[234] J.M. Skelton, L.A. Burton, S.C. Parker, A. Walsh, C.-E. Kim, A. Soon, J. Buckeridge, A.A. Sokol, C.R.A. Catlow, A. Togo, and I. Tanaka, *Phys. Rev. Lett.* **117** 075502 (2016).
[235] Y. Shen and E.J. Reed, *J. Phys. Chem. C* **120** 17759 (2016).
[236] F. Paesani, *Acc. Chem. Res.* **49** 1844 (2016).

[237] J. Dawidowski, L.A. Rodríguez-Palomino, J.I. Márquez Damián, J.J. Blostein, and G.J. Cuello, *Ann. Nucl. Energy* **571** 012006 (2014).
[238] L.A. Rodríguez-Palomino, J. Dawidowski, J.J. Blostein, and G.J. Cuello, *J. Phys. Conf. Ser.* **90** 247 (2016).
[239] R.M. Lindstrom, *J. Res. Natl. Inst. Stand. Technol.* **98** 127 (1993).
[240] G. Festa, L. Arcidiacono, A. Pappalardo, T. Minniti, C. Cazzaniga, A. Scherillo, C. Andreani, and R. Senesi, *J. Instrum.* **11** C03060 (2016).
[241] F. Murtas, G. Croci, A. Pietropaolo, G. Claps, C.D. Frost, E. Perelli Cippo, D. Raspino, M. Rebai, N.J. Rhodes, E.M. Schooneveld, M. Tardocchi, and G. Gorini, *J. Instrum.* **7** P07021 (2012).
[242] M.A. Adams, S.F. Parker, F. Fernandez-Alonso, D.F. Cutler, C. Hodges, and A. King. *Appl. Spectrosc.* **63** 727 (2009).
[243] Url: http://www.j-parc.jp/MatLife/en/index.html (Last accessed 30 March 2017).
[244] Url: http://www.isis.stfc.ac.uk/instruments/Chipir/ (Last accessed 30 March 2017).